



## Actuator Line Modeling of Wind Turbine Wakes

Troldborg, Niels

*Publication date:*  
2009

*Document Version*  
Early version, also known as pre-print

[Link back to DTU Orbit](#)

*Citation (APA):*  
Troldborg, N. (2009). *Actuator Line Modeling of Wind Turbine Wakes*.

---

### General rights

Copyright and moral rights for the publications made accessible in the public portal are retained by the authors and/or other copyright owners and it is a condition of accessing publications that users recognise and abide by the legal requirements associated with these rights.

- Users may download and print one copy of any publication from the public portal for the purpose of private study or research.
- You may not further distribute the material or use it for any profit-making activity or commercial gain
- You may freely distribute the URL identifying the publication in the public portal

If you believe that this document breaches copyright please contact us providing details, and we will remove access to the work immediately and investigate your claim.

# **Actuator Line Modeling of Wind Turbine Wakes**

by

**Niels Trolldborg**

Dissertation submitted to the Technical University of Denmark in partial fulfillment of the requirements for the degree of Doctor of Philosophy in Mechanical Engineering

**Fluid Mechanics  
Department of Mechanical Engineering  
Technical University of Denmark  
June, 2008**

Fluid Mechanics  
Department of Mechanical Engineering  
Nils Koppels Allé, Building 403  
Technical University of Denmark  
DK-2800 Lyngby, Denmark

Copyright © Niels Trolborg, 2008

Printed in Denmark by DTU-Tryk, Lyngby

ISBN 978-87-89502-80-9

# Preface

This thesis is submitted in partial fulfillment of the requirements for the Ph.D. degree from the Technical University of Denmark (DTU). The research work was conducted during the period from February 2005 to June 2008 at the Department of Mechanical Engineering (MEK), Fluid Mechanics Section.

I wish to express my sincere gratitude to my supervisors Professor Jens N. Sørensen and Associate Professor Robert Mikkelsen for all their support and helpful guidance during my studies.

I would also like to thank senior researchers Gunner Larsen and Helge A. Madsen from Risø National Laboratory for many useful inputs on wake turbulence analysis.

Finally, I would like to thank my family and friends for their support and to Solveig for her love, patience and support.

Technical University of Denmark  
Lyngby, June 2008.

Niels Trolldborg



# Contents

<b>Preface</b>	<b>i</b>
<b>Contents</b>	<b>ii</b>
<b>List of Symbols</b>	<b>v</b>
<b>Abstract</b>	<b>1</b>
<b>Dansk resumé</b>	<b>2</b>
<b>1 Introduction</b>	<b>3</b>
1.1 Prior works . . . . .	3
1.1.1 Near wake studies . . . . .	4
1.1.2 Far wake studies . . . . .	5
1.1.3 Actuator disc models . . . . .	8
1.1.4 Summary and status . . . . .	10
1.2 Present work . . . . .	11
<b>2 Numerical Modeling</b>	<b>13</b>
2.1 Actuator line model . . . . .	13
2.2 Flow solver - EllipSys3D . . . . .	15
2.3 Modeling the atmospheric boundary layer . . . . .	16
2.3.1 Modeling the mean wind shear . . . . .	16
2.3.2 Modeling the atmospheric turbulence . . . . .	19
2.4 Computational domains . . . . .	21
2.5 Wind turbines . . . . .	22
2.6 Summary . . . . .	23
<b>3 Numerical sensitivity</b>	<b>24</b>
3.1 Domain dimensions . . . . .	24
3.2 Regularization parameter . . . . .	25
3.3 Time step . . . . .	26
3.4 Pressure solver . . . . .	26
3.5 Reynolds number . . . . .	27
3.6 Differencing scheme . . . . .	28
3.7 Grid configuration and resolution . . . . .	29
3.8 Boundary conditions . . . . .	31

3.9	Summary . . . . .	32
<b>4</b>	<b>Wind Turbine Wake Aerodynamics in Uniform Inflow - Initial Results</b>	<b>33</b>
4.1	Numerical Setup . . . . .	33
4.2	Validation - comparison with measurements . . . . .	33
4.3	Blade loading . . . . .	34
4.4	Wake flow characteristics . . . . .	35
4.5	Summary . . . . .	39
<b>5</b>	<b>Wind Turbine Wake Aerodynamics in Uniform Inflow - Vortex Properties</b>	<b>41</b>
5.1	Classical wake models . . . . .	41
5.2	Vortex positions and pitch . . . . .	43
5.3	Circulation . . . . .	46
5.4	Induced velocities . . . . .	47
5.5	Summary . . . . .	50
<b>6</b>	<b>Wind Turbine Wake Aerodynamics in Uniform Inflow - Turbulence Properties</b>	<b>52</b>
6.1	Reynolds stresses . . . . .	52
6.2	Self-similarity . . . . .	55
6.3	Spectral characteristics . . . . .	56
6.4	Characteristic length scales . . . . .	57
6.5	Coherence . . . . .	58
6.6	Large scale dynamics . . . . .	59
6.7	Summary . . . . .	60
<b>7</b>	<b>Wind Turbine Wake Aerodynamics in Atmospheric Shear Flow</b>	<b>61</b>
7.1	Mesh configuration . . . . .	61
7.2	Atmospheric shear layer modeling . . . . .	61
7.3	Blade loading . . . . .	62
7.4	Wake characteristics . . . . .	64
7.5	Summary . . . . .	70
<b>8</b>	<b>Wind Turbine Wake Aerodynamics in Turbulent Inflow - Initial Results</b>	<b>71</b>
8.1	Numerical setup . . . . .	71
8.2	Inflow turbulence decay . . . . .	72
8.3	Wake characteristics . . . . .	74
8.4	Summary . . . . .	76
<b>9</b>	<b>Wind Turbine Wake Aerodynamics in Turbulent Non-Sheared Inflow - Turbulence Characteristics</b>	<b>77</b>
9.1	Inflow turbulence characteristics . . . . .	77
9.2	Validation - comparison with measurements . . . . .	78
9.3	Reynolds stresses . . . . .	79
9.4	Self-similarity . . . . .	80
9.5	Spectral characteristics . . . . .	80
9.6	Characteristic length scales . . . . .	81
9.7	Coherence . . . . .	82

9.8	Large scale dynamics . . . . .	83
9.9	Summary . . . . .	89
<b>10</b>	<b>Wind Turbine Wake Aerodynamics in Atmospheric Sheared and Turbulent Inflow</b>	<b>90</b>
10.1	Overall wake characteristics . . . . .	90
10.2	Self-similarity . . . . .	92
10.3	Characteristic length scales . . . . .	93
10.4	Coherence . . . . .	95
10.5	Large scale dynamics . . . . .	96
10.6	Summary . . . . .	98
<b>11</b>	<b>Wake Interaction between a Row of 3 Turbines</b>	<b>99</b>
11.1	Mesh configuration . . . . .	99
11.2	Qualitative wake characteristics . . . . .	99
11.3	Mean Wake Characteristics . . . . .	100
11.4	Rotor loading . . . . .	103
11.5	Summary . . . . .	104
<b>12</b>	<b>Wake Interaction between 2 Turbines in Strongly Sheared and Low Turbulent Atmospheric Flow</b>	<b>106</b>
12.1	Mesh configuration and numerical setup . . . . .	106
12.2	Atmospheric boundary layer modeling . . . . .	107
12.3	Blade loading . . . . .	107
12.4	Wake Characteristics . . . . .	109
12.5	Summary . . . . .	112
<b>13</b>	<b>Conclusion</b>	<b>113</b>
<b>A</b>	<b>Basic concepts of turbulence applied to wind turbine wakes</b>	<b>116</b>
A.1	Turbulence statistics . . . . .	116
A.2	Correlation and scales of turbulence . . . . .	116
A.3	Coherence . . . . .	120
A.4	Proper orthogonal decomposition (POD) . . . . .	124
A.5	Self-similarity . . . . .	126
A.6	Summary . . . . .	127
	<b>Bibliography</b>	<b>128</b>

# List of Symbols

## Roman letters

$a$	Radial position of tip vortices	$[m]$	$p$	Pressure	$\left[\frac{N}{m^2}\right]$
$a_i$	Coefficient of POD mode $i$	$\left[\frac{m}{s}\right]$	$r_{1/2}$	Wake half width	$[m]$
$a_z$	Axial interference factor	$[-]$	$R$	Rotor radius	$[m]$
$c$	Chord length	$[m]$	$S_i, S_{i,i}$	Power spectrum of $v_i$	$\left[\frac{m^2}{s}\right]$
$C$	Coherence decrement	$[-]$	$S_{k,i}$	Kaimal power spectrum of $v_i$	$\left[\frac{m^2}{s}\right]$
$C_D$	Drag coefficient	$[-]$	$S_{i,j}$	Cross spectrum between $v_i$ and $v_j$	$\left[\frac{m^2}{s}\right]$
$C_L$	Lift coefficient	$[-]$	$r, \theta, z$	Polar coordinates	$[m, rad, m]$
$C_P$	Power coefficient	$[-]$	$s, t, n$	Spanwise, tangential, normal coordinates relative to blade	$[m, rad, m]$
$C_T$	Thrust coefficient	$[-]$	$t$	Time	$[s]$
$coh$	Spectral coherence	$[-]$	$U_i, V_i$	Velocity component $i$	$\left[\frac{m}{s}\right]$
$d$	Distance	$[m]$	$V_\infty$	Free-stream velocity / Velocity at hub height	$\left[\frac{m}{s}\right]$
$D$	Drag force	$\left[\frac{N}{m}\right]$	$V_0$	Mean inlet velocity	$\left[\frac{m}{s}\right]$
$e$	Unit vector	$[-]$	$V_\infty$	Characteristic velocity difference	$\left[\frac{m}{s}\right]$
$f$	Frequency	$[s^{-1}]$	$V_{rel}$	Relative velocity at blade section	$\left[\frac{m}{s}\right]$
$f$	Body force	$\left[\frac{m}{s^2}\right]$	$u_i, v_i$	Fluctuating velocity component $i$	$\left[\frac{m}{s}\right]$
$f_r$	Reduced frequency	$[-]$	$u_*$	Friction velocity	$\left[\frac{m}{s}\right]$
$f_v$	Self-similar velocity	$[-]$	$x, y, z$	Cartesian coordinates	$[m]$
$f_{2D}$	Loading	$\left[\frac{N}{m}\right]$	$y_0$	Roughness height	$[m]$
$h$	Helical pitch	$[m]$	$z_d$	Distance to inflow turbulence plane	$[m]$
$H$	Tower height	$[m]$			
$l$	$h/2\pi$	$[m]$			
$L$	Lift force	$\left[\frac{N}{m}\right]$			
$L_{i,j}^{(k)}$	Integral length scale	$[m]$			
$L_{k,i}$	Kaimal length scale of $v_i$	$[m]$			
$L_x$	Domain width	$[m]$			
$L_y$	Domain height	$[m]$			
$L_z$	Domain length	$[m]$			
$\hat{M}_y$	Equivalent yaw moment	$[Nm]$			

## Greek letters

$\alpha$	Angle of attack	$[^{\circ}]$	$\rho_{i,j}$	Correlation coefficient between $v_i$ and $v_j$	$[-]$
$\alpha$	Wind shear exponent	$[-]$	$\sigma_i$	Standard deviation of $v_i$	$\left[\frac{m}{s}\right]$
$\gamma$	Pitch angle	$[^{\circ}]$	$\sigma_{k,i}$	Standard deviation of $v_i$ estimated from Kaimal spectrum	$\left[\frac{m}{s}\right]$
$\Gamma$	Circulation	$\left[\frac{m^2}{s}\right]$	$\tau$	Integral time scale	$[s]$
$\epsilon$	Regularization parameter	$[-]$	$\phi^k$	POD mode $k$	$[-]$
$\eta$	Regularization function	$[-]$	$\phi_m$	Angle used in parameterization of coherence	$[^{\circ}]$
$\eta$	$y/H$	$[-]$	$\varphi$	Flow angle	$[^{\circ}]$
$\theta$	Azimuthal angle	$[^{\circ}]$	$\varphi_y$	Yaw angle	$[^{\circ}]$
$\lambda$	Tip-speed ratio: $\frac{\Omega R}{V_{\infty}}$	$[-]$	$\psi$	Wake age	$[^{\circ}]$
$\mu$	Dynamic viscosity	$\left[\frac{kg}{m \cdot s}\right]$	$\Omega$	Angular rotor velocity	$\left[\frac{rad}{s}\right]$
$\nu$	Kinematic viscosity	$\left[\frac{m^2}{s}\right]$			
$\xi$	$r/r_{1/2}$	$[-]$			
$\rho$	Mass density	$\left[\frac{kg}{m^3}\right]$			

## Indices

$\infty$	Free stream	$r\theta z$	Polar components
0	Inlet / prescribed	$rel$	Relative
$d,w$	Disc / far wake	$rot$	Rotational
$k$	Kaimal	$stn$	Spanwise, tangential, normal components
$(in), (w)$	inlet / wake	$xyz$	Cartesian components
$ijkln$	Indices		

## Special numbers

CFL	Courant - Friedrichs - Lewy number, $\frac{V_{\theta} \Delta t}{\Delta z}$	$[-]$	Re	Reynolds number, Rotor: $\frac{V_{\infty} R}{\nu}$ , Aerofoil: $\frac{V_{\infty} c}{\nu}$	$[-]$
Pe	Peclet number, $\rho V \frac{\Delta z}{\mu}$	$[-]$			

## Acronyms

2D,3D	Two or Three-Dimensional	CFD	Computational Fluid Dynamics
AD	Actuator Disc	LDA	Laser Doppler Anemometry
AL	Actuator Line	LES	Large Eddy Simulation
DWM	Dynamic Wake Model	PIV	Particle Image Velocimetry
BEM	Blade Element Momentum method	RANS	Reynolds Averaged Navier-Stokes
CDS4	Fourth order central difference		

# Abstract

This thesis contains a comprehensive 3D Navier-Stokes computational study of the characteristics of wakes of wind turbines operating in various flow conditions including interacting wakes between a row of turbines. The computations were carried out using the actuator line technique combined with the 3D Navier Stokes solver EllipSys3D and a LES turbulence model. Simple models, based on applying body forces in the computational domain, are developed for imposing sheared and turbulent inflow and their validity is discussed. A few computations on stand alone turbines are compared to measurements and good to fair agreement are shown in terms of respectively power coefficient and mean wake properties. The turbulence properties in the wake are generally characterized by its spectral characteristics and include estimation of spectral coherence, length scales and Reynolds stresses.

Simulations of the wake from an isolated turbine operating in uniform inflow at tip-speed ratios ranging from  $\lambda = 3.21$  to  $\lambda = 11.78$  is presented and provides detailed information about the wake development including vortex properties and turbulence characteristics.

Calculations on the wake of turbines subject to sheared inflow shows that besides an expected vertical skewed wake the wake also becomes increasingly asymmetric in the horizontal direction as it is convected downstream. The latter phenomena, which is also often observed in measurements, is argued to be caused by the rotation of the wake.

A detailed study is presented to investigate the influence of including turbulence in the inflow. The study shows that the ambient turbulence causes the vortex system in the wake to become unstable much closer to the rotor and as a consequence the wake becomes fully turbulent earlier than if inflow turbulence is neglected. Furthermore, it is shown that the main effect governing the large scale meandering of wakes is the large scale structures of the ambient turbulence field. Finally studies are conducted on rows of respectively two and three turbines. The investigation includes evaluation of the loading on the rotors and it is shown that the turbines are subject to rather severe yaw moments, even in situations where the mean wind is oriented along the row. This observation is indicative of large scale dynamics of the wakes.

# Dansk resumé

Den foreliggende afhandling inkluderer omfattende 3D Navier-Stokes beregninger af kølvandet fra vindmøller opererende under forskellige betingelser inklusiv interagerende kølvand mellem møller placeret i rækker. Simuleringerne er udført ved hjælp af actuatorliniemodellen kombineret med 3D Navier-Stokes løseren EllipSys3D og en LES turbulensmodel. Simple modeller, baseret på anvendelse af volumenkræfter, til at påtrykke vindgradient og turbulens er udviklet og deres anvendelse valideres. Nogle få beregninger på enkeltstående møller er sammenlignet med målinger og god overenstemmelse er opnået både for effekt kurven samt middelhastigheder og turbulensintensitet i kølvandet. Turbulensegenskaberne i kølvandet er karakteriseret ved deres spektrale egenskaber og inkluderer estimering af spektral kohærens, længdeskalaer og Reynoldsspændinger.

Simuleringer af kølvandet fra en isoleret mølle opererende i et ensartet indløb ved tip hastighedsforhold mellem  $\lambda = 3.21$  to  $\lambda = 11.78$  præsenteres og giver detaljerede informationer om kølvandets udvikling inklusiv hvirvel og turbulensegenskaberne.

Beregninger på kølvandet fra møller i en vertikal vindgradient viser at der, udover en forventet lodret skævhed af kølvandet, også opstår en vandret asymmetri der vokser i størrelse nedstrøms møllen. Det sidstnævnte fænomen er ligeledes observeret i flere målinger og det argumenteres at asymmetrien skyldes rotationen af kølvandet.

Et detaljeret studie af indflydelsen af at inkludere turbulens i indløbet viser at den omgivende turbulens forårsager at hvirvelsystemet i kølvandet bliver ustabil meget tættere på rotoren og som følge heraf bliver kølvandet fuldt turbulent tidligere end hvis indløbet er laminart. Endvidere vises det at storskaladynamikken af kølvandet hovedsagligt er bestemt af de store kohærente strukturer i den omgivende turbulens.

Afslutningsvis præsenteres numeriske simuleringer af rækker på henholdsvis to og tre møller. Studierne inkluderer evaluering af lastpåvirkningerne på roterene og det observeres at krøjemomentlasterne kan være signifikante selv i tilfælde hvor middelvindhastigheden er i samme retning som møllernes fællesakse. Dette er en indikation på storskalabevægelse af kølvandene.

# Chapter 1

## Introduction

Wind turbines clustered in wind farms are generally subject to a mixed type flow field which in part is undisturbed and in part influenced by the wake from upstream turbines. As a consequence, these turbines experience a flow field which is substantially altered compared to an isolated turbine, which in effect reduce power production and increase fatigue loads. The usual modeling approach used by industry for compensating for wake interaction is by increasing the overall turbulence level and decreasing the inflow velocity in the design process, however, with the disadvantages of not capturing the actual turbulence characteristics properly. Nor does such a modeling approach satisfactorily take into account the important mechanism of wake deficit meandering, which has been observed in field measurements and may contribute significantly to the increased loads of downstream turbines. These deficiencies in the modeling of wind turbine wakes have created a widespread desire in the wind industry to get more reliable predictions of the flow field experienced by wind turbines operating in the wake of other turbines.

### 1.1 Prior works

Although wakes, as revealed from several comprehensive reviews [86], [14], [70], have been a topic of intensive research during the last decades the basis of wind turbine aerodynamics is still not fully understood even under simple operational conditions.

In the study of wind turbine wakes a distinct division is typically made between the near wake and the far wake. Nevertheless, the definition of the two regions is somewhat ambiguous. Usually, the near wake is considered to be the region where the presence of the rotor is felt directly by the number of blades and the blade aerodynamics. Using this definition the near wake is essentially the region in which the helical vortex system formed behind the rotor remains stable and distinct since the shed vortices are directly associated with the radial variation of the bound vorticity on the blades. Therefore, depending on the rotor loading and the inflow conditions, the near wake region may extent several diameters downstream of the turbine. Furthermore, this definition, confusingly imply that the near wake includes the region considered to be the far wake in the Blade Element Momentum (BEM) method [26], [65] as well as in some analytical vortex methods [60], [61].

The far wake is the region beyond the downstream position where the wake dynamics are more or less independent on rotor characteristics. In this region the vortex system formed by the rotor is completely broken down and the flow field is governed by small scale turbulence.



In the following a survey of previous works on wind turbine wakes will be presented. In the first two subsections, the works on respectively the near and far wakes are reviewed. Note that the studies, which consider the influence of shear, ambient turbulence and other external effects, are described in the section about far wakes. The third subsection is dedicated to reviewing the research work conducted using the actuator disc principle.

### 1.1.1 Near wake studies

A vast number of researches have been conducted on the near wake characteristics of wind turbines.

Ebert and Wood [16], [17], [18] conducted a series of measurements in the near wake of a small 2 bladed horizontal axis wind turbine model at different tip speed ratios. They found that at high tip speed ratios, the tip vortices contain a large part of the angular momentum in the wake and since this angular momentum balance the power output of the turbine they concluded that the properties of the tip vortices should be incorporated in new rotor models. Furthermore, they showed that the pitch of the tip vortices remained rather constant within the first 0.4 rotor radii downstream the turbine.

Medici et al. [52] carried out comprehensive wind tunnel measurements in the wake of different model rotors using both hotwire anemometry and PIV. Fundamental characteristics of the wake and tip vortices were shown both in axial and yawed flow. In the experiments the tip vortices could be detected up to approximately 3 diameters downstream the rotor. Moreover, they showed interesting results connected to yaw-control and large scale vortex shedding in the wake.

Whale et al. [88] conducted PIV measurements in the wake of a three bladed model wind turbine in a water tank and compared them with data obtained in the wake of two full scale turbines located at two different sites. The comparison showed fair to rather poor agreement and the discrepancies were attributed to various factors such as Reynolds number scale effects, water tank blockage, complex terrain and other uncertainties in the full-scale measurements.

Later Whale and co-workers [89] made a PIV investigation of the properties of the wake of a two bladed model rotor operating at different tip speed ratios and compared the results with numerical simulations using an inviscid free vortex wake method. The study revealed good qualitative agreement between the wake structure obtained from experiments and computations in terms of wake shape, including expansion. Furthermore, it was shown that as long as similarity is obtained in tip speed ratio, the behavior of the wake might be only vaguely sensitive to blade Reynolds number.

The near wake has moreover been studied by means of vortex wake models with the wake geometry being either free [6] or prescribed [11]. Even though free wake models can be straightforwardly applied to general unsteady flow situations they are computationally costly and tend to suffer from stability problems due to the intrinsic singularities of the vortex panels. On the other hand, owing to their dependence on various parameters, prescribed wake models tend to be limited to more or less well-known steady flow problems.

Also analytical vortex wake models have been proposed in which the wake structure and behavior of the tip vortices is studied by considering the problem of determining the induced velocity field and stability of a system of helical vortices.

Okulov [60] considered a vortex system consisting of an arbitrary number of identical slender helical vortices with constant circulation and pitch. The study showed that for vorticity fields

with helical symmetry simple expressions exist, relating the axial velocity to the tangential velocity and the axial vorticity to the tangential vorticity.

More recently, Okulov and Sørensen [61] extended this work to more general applications by embedding the system of helical vortices in different types of assigned flow fields. Thereby, they developed a model suitable for analyzing wakes consisting of helical tip vortices as well as the trailing vortex sheet of the blades and the root vortex. By means of a parametrical study they presented stability properties of the tip vortices for assigned flows consisting of axisymmetric helical vortices with different distributions of axial vorticity. In contrast to previous analytical works they showed that the tip vortices may be stable and that the radial extents of the assigned vorticity field strongly influence the stability properties. Results of their proposed model were compared to the measurements obtained by Medici [52] and generally good agreement was shown.

Full three-dimensional computations employing the Reynolds-averaged Navier-Stokes equations have been carried out by e.g. Sørensen et al. [78]. Although advanced CFD methods have proven to be suitable for predicting and understanding the flow around wind turbines they still have some shortcomings in terms of inaccurate turbulence and transition modeling. Furthermore, these methods normally are too computationally demanding to obtain a fine grid resolution in the wake.

Recently, however Zahle [91] presented full three-dimensional unsteady Navier Stokes computations on the NREL wind turbine using the so-called overset grid method to facilitate a high resolution of both rotor and wake with a reasonable number of grid points. Good agreement with measurements was obtained including the blade tower vortex interaction.

The same technique was later used by Zahle and Sørensen [92] to study the influence of grid resolution on the integrated forces acting on the NREL Phase VI rotor. Their computations showed that a high resolution of the region located beyond one rotor radius downstream of the rotor only marginally affected the velocities in the rotor plane.

### 1.1.2 Far wake studies

The far wake has also been a subject of extensive research both experimentally and numerically. A common difficulty in field measurements of the far wake is that the dynamically changing inflow generally is not fully known and even in situations where turbulence is low data acquisition is limited to rather few measuring stations. Therefore, it can be difficult to identify and isolate the effect of a specific process; though with the emergence of the LiDAR technique some of these problems can be greatly reduced. On the other hand research work conducted in wind tunnels under controlled conditions often suffer from various scale and blocking effects whereby the findings of such studies might not relate to full scale wind turbines.

The NREL Unsteady Aerodynamics Experiment [21], [68] and the more recent European MEXICO project [71] are, so far, some of the very few wind tunnel experiments carried out on wind turbines which are representative to full scale turbines. However, in the former project only few wake measurements were included and in the MEXICO project the detailed PIV measurements of the wake were only carried out in the region extending from approximately 1 diameter upstream to little over 1 diameter downstream of the rotor.

Semi-analytical far wake models have been proposed to describe the wake velocity after the initial expansion [2], [23], [24]. Typically a near wake region is defined during which the pressure recovers to the atmospheric level and the wake becomes fully developed. In this domain

one dimensional momentum theory is normally used as a starting point for establishing the wake deficit. After the near wake region the models usually assume rotational symmetry and self-similarity of the wake deficit based on a Gaussian form or on profiles obtained from investigations on jets. A problem of most of these models is that they tend to depend on a number of coefficients and parameters, such as the near wake length and expansion rate, which needs to be empirically determined, hence questioning their validity in more general applications.

Furthermore, as these models mainly aim at capturing mean flow characteristics, they usually do not correctly include the important dynamic wake meandering. It is greatly acknowledged that wake meandering may considerably increase extreme loads and in particular yaw loads on turbines located in wind farms [46]. The reason for this is that the meandering causes the wake from upstream turbines to be swept in and out of the rotor plane of downstream turbines. As a consequence a downstream turbine continuously experience part wake situations even in cases where the mean wind is in line with the turbines. Moreover, the meandering significantly contributes to the reduction of the depth of the mean wake deficit and hence models disregarding the effect of meandering tend to under predict the power output of downstream turbines [22].

Ainslie [3] developed a model which included the effect of meandering on wake deficits by correlating the large scale motion of the wake to the variability in the wind direction. Later, he [4] compared model results to different full scale experiments and generally obtained good agreement between measured and predicted centerline velocity deficit as a function of downstream distance.

In their wind tunnel study of the wake flow characteristics behind a small wind turbine model, Medici et al. [52] observed a clear indication of large scale vortex shedding similar to the well known von Karman vortex street experienced behind two-dimensional cylinders and they hypothesized that these findings might be connected with wake meandering.

Recently, Larsen and colleagues [43], [44] presented a consistent physical theory for describing the dynamic wake meandering. The basic conjecture behind the so called Dynamic Wake Model (DWM) is that wake meandering is governed by the large scale lateral and vertical turbulence components in the atmosphere - an interpretation which has been supported by Bingöl et al. [9] who conducted LiDAR measurements of the wake from a full scale wind turbine located in the field. For completing the theory of the DWM model, the formulation of the large scale wake dynamics was further combined with models for respectively the mean velocity deficit and the added wake turbulence in the meandering frame of reference. Larsen et al. [43] presented the first steps toward developing a suitable model for the added wake turbulence in the meandering frame of reference. In this context they proposed to use the enhanced spectral method of Nielsen et al. [59], which allows for simulating the inhomogeneous, non-stationary and non-Gaussian turbulence that normally characterize a wind turbine wake. However, such approach requires detailed knowledge about the turbulence properties of the wake in terms of spectral characteristics, length scales and spectral coherence.

These quantities have been studied previously through field measurements [32], [85], [80] wind tunnel experiments [81] and simulations [13]. The uncertainty related to determination of the scales of turbulence from measurements is, as discussed by Frandsen [24], and also mentioned above, generally large due to scale effects, limited data acquisition and/or insufficient knowledge about the ever changing inflow, which is also reflected in the rather large variability of the reported wake length scales.

Therefore, it is beneficial to use numerical methods since these besides providing all needed data about the wake also makes it easier to study the effect of a single parameter.

Detailed numerical studies of the far wake, including the development of the Reynolds stresses, have been carried out by Crespo and colleagues [12], [13], [27] using methods based on the UPMWAKE model in which the wind turbine is supposed to be immersed in an atmospheric boundary layer. This model uses a finite difference approach to solve the parabolized RANS equations combined with a  $k - \epsilon$  turbulence model. The code is capable of predicting some fundamental effects in the far wake and generally has proved to compare reasonably well with measurements but as the model is based on parabolized Navier-Stokes equations it cannot be applied to situations where flow recirculation occurs.

As mentioned above wind shear and atmospheric turbulence is inherent for all wake measurements carried out in the field. Nevertheless, computations on wind turbines operating in non-uniform conditions are rare compared to the amount conducted in uniform inflow. Most of the numerical studies conducted on wind turbine wakes in shear flows uses simplified representations of the rotors such as the actuator disc or line technique (see section 1.1.3).

Sørensen and Johansen [79] simulated the rotor designed in connection with the UPWIND project subject to a strongly sheared inflow. For the simulation they used a spherical computational grid, which rotated with the rotor and thus no physical wall boundary was included. The velocity shear was imposed at the inlet boundary in a way that ensured a constant low velocity at ground level. The computations revealed considerable circumferential hysteresis effects of the blade loading and showed disturbances of the velocity field upstream of the rotor, which were much larger than for the same rotor operating in uniform inflow.

More recently, Zahle and Sørensen [93] used full Navier Stokes computations combined with an overset grid technique to simulate the flow over two different rotors operating in a strongly sheared inflow. Thereby, they facilitated a more correct inclusion of the wall boundary and the numerical predictions were compared to those obtained using a spherical grid similar to the one presented by Sørensen and Johansen [79]. Although, the study revealed reasonable good agreement in the predictions of the blade forces the induced velocities upstream of the rotor, were observed to differ significantly. When using the overset grid technique the upstream influence was reduced to levels comparable to that seen for a uniform inflow case, as should be expected, and therefore it was concluded that this method were more suitable for simulating turbines in shear flow.

Besides, presenting the loading on the rotors the downstream development of the wake was also investigated qualitatively. Contours of the instantaneous velocity and vorticity in a vertical plane along the center axis revealed a skewed wake due to the higher transport velocity at the top. Moreover, contour plots of the axial velocity at various downstream cross-sections revealed a development where the wake became increasingly horizontally asymmetric with downstream position.

The horizontal asymmetry was not observed to the same extent immediately downstream of the rotor and also was not seen in the blade loads, which were found only to lag the blade azimuth position moderately. Evidently, it seems that, rather than the load distribution, it is the rotation of the wake which is responsible for the asymmetry as it causes low velocity air from the lower part of the wake to surge upwards on one side and high velocity air from the upper part to move downwards on the other side. This is an interesting observation since it might be expected that when the load distribution on the blade is nearly the same at the two horizontal positions then this should also be reflected in a nearly horizontally symmetric development of the wake.

In fact, studies of wakes of turbines operating in shear flows are usually limited to studying the development in the vertical plane intersecting the center axis, which represents the most ob-

vious difference from the purely rotationally symmetric wake, while the full description of the flow field have received less attention. However, there are several field measurements [90], [10], which seems to indicate that the wake is asymmetric in the horizontal direction. Sometimes, the asymmetry is explained as being due to upstream obstacles or other external effects [27]. Nevertheless, the computation of Zahle and Sørensen [93], suggest that the asymmetry may also be due to the rotation of the wake. This hypothesis is further supported by the work of Jimenez et al. [38], where a measured horizontal asymmetry of the wake could not be reproduced by a constant loaded rotor - a model which does not include rotation.

### 1.1.3 Actuator disc models

The numerical simulations presented in this work are all conducted using the actuator line method, which is described in more detail in chapter 2. However, there exists a large variety of methods, which utilize the same overall principles and therefore this section is devoted to reviewing the various formulations of these models and their application.

Characteristic for all the methods is that they use equivalent forces to represent the rotor while the surrounding flow field is governed by a full set of Euler or Navier Stokes equations. The advantage of this technique is mainly that the presence of the rotor is modeled without having to resolve the viscous airfoil boundary layer and therefore the grid resolution can be significantly reduced compared to full CFD.

The simplest formulation is the constantly loaded actuator disc, in which the forces representing the rotor are prescribed and distributed on a permeable disc of zero thickness. This approach has been adopted by several researchers to study and validate the assumptions underling the momentum theory [72] as well as for giving information about fundamental features of axisymmetric wakes including unsteady wake states [74].

More recently, Jimenez et al. [38] used a constant loaded actuator disc in combination with large eddy simulations of the flow field to study the properties of the Reynolds stresses and in later work [39] also the spectral coherence in the wake of turbine operating in a modeled atmospheric boundary layer. The presented results were in both cases found to be in fair agreement with experiments and it was concluded that large eddy simulations are useful for obtaining detailed information about wake flow characteristics.

More accurate rotor modeling is achieved by using the generalized actuator disc method, which essentially represents a straight-forward extension of the blade element momentum method (BEM). The main difference is that, whereas the BEM is based on the assumption of the flow taking place in radial independent stream tubes the generalized actuator disc method has no restriction on the kinematics of the flow since it is governed by the unsteady Euler or Navier Stokes equations. Thus, in the generalized actuator disc method the aerodynamic forces acting on the rotor are, as in the BEM, computed from two dimensional airfoil characteristics, corrected for three-dimensional effects, using a blade element approach. In order to model an actual rotor with a finite number of blades, a tip correction is usually applied to the forces and subsequently they are distributed evenly along each annular element.

Numerical simulations of actual wind turbines employing the generalized actuator disc model have been carried out by Sørensen et al. [72] and Mikkelsen [56] in axisymmetric flow condition in order to study unsteady phenomena and for rotors subject to conning by Madsen and Rasmussen [45] and Mikkelsen et al. [55].

Masson [51] used the actuator disc technique and a  $k - \epsilon$  type turbulence model to simulate a

wind turbine operating in uniform inflow and later Masson and colleagues [5], [40] devised a technique for simulating rotors operating in an atmospheric boundary layer with different types of stratification.

Mikkelsen [56], used an actuator disc approach combined with a full 3D projection of velocities and forces on the disc for establishing approximate simulation of a rotor operating in yaw misaligned conditions. The computed results were found to be in reasonable agreement with measurements; however, a major limitation of the method is that it is incapable of producing skewed wake geometries.

A formulation of the actuator disc method, in which the forces acting on the disc are determined from the local flow conditions in a fully three dimensional manner has been used by Ivanell et al. [37] for simulating a small wind farm consisting of  $3 \times 3$  wind turbines. In this study the turbines were operating in a logarithmic sheared velocity profile and simulations were conducted both with and without inclusion of inflow turbulence. Besides giving a qualitative description of the wake behavior it was also shown that the inflow angle of the oncoming flow and the ambient turbulence level had a significant effect on the total power output of the park.

The main limitation of the actuator disc method is that it strictly speaking only is valid for rotationally symmetric flow conditions since the forces at each spanwise section are distributed evenly in the azimuthal direction. This also imply that the presence of the blades is taken as an integrated part in the circumferential direction and hence the method cannot capture the influence of the tip vortices.

To overcome this limitation Sørensen and Shen [75] developed the actuator line model, where the loading, is distributed along lines representing the blades of the turbine in a fully three-dimensional domain.

This technique, combined with the Navier Stokes equations, was used by Mikkelsen [56] and Ivanell [35] for simulating the wakes of a wind turbine operating in steady uniform inflow and by Mikkelsen [56] for a yawed rotor.

Mikkelsen et al. presented actuator line computations on both isolated turbines [57] and rows of wind turbines [58] placed in prescribed inlet velocity profiles using a simple method based on introducing body forces in the entire computational domain.

Ivanell et al. [36] conducted actuator line computations with a high resolution of the wake to study the stability properties of the tip and root vortices formed in the wake of a wind turbine operating in a laminar and uniform inflow.

The final, and most advanced, class of hybrid methods described in this section is the so-called actuator surface model. This model extent the principles of the actuator line method by distributing the forces, obtained at each airfoil section, along the chord line in a manner that represent the chordwise pressure difference distribution over the airfoil. Thereby, the method more closely resembles the local flow field around the local airfoil section, however still without having to resolve the viscous boundary layer.

Shen and Sørensen [69] proposed a version of the actuator surface model in which the local blade forces are distributed along the airfoil chord according to a set of empirical relations expressing the chordwise pressure difference as a function of airfoil shape and angle of attack. The empirical functions were established by fitting curves to the chordwise pressure obtained from 2D airfoil computations using the XFOIL software. The presented model was used to simulate the flow past a Nordtank 500 kW wind turbine and the numerical predictions were compared with actuator line computations. The comparison showed only small differences but generally the actuator surface model more accurately predicted the flow structure near the blades and in

the region of the tip vortices. Furthermore, it was shown that a certain minimum of grid points are needed in the region of the rotor blades in order to capture correctly the flow around the airfoil.

Dobrev et al. [15] used the actuator surface model together with a simplified representation of the chordwise pressure distribution to simulate the NREL phase VI wind turbine. Comparison with measurements showed that the model was capable of reproducing the mechanical power for low and moderate inflow velocities; whereas larger deviations were observed at high velocities where the flow field is detached.

### 1.1.4 Summary and status

From the above given literature survey the following conclusions about the state of the art of wind turbine wake research can be made:

- The experimental work conducted in wind tunnels are generally put at a disadvantage due to too low Reynolds number and other scale effects. On the other hand in field measurements the flow conditions are generally not fully known due to terrain effects, wind shear, turbulence and changes in wind direction, which complicates identifying a specific phenomenon. For this reason it should be appreciated that, unless the datasets from the given sites are very large, validating numerical models through comparison with field measurements of the wake may be questionable because any observed agreement or discrepancy could be somewhat coincidental.
- Even though a large variety of numerical methods have been developed, ranging from inviscid vortex methods to full unsteady Navier-Stokes based techniques, many of which has proven to show an acceptable agreement with a given set of measurements, it seems that no one has attempted to use these methods for providing more complete and general features of unsteady wind turbine wakes including a satisfactory description of its turbulence characteristics.
- Most of the work conducted so far has either considered the near wake or the far wake, whereas the intermediate region, where the vortex system undergoes a transition from organized flow structures to a fully turbulent flow has received less attention. In this context the stability properties of the tip vortices are of paramount importance, especially in relation to wind turbines that are grouped in wind farms, since it is clear that if a wind turbine is located in a wake consisting of stable tip vortices it will be more severely loaded than if the vortices break down by instability. Although, the stability of helical vortices has been studied both analytically [60], [61] as well as through simulations [87] and experiments [19] it appears that the knowledge about this topic is still far from satisfactory, even for simple inflow conditions.
- The basic aerodynamic behavior of wakes of wind turbines subject to sheared and/or turbulent inflow are other issues which are far from well understood. While wind shear and inflow turbulence is an integrated part of all field measurements, it appears that only few research works have been dedicated to explicitly treating their impact on wind turbine wakes. Most of the investigations on the influence of sheared inflow on the wake only

considers mean properties (velocity and turbulence intensity) in a vertical plane placed along the center axis of the turbine. In fact it seems that the recent computational study of Zahle et al. [93] is the first where examples of the complete three dimensional behavior of the wake from a wind turbine operating in sheared inflow is presented.

- The physics behind large scale wake meandering is still not completely understood. Although several research works indicate that the meandering is driven mainly by the large scale turbulence components of the atmosphere, the phenomena is presumably also influenced by the large coherent structures formed as consequence of vortex break down in a manner which is not known. Nevertheless, the model proposed by Larsen and colleagues [43] is promising since it captures what is believed and seems to be the most important physics of wake meandering and in the same time is easily integrated in existing aeroelastic wind turbine models. However, in order to complete this method, suitable models for the wake deficit as well as for the added wake turbulence described in the meandering frame of reference is required.

## 1.2 Present work

This thesis presents full unsteady three-dimensional Navier Stokes simulations of wakes of wind turbines operating in various inflow conditions using a method, which combines large eddy simulations with an actuator line technique.

The objective of the investigation is to examine in detail the properties of wind turbine wakes and to propose consistent ways of characterizing them. Based on the state of the art of wind turbine wake research the thesis mainly aims at providing more insight into the dynamic features of wind turbine wakes such as wake deficit development, vortex breakdown, turbulence properties and wake meandering. The main focus is on the wake of isolated turbines subject to different flow conditions, including wind shear and/or turbulent inflow, but also results from simulations of two and three interacting wakes are discussed in detail.

The remaining parts of this thesis is organized as follows:

Chapter 2 describes the numerical methods used for simulating the wind turbine wakes and is followed by a study of the sensitivity of the simulations to various solver and flow parameters in chapter 3.

Thereafter a study on isolated turbines is presented in which the complexity of the inflow conditions is systematically increased. Chapter 4-6 present the numerical simulations of the wake of a turbine operating in uniform inflow at different tip speed ratios. The first of these chapters describe the numerical setup and shows the initial results, while the two subsequent chapters present respectively the vortex properties and the turbulence characteristics of the wake.

Chapter 7 consists of a comprehensive study of the blade loading and the wake development from a wind turbine operating in a sheared non-turbulent inflow.

In chapter 8-9, an investigation of the wake from a turbine subject to a non-sheared turbulent inflow is carried out. Initially, the overall wake properties are compared to those observed in uniform inflow. Thereafter, a detailed study of the wake turbulence characteristics is conducted and the results are compared to those obtained from a corresponding simulation of another turbine.

As a final study on isolated wind turbines chapter 10 presents a simulation and analysis of the wake of a turbine operating in sheared and turbulent inflow.



The chapters 11-12 are devoted to investigating the flow field between a row of turbines. To begin with a row of three turbines is considered in a situation where the row is aligned with the mean wind, i.e. full wake operation. This study includes both laminar and turbulent inflow conditions.

Following this the wake of two turbines subject to a strongly sheared and low turbulent inflow are simulated in a case where the downstream turbine operates partly in the wake of the upstream one.

Finally, the main results of the thesis are summarized in chapter 13.

Appendix A provides some important quantities in the analysis of turbulent flows and discusses their application in the study of wind turbine wakes.

# Chapter 2

## Numerical Modeling

In this chapter the basis of the models used for the computations of wind turbine wakes is presented together with a description of the simulated wind turbines.

### 2.1 Actuator line model

The actuator line method, introduced by Sørensen and Shen [75], is a fully three-dimensional and unsteady aerodynamic model for studying the flow field around wind turbines. The method combines a three-dimensional Navier-Stokes solver with a so-called actuator line technique in which body forces are distributed radially along lines representing the blades of the wind turbine. Originally the method was formulated in vorticity-velocity variables but later Mikkelsen [56] reformulated it in primitive variables (pressure-velocity) in order to combine it with the flow solver EllipSys3D to be described later. The basis of the model is the incompressible Navier-Stokes equations

$$\frac{\partial \mathbf{V}}{\partial t} + \mathbf{V} \cdot \nabla \mathbf{V} = -\frac{1}{\rho} \nabla p + \nu \nabla^2 \mathbf{V} + \mathbf{f}, \quad \nabla \cdot \mathbf{V} = 0 \quad (2.1)$$

where  $\mathbf{f}$  denote the body forces, which represent the loading on the rotating blades.

The body forces acting on the blades are determined using a blade element approach combined with tabulated two-dimensional airfoil characteristics. Figure 2.1 shows a cross-sectional airfoil element at radius  $r$  in the  $(\theta, z)$  plane.

The local velocity relative to the rotating blade is determined from the shown velocity triangle as

$$V_{rel} = \sqrt{V_z^2 + (\Omega r - V_\theta)^2} \quad (2.2)$$

Here,  $\Omega$  denotes the angular velocity and  $V_z$  and  $V_\theta$  are the velocities in the axial and tangential direction, respectively. The flow angle between  $V_{rel}$  and the rotor plane is determined as

$$\varphi = \tan^{-1}\left(\frac{V_z}{\Omega r - V_\theta}\right) \quad (2.3)$$

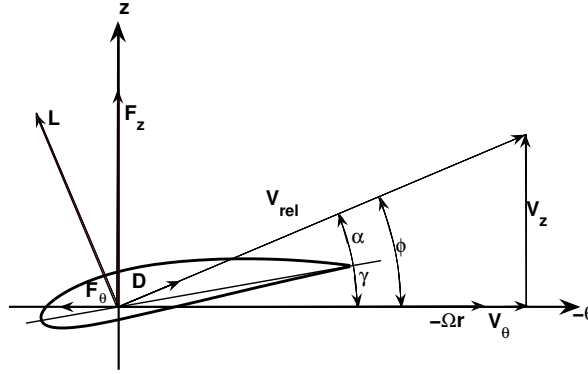


Figure 2.1: Cross-sectional airfoil element showing velocity and force vectors

The local angle of attack is given by  $\alpha = \varphi - \gamma$ , where  $\gamma$  denote the local pitch angle. It should be emphasized that the angle of attack, in the present work, is determined without subtracting the induction from the bound vortices. Having determined the angle of attack and the relative velocity the lift and drag force per spanwise length are found as

$$\mathbf{f}_{2D} = (L, D) = \frac{1}{2} \rho V_{rel}^2 c (C_L \mathbf{e}_L, C_D \mathbf{e}_D) \quad (2.4)$$

where  $C_L = C_L(\alpha, Re)$  and  $C_D = C_D(\alpha, Re)$  are the lift and drag coefficients, respectively,  $Re$  is the Reynolds number based on chord length  $c$  and  $\mathbf{e}_L$  and  $\mathbf{e}_D$  denote the unit vectors in the direction of respectively the lift and drag.

The applied aerodynamic blade forces need to be distributed smoothly on several mesh points in order to avoid singular behavior. In practice the aerodynamic blade forces are distributed along and away from the actuator lines in a three-dimensional Gaussian manner by taking the convolution of the computed local load,  $\mathbf{f}$ , and a regularization kernel  $\eta_\epsilon$  as shown below

$$\mathbf{f}_\epsilon = \mathbf{f} \otimes \eta_\epsilon, \quad \eta_\epsilon(d) = \frac{1}{\epsilon^2 \pi^{3/2}} \exp \left[ - \left( \frac{d}{\epsilon} \right)^2 \right] \quad (2.5)$$

Here  $d(= |\mathbf{x} - s\mathbf{e}_i|)$  is the distance between cell centered grid points and points at the  $i$ 'th actuator line and  $\epsilon$  is a parameter that serves to adjust the concentration of the regularized load. Hence, the regularized force per unit volume becomes

$$\mathbf{f}_\epsilon(\mathbf{x}) = \sum_{i=1}^B \int_0^R \mathbf{f}_{2D}(s) \eta_\epsilon(|\mathbf{x} - s\mathbf{e}_i|) ds \quad (2.6)$$

The influence of the parameter  $\epsilon$  will be studied in chapter 3.

The advantage of representing the blades by airfoil data, as it is done in the actuator line model, is that much fewer grid points are needed to capture the influence of the blades compared to what would be needed for simulating the actual geometry of the blades. Therefore, the actuator line model allows for a detailed study of the dynamics of the different wake structures, such as the tip and root vortices, using a reasonably number of grid nodes. Furthermore, the model benefits from being applicable with simple structured grids and therefore issues connected to grid generation do not occur. On the other hand, a drawback of the method is its reliance on

tabulated airfoil characteristics as well as the models connected to these data, which are needed for simulating complicated phenomena such as dynamic stall, transition and three-dimensional effects. However, as the main purpose of the present thesis is to study fundamental wake effects it is considered of minor importance to capture the loads on the rotor exactly.

## 2.2 Flow solver - EllipSys3D

The computations of the global flow field have been carried out using the 3D flow solver EllipSys3D developed by Michelsen [53], [54] and Sørensen [77]. This code solves the discretized incompressible Navier-Stokes equations in general curvilinear coordinates using a block structured finite volume approach. EllipSys3D is formulated in primitive variables (pressure-velocity) in a non-staggered grid arrangement.

In EllipSys3D the solution to the Navier Stokes equations is advanced in time using an iterative time-stepping method. In each time step a number of sub iterations are carried out where the momentum equations are used as a predictor and the rewritten continuity equation (pressure correction equation) is used as a corrector for the solution at the subsequent time step. The pressure correction equation is in the present work solved using the SIMPLE algorithm and pressure decoupling is avoided using the Rhie/Chow interpolation technique. The convective terms were discretized using a hybrid scheme combining the third order accurate QUICK (10%) scheme and the fourth order CDS scheme (90%). This scheme was employed as a compromise between avoiding the unphysical numerical wiggles, occurring when using the fourth order CDS and limiting numerical diffusion due to the upwinding nature of the QUICK. The influence of discretization scheme is discussed in 3.

Large eddy simulation (LES) was used to model the small unresolved length scales of turbulence. In LES the governing equations are obtained by filtering the time dependent Navier-Stokes equations in physical space such that those eddies which are below a certain size are filtered out. The resulting equations thus only govern the dynamics of the large scales, while the smaller scales are modeled by some eddy-viscosity based sub-grid scale model. In practice, the finite volume discretization of the flow equations works implicitly as a filter where the scales larger than the grid spacing are resolved while the scales below are modeled using an eddy-viscosity based sub-grid scale model.

A vast number of turbulence models for LES have been proposed as reviewed by Sagaut [67] and in the present work the subgrid scale (SGS) viscosity was modeled using the vorticity based mixed scale model by Phuoc [62]. In this model the SGS viscosity is given by

$$\nu_{sgs}(\mathbf{x}, t) = \rho C_m |\nabla \times \bar{\mathbf{V}}(\mathbf{x}, t)|^\alpha (q_c^2)^{\frac{1-\alpha}{2}}(\mathbf{x}, t) \bar{\Delta}^{1+\alpha} \quad (2.7)$$

Here  $\rho$  is the density,  $\bar{\mathbf{V}}$  is the filtered velocity,  $\bar{\Delta}$  is the filter cut-off length, which is set equal to  $\Delta Vol^{1/3}$ , where  $\Delta Vol$  is the volume of a given cell,  $C_m$  and  $\alpha$  are constants which here are set to respectively 0.01 and 0.5. The kinetic energy  $q_c^2$  is evaluated in physical space as

$$q_c^2(\mathbf{x}, t) = \frac{1}{2} (\bar{v}_i(\mathbf{x}, t))' (\bar{v}_i(\mathbf{x}, t))' \quad (2.8)$$

Here,  $(\bar{v})' = \bar{\mathbf{V}} - \tilde{\bar{\mathbf{V}}}$ , with  $\tilde{\bar{\mathbf{V}}}$  denoting the doubled filtered velocity, represents the high frequency part of the resolved velocity field. The additional filter designated with a tilde is referred to as

the test filter. The mixed scale model has been chosen because of its simplicity and because it both accounts for the dissipation of energy and the important interaction between the smallest resolved scales and the largest unresolved scales.

## 2.3 Modeling the atmospheric boundary layer

Several methods have been used in CFD to simulate the effect of the atmospheric boundary layer. The simplest method is to assume a laminar flow and just impose a given wind shear profile at the inlet and allowing for some development through the domain. This approach was used by Sørensen and Johansen [79] and Zahle and Sørensen [93] to study the wake of a wind turbine operating in extreme wind shear.

The usual approach for simulating the turbulent wind over rough terrain is to solve the incompressible RANS equations together with the high Reynolds number  $k - \epsilon$  turbulence model often combined with a law of the wall model to capture the inner near wall region, see e.g. [77]. Using this approach the mean equilibrium wind shear profile is related to the wall shear stress. More recently LES based models have also been applied for simulating the atmospheric boundary layer over complex terrain. In order to reduce computational costs these methods are often combined with models for the flow in the near wall region either in terms of a wall function or through the use of hybrid methods, which simulates the near wall region using RANS. A formulation of the former of these methods were in combination with an actuator disc approach used by Jimenez et al. [38], [39] for simulating the wake of a wind turbine operating in an atmospheric boundary layer.

A version of the more physical hybrid model was implemented in EllipSys3D by Bechmann [7] and used with success in the study of three atmospheric test cases. Though this model is basically capable of capturing a wide range of turbulent structures in the atmosphere such work still has not been combined with studies of wind turbine wakes.

In the present work the atmospheric boundary layer is modeled using a technique where body forces applied to the entire computational domain is used to impose a given but arbitrary steady wind shear profile, while free-stream turbulence is modeled by introducing synthetic turbulent velocity fluctuations to the mean flow upstream of the rotor.

### 2.3.1 Modeling the mean wind shear

The method of imposing a given wind shear profile by applying body forces was presented by Mikkelsen et al. [57] and is essentially based on the immersed boundary technique. Traditionally the immersed boundary technique is used to deal with problems in complex geometries since it offers a simple way of coping with boundaries that do not comply with the mesh layout. A review of the various applications of the immersed boundary technique is provided in [66].

Here, the technique of introducing body forces will be used to prescribe a desired mean velocity profile in the entire domain. Hence, the idea is to conduct an initial computation without the wind turbine included in the domain in order to establish the force field required to obtain the desired mean wind shear profile. The obtained steady force field is afterward stored and fixed in the subsequent computation where the wind turbine is included.

In the following the method will be described for the unsteady case, however, the method easily applies for the steady case as well.

In order to determine the body force required to obtain a desired velocity in a given computational cell consider again the incompressible Navier-Stokes equations

$$\frac{\partial \mathbf{V}}{\partial t} + \mathbf{V} \cdot \nabla \mathbf{V} = -\frac{1}{\rho} \nabla p + \nu \nabla^2 \mathbf{V} + \mathbf{f}, \quad \nabla \cdot \mathbf{V} = 0 \quad (2.9)$$

As mentioned in section 2.2 EllipSys3D solves this coupled set of equations using the SIMPLE/PISO predictor corrector method. In discretized form the integrated momentum equation yields a large system of linear equations

$$A_P V_P^{t+\Delta t} + \sum_i A_i V_i^{t+\Delta t} = S_P + f_P \quad (2.10)$$

Here  $V$  denotes any of the three velocity components,  $S$  is a source term that includes the pressure and body forces and  $f$  refer to the external body force which is to be adjusted to establish a desired velocity. The subscript  $P$  denotes the current cell and the identifier,  $i = E, W, N, S, B, T$ , refer to the neighboring cells. From the discretized momentum equation the external force required to establish the desired velocity  $U_0$  in the computational cell  $P$  at a given time step is predicted as

$$f_P = A_P U_0 + \sum_i A_i V_i^{t+\Delta t} - S_P \quad (2.11)$$

This procedure is carried out for all cells in the domain and continued until a converged steady state shear profile is obtained.

The above method for imposing a prescribed wind shear is easy to implement and generally has good convergence properties. Though, it evidently does not simulate the real physics of the atmospheric boundary layer it is believed to capture the most important features in relation to the simulation of wind turbine wakes.

In order to illustrate the use of the method and to evaluate the expected influence of the forces needed to sustain a given velocity profile consider a simple fully developed laminar flow above an infinite flat plate as sketched in figure 2.2. The wall is considered infinite in the horizontal

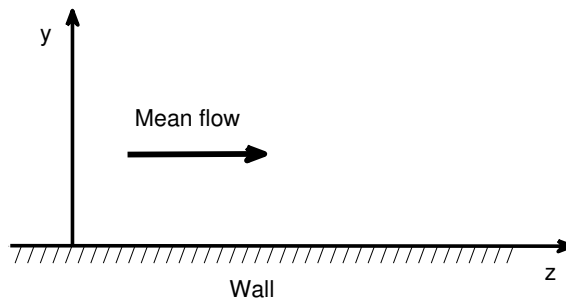


Figure 2.2: Sketch of idealized flow over a flat plate

directions with no variation in any flow properties in these directions. In this case  $V_x = V_y = 0$  and the Navier-Stokes equation reduces to the following ordinary differential equation

$$\nu \frac{d^2 V_z}{dy^2} + f = 0 \quad (2.12)$$

where  $f$  represents the prescribed body forces

Assuming, as it is done in all the computations involving modeling of the atmospheric boundary layer presented in this thesis, that the mean velocity profile may be expressed in terms of a power law profile

$$V_z = V_\infty \zeta(\eta), \quad \zeta(\eta) = \eta^\alpha, \quad \eta = \frac{y}{H} \quad (2.13)$$

where  $H$  is the hub height of the wind turbine. Then differentiating twice gives the following expression for the body forces needed to sustain the given velocity profile.

$$f(\eta) = -\alpha(\alpha - 1)\nu \frac{V_\infty}{H^2} \eta^{\alpha-2} \quad (2.14)$$

Now, what is most relevant for the present work is the expected influence of the applied forces on a wind turbine wake. This is evaluated by computing the added effect,  $E_{flow}$  per unit volume required to maintain the power law profile and integrate across a volume representative for the wake. Considering a wake region with a volume of  $Vol = D^2 L$  having center at hub height  $H$ . In this case the total effect of the prescribed force field on the wake is

$$\begin{aligned} E &= \int_{Vol} E_{flow} dVol = \mu D L \int_{H-R}^{H+R} V_z \frac{d^2 V_z}{dy^2} dy = \\ &\mu V_\infty^2 \frac{DL}{H} \int_{1-R/H}^{1+R/H} \zeta \frac{d^2 \zeta}{d\eta^2} d\eta = \mu V_\infty^2 \frac{DL}{H} \beta \end{aligned} \quad (2.15)$$

where

$$\beta = \int_{1-R/H}^{1+R/H} \zeta \frac{d^2 \zeta}{d\eta^2} d\eta = \left[ \frac{\alpha(\alpha - 1)}{2\alpha - 1} \eta^{2\alpha-1} \right]_{1-R/H}^{1+R/H} \quad (2.16)$$

Expressing the effect from the wind turbine wake system as

$$P = \frac{1}{2} \pi \gamma R^2 \rho V_\infty^3 C_P \quad (2.17)$$

where  $\gamma$  is the fraction of energy transferred to the wake and  $C_P$  is the power coefficient. Then, the relative effect of  $E$  compared to  $P$  is

$$\varepsilon = \frac{E}{P} = \frac{\mu V_\infty^2 \frac{DL}{H} \beta}{\frac{1}{2} \pi R^2 \rho V_\infty^3 C_P \gamma} = \frac{4\beta}{\pi C_P \gamma} \frac{L}{H} \frac{1}{Re} = \frac{\varepsilon_0}{Re}, \quad \varepsilon_0 = \frac{4\beta}{\pi C_P \gamma} \frac{L}{H} \quad (2.18)$$

Thus, the effect of the force field given by equation 2.14 on the wake system is inversely proportional to the Reynolds number. This is not surprising since at high Reynolds numbers the flow only undergoes limited development and hence the forces needed to maintain a given inlet profile are small.

To get a more complete impression of the magnitude of  $\varepsilon$  figure 2.3 displays a representative plot of  $\varepsilon_0$  as a function of  $\alpha$ . For the shown case the maximum effect of the prescribed force field on the wake is in the order of  $20/Re$ . Therefore, considering the magnitude of the Reynolds numbers ( $O(10^5)$ ) of the computations presented in this thesis it seems reasonable to use body forces to prescribe the mean shear profile.

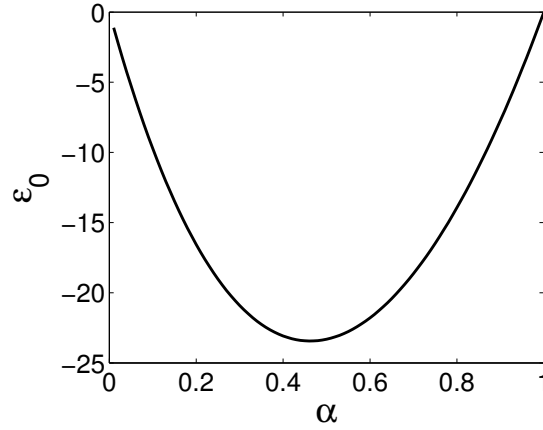


Figure 2.3: Variation of  $\varepsilon_0$  as a function of  $\alpha$ ;  $H/R = 2$ ,  $L/H = 5$ ,  $C_P = 0.5$  and  $\gamma = 0.15$

### 2.3.2 Modeling the atmospheric turbulence

The atmospheric turbulence is modeled by introducing artificial turbulent fluctuations upstream the wind turbine.

#### Generation of inflow turbulence

The introduced turbulence was generated using the method of Mann [48], [49], which is based on a model of the spectral tensor. This algorithm models the spectral tensor (three-dimensional spectrum) using rapid distortion theory, implying a linearization of the Navier Stokes equation, combined with an assumption of linear shear and a model for eddy lifetime.

The algorithm of Mann is capable of simulating all three velocity components of a three-dimensional incompressible turbulence field, which is homogeneous, stationary, Gaussian, anisotropic and has the same second order statistics as the atmosphere. The output of the algorithm is a spatial box of equidistantly spaced turbulence. Here, the  $z$ -axis is in the direction of the mean wind speed and is inferred as a time axis via Taylor's frozen turbulence hypotheses.

It should be noted that, since the simulated turbulent fluctuations are periodic in all directions, turbulence is generally generated in a box with each of the cross flow dimensions twice the size wanted and then only one quarter (the lower left corner) of the box is used as input in the later modeling of the inflow turbulence.

#### Applying the turbulent fluctuations

The usual approach adopted when applying turbulent fluctuations from a pre-generated pseudo turbulence field is simply to superimpose the fluctuating velocities to the mean velocities at the inlet boundary [41]. Here, however, it is, as illustrated in figure 2.4, proposed to introduce the turbulence field in a plane located just upstream of the rotor and not at the inlet, whereby the turbulent fluctuations are better preserved prior to impacting the rotor.

Furthermore, instead of adding turbulent fluctuations directly to the mean flow, it is proposed to use unsteady concentrated body forces for generating the prescribed turbulent fluctuations. The reason for using this approach is mainly to avoid possible problems with lack of continuity;



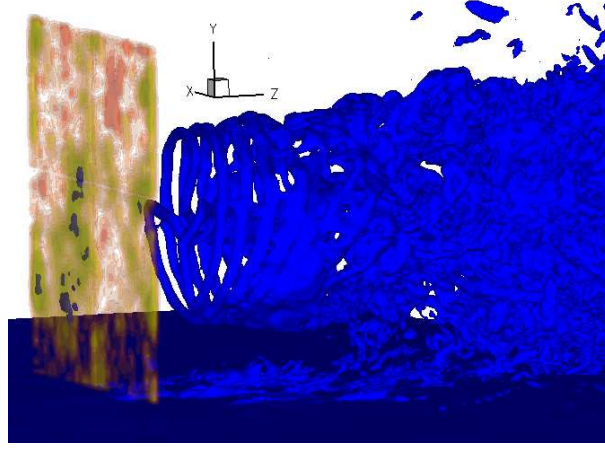


Figure 2.4: Iso-surfaces of vorticity magnitude of wake of wind turbine operating in sheared and turbulent inflow.

Even though the turbulence generator by Mann automatically produces incompressible fields, continuity is generally not conserved in a discretized domain. This is not a problem when used in an aero-elastic model but can be problematic in a numerical simulation and therefore introducing the synthetic turbulence in terms of body forces rather than, as a mass source/sink seems beneficial.

The basis of the proposed method is identical to that used for prescribing the steady shear profile. From the discretized momentum equation the external force required to establish a fluctuation  $u_0$  about the mean  $V$  in the computational cell  $P$  at a given time step is predicted as

$$f_P = A_P(V + u_0) + \sum_i A_i V_i^{t+\Delta t} - S_P \quad (2.19)$$

During the following sub-iterations the instantaneous solution will converge toward the desired velocity.

The above procedure is carried out at each time step for all mesh points in the given plane upstream of the rotor. To circumvent possible problems of singular behavior the applied forces are smeared in the direction normal to the plane using a one-dimensional Gaussian approach. Hence the forces are distributed away from the plane by using the convolution

$$\mathbf{f}_\epsilon = \mathbf{f}_P \otimes \eta_\epsilon, \quad \eta_\epsilon(z) = \frac{1}{\epsilon\sqrt{\pi}} \exp \left[ - \left( \frac{z - z_d}{\epsilon} \right)^2 \right] \quad (2.20)$$

Again  $\epsilon$  is a parameter that serves to adjust the concentration of the regularized load and  $d = z - z_d$  is the normal distance from a grid point to the turbulence plane. In the present work the parameter  $\epsilon$  is set equal to the side length of a grid cell.

Since the resolution of the grid used for generating the turbulence normally is coarser than the grid used in the subsequent numerical simulation of the wind turbine both spatial and temporal interpolation is required. For a given time  $t$  in the simulation, two successive planes from the turbulence box corresponding to the turbulent field at time  $T_i$  and  $T_{i+1}$ , where  $T_i < t < T_{i+1}$  is used as input. For each of these planes bilinear interpolation is used to get the velocity in point  $P$  at respectively time  $T_i$  and  $T_{i+1}$ . Thereafter these velocities are interpolated in time to get the velocity at time  $t$ .

## 2.4 Computational domains

All computations in the present work have been conducted in Cartesian computational domains and here some of their common features will be described. Two different grid configurations have been used depending on the given flow problem: one for computations on wind turbines operating in non-sheared inflow and one for wind turbines operating in sheared inflow. The overall layouts of the two configurations are sketched in figure 2.5, which also serves to define the used coordinate system.

The dimensions of the grids are  $L_x \times L_y \times L_z$ , where  $L_z$  denotes the domain length (in the flow direction),  $L_y$  the domain height and  $L_x$  the domain width. The actuator lines were in all cases

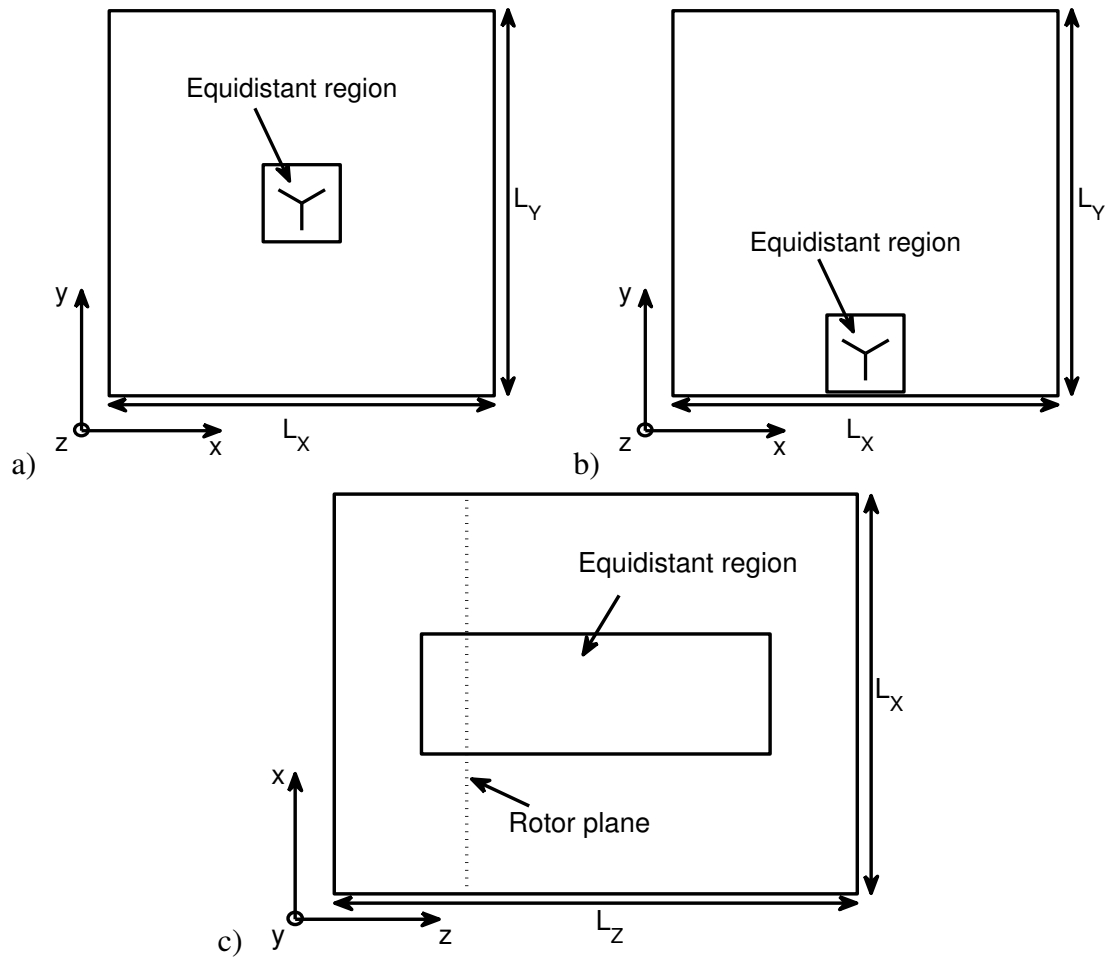


Figure 2.5: Sketches of computational domains; a) Cross-section of grid for uniform inflow; b) Cross-section of grid for sheared inflow; c) Top view of the two grid layouts.

rotating in the  $z$ -plane and positioned as indicated in the figures. In order to resolve the strong gradients in the vicinity of the actuator lines and in the same time preserving the generated flow structures in the wake a high concentration of grid points were distributed equidistantly in the region around and downstream the rotor. The dimensions of the equidistant region, occasionally referred to as the near domain, are chosen according to the given flow problem but in general its height and width extents outside the rotor plane in order to account for wake expansion. Outside the equidistant region grid points were stretched away toward the outer boundaries. In all the

computations the resolution in the near domain corresponded to 30 grid points per rotor radius. In order to facilitate parallelization of the computations the grid was divided into a number of blocks with an equal number of grid points in each direction.

For the computations on turbines subject to uniform mean inflow the following boundary conditions were applied:

- At the inlet boundary the velocity in the  $z$ -direction was assumed uniform and equal to the free-stream velocity i.e.  $V_z = V_\infty$ , while the velocity components in the  $x$  and  $y$  direction were zero, i.e.  $V_x = V_y = 0$ .
- At the outlet boundary Neumann conditions were imposed, i.e.  $\frac{\partial V_x}{\partial z} = \frac{\partial V_y}{\partial z} = \frac{\partial V_z}{\partial z} = 0$
- At the lateral boundaries ( $x/R = -L_x/2, x/R = L_x/2$ ) periodicity were imposed.
- The lower and upper boundaries were applied with symmetry conditions, implying that  $V_y = 0$  and  $\frac{\partial V_x}{\partial y} = \frac{\partial V_z}{\partial y} = 0$

In the computations involving a sheared inflow the following changes were made to the above boundary conditions:

- At the inlet boundary the velocity in the  $z$ -direction was specified according to the wanted shear profiles i.e.  $V_z = V_z(y)$ , while the velocity components in the  $x$  and  $y$  direction were zero.
- At the lower boundary the usual wall condition was imposed, while the upper boundary was prescribed according to the velocity profile i.e.  $V_z = V_z(L_y)$  and  $V_x = V_y = 0$ .
- The outlet were applied with unsteady convective conditions, i.e.  $\frac{\partial \mathbf{V}}{\partial t} + \mathbf{U} \frac{\partial \mathbf{V}}{\partial z} = 0$ , where  $\mathbf{U}$  is a velocity that is independent of location on the outflow surface and is chosen to maintain overall mass conservation. The necessity of imposing this boundary condition in case of sheared flow is shown in chapter 3.

## 2.5 Wind turbines

The computations presented in this thesis were conducted using airfoil data from respectively the Tjæreborg and the NM80 wind turbine.

The Tjæreborg turbine has a blade radius of  $R = 30.56 \text{ m}$  and rotates at  $\Omega = 22.1 \text{ RPM}$ , corresponding to a tip speed of  $70.7 \text{ m/s}$ . The blade sections consist of NACA 44xx airfoils with a chord length of  $0.9 \text{ m}$  at the tip, increasing linearly to  $3.3 \text{ m}$  at hub radius  $6 \text{ m}$ . The blades are linearly twisted  $1^\circ$  per  $3 \text{ m}$ .

Figure 2.6 shows the lift and drag polars used for respectively the NACA 4412 and the NACA 4424 airfoil. These airfoils represent blade sections near the tip and the root, respectively. In the range of angles of attack between approximately minimum and maximum  $C_L$  the data are taken directly from wind tunnel measurements provided by Abbott and von Doenhoff [1]. Outside of this range the airfoil data have been corrected for three-dimensional effects. Further technical details of the rotor can be found in [95].

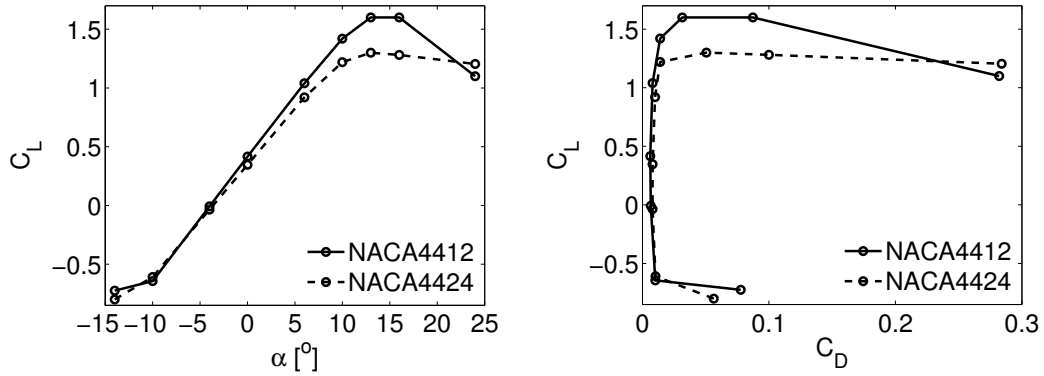


Figure 2.6: Lift and drag polars used in the computations for representing respectively the NACA 4412 and the NACA 4424 airfoil.

The radius of the NM80 turbine is  $R = 40.04m$  and it has a variable rotational speed depending on the wind speed; at a wind speed of  $V_\infty = 5 m/s$  the rotational speed is 11.2 RPM, while it at  $V_\infty = 20 m/s$  is 17.2 RPM. Further details about the NM80 turbine can be found in [29].

## 2.6 Summary

The different parts of the model used for the simulations of the wind turbine wakes have been presented. The principles of the actuator line method were described and its advantages related to simulation of wind turbine wakes were discussed. Following this the 3D Navier Stokes solver EllipSys3D, in which the actuator line model is implemented, was presented together with a short description of the sub-grid scale model applied for modeling the small scale turbulence. Next, the technique of using body forces to model the atmospheric boundary layer including turbulence was presented along with a description of its implementation in EllipSys3D. Finally, the overall layout of the used numerical grid configuration was described followed by a description of the wind turbines used in the wake studies.

# Chapter 3

## Numerical sensitivity

In order to establish the overall requirements for the various grid and solver parameters used with the actuator line computations a parametric study of their influence on the computed results have been conducted. Unless otherwise stated, all the computations in this study considered a uniform inflow velocity of  $V_\infty = 10 \text{ m/s}$  and were carried out using airfoil data from the Tjæreborg wind turbine.

### 3.1 Domain dimensions

The size of the computational domain should be large enough to avoid the influence of the boundaries on the local flow through and downstream the turbine. Here, only the influence of the cross-sectional area of the domain was investigated since the outlet boundary in all the computations presented in this thesis generally is located very far from the rotor in question. The layout of the meshes is as sketched in figure 2.5 with the number of grid points in each direction being 128. They all had quadratic cross-sections ( $L_x = L_y$ ) and a fixed length of  $L_z = 18R$ .

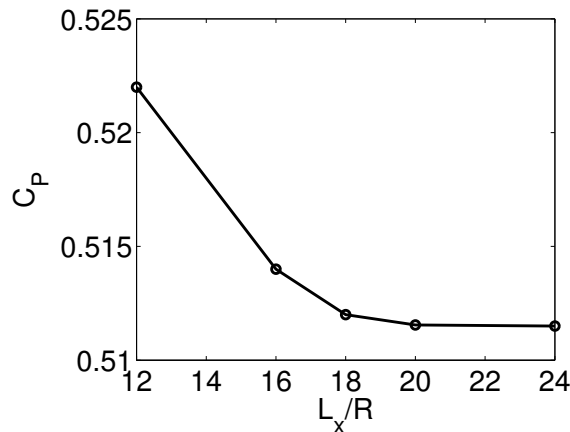


Figure 3.1: Predicted power coefficient as a function of domain width.

Figure 3.1 shows the predicted power coefficient as a function of side length. As seen a side length greater than  $18R$  seems to be sufficient to obtain convergence in the predicted power.

## 3.2 Regularization parameter

Ideally, the regularization parameter,  $\epsilon$ , should be chosen such that the applied forces are distributed over an area representing the chord distribution and in the ultimate case of course resemble the chordwise pressure distribution, as in the actuator surface approach. However, due to limited computer resources this is not an option and hence it is of interest to study how the choice of the parameter affects the result.

The influence of  $\epsilon$  has previously been studied for an axisymmetric actuator disc by Sørensen and Shen [75] and for the actuator line method formulated in a polar frame of reference by Ivanell [35] and Mikkelsen [56].

Here, the sensitivity of the computed solutions to the regularization parameter was investigated in a cubic mesh with side lengths 18 rotor radii and a layout identical to the one used for the study of the influence of the domain size.

Figure 3.2 compares the distribution of the axial interference factor,  $a_z = (1 - V_z/V_\infty)$ , along an actuator line for four different values of  $\epsilon$ . The values of  $\epsilon$  are scaled with the resolution of the actuator lines  $\Delta r$ , which is equal to the length of a cell in the equidistant region. From the

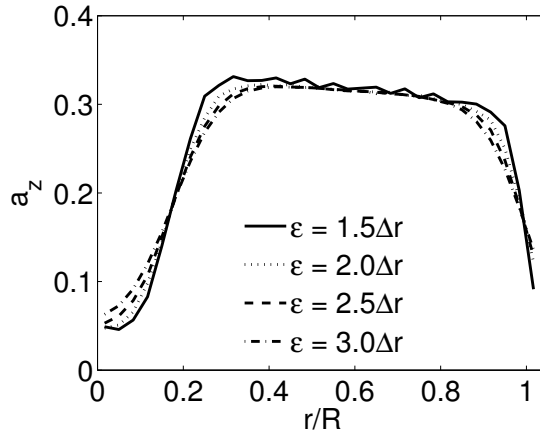


Figure 3.2: Radial distribution of the axial interference factor along an actuator line for different  $\epsilon$  values.

figure it is seen that increasing  $\epsilon$  result in a more smooth variation of the velocity near the root and tip. For  $\epsilon = 1.5\Delta r$  the radial distribution display significant oscillations, thus indicating that this value of  $\epsilon$  is too small. On the other hand, if  $\epsilon$  is chosen too large the applied forces will be smoothened considerably and thereby the distinct pattern of the tip and root vortices may be smeared out. Choosing  $\epsilon = 2\Delta r$  appeared to offer good compromise between reducing oscillations and limit the smoothing of the loading.

### 3.3 Time step

In connection with unsteady Navier-Stokes computations an often used criterion for time advancement schemes is that the Courant-Friedrich-Levy-number (CFL) should not exceed 1, requiring that a disturbance must not be convected more than one grid spacing during a single time step.

However, when using the actuator line method with a Cartesian grid the time step size is mainly restricted by the tip speed ratio of the rotor since the movement of the blade tip during one time step should not exceed one grid spacing. Therefore, the minimum number of time steps per rotor revolution should be greater than  $2\pi R/\Delta r$ , which with the given grid resolution ( $\Delta r/R = 1/30$ ) corresponds to 188.5 time steps per rotor revolution. This latter requirement for the time step is far more restrictive than the CFL condition and in all of the computations performed in this thesis the maximum CFL number rarely exceeded 0.2.

The influence of time step was investigated in the same grid as used for the study on the regularization parameter. In the study the number of time steps per rotor revolution was varied from 204 to 1020.

Figure 3.3 displays the lift distribution along the blades of the wind turbine for various time steps. As seen in the range of tested time resolution any difference is barely seen and it was

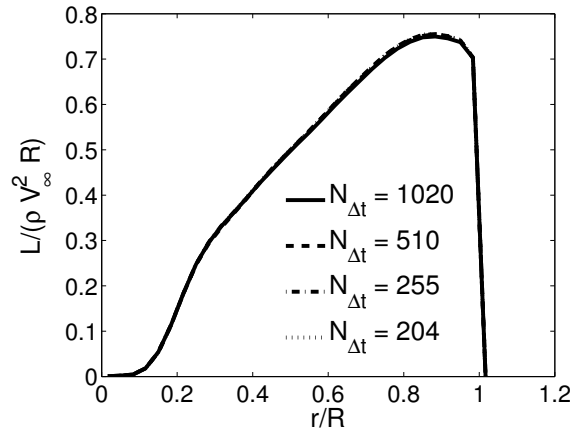


Figure 3.3: Lift distribution along an actuator line for various time steps.

concluded that a time step corresponding to 204 time steps per rotor revolution was sufficient to obtain accurate solutions.

### 3.4 Pressure solver

In the majority of the computations presented in this thesis the pressure correction equation has as mentioned in section 2.2 been solved using the SIMPLE algorithm. For unsteady problems, however, it is common to apply the more accurate PISO algorithm and therefore it was studied whether using the latter algorithm affected the computed result. The study was carried out in the same computational mesh as used for the computations presented in chapter 4, i.e. a grid with a high resolution of the region extending from the rotor plane and 7 diameters downstream. The study showed that, though changing to the PISO algorithm causes a general decrease in the

residuals of the pressure; it has no effect on the rotor loading and the flow behavior. The reason for this is that the CFL number of the actuator line computations is always very low (see section 3.3) and therefore a more accurate treatment of the pressure correction equation is not needed. Since the computational costs of the PISO algorithm is nearly twice that of the SIMPLE algorithm it is recommended to use the latter algorithm. It should be appreciated, however, that in other flow problems it could be advantageous to combine an increased time step with the PISO algorithm.

### 3.5 Reynolds number

Most of the computations presented in this thesis have been carried out at a Reynolds number based on rotor radius of  $10^5$ . This Reynolds number is of course considerably lower than experienced in the field and it might be expected to have an impact on the computed rotor loads and turbulent length scales in the wake.

However, as discussed by Sørensen et al. [74] and Mikkelsen [55] the Reynolds number used in the actuator line computations have, due to the absence of boundary layers, only a minor influence on the overall wake behavior provided it has reached a certain critical minimum.

In "real life" the Reynolds number of course affects the small scale structures in the wake,

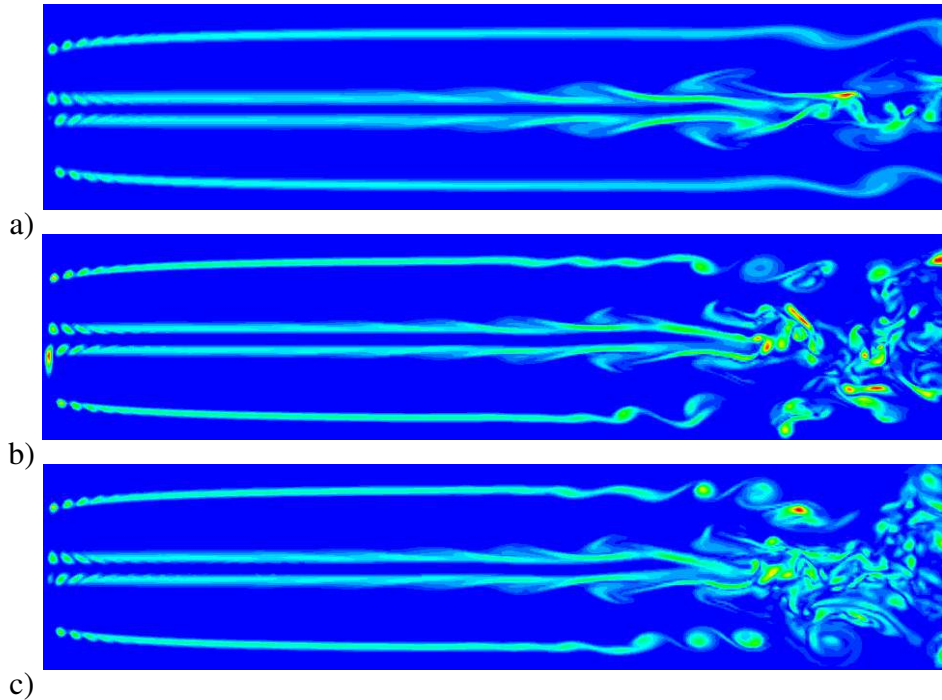


Figure 3.4: Vorticity contours in the wake of the turbine using QUICK; a)  $Re = 10^4$ ; b)  $Re = 10^5$  and c)  $Re = 10^6$ . Regions of high vorticity appear as light colors.

which are smaller for larger Reynolds numbers. Nevertheless, in the computations the filter width, grid spacing and differencing scheme rather than the Reynolds number are the main parameters governing the smallest length scales.

This is illustrated qualitatively in figure 3.4, which depicts the contours of the absolute vorticity in the wake for Reynolds numbers in the range  $10^4 - 10^6$ . The shown results have been com-



puted on a grid identical to the one used in chapter 4 and using the QUICK scheme. As seen the overall flow behavior is the same though at  $Re = 10^4$  the wake is clearly more diffusive and the observed instabilities in the wake are moved downstream.

### 3.6 Differencing scheme

As shown in section 3.5, the smallest resolvable scales in the computations presented here are too large for molecular viscosity to be important and hence energy dissipation mainly stems from the SGS-model and from numerical diffusion. In order to limit the latter contribution the convective terms in the Navier-Stokes equations should generally be discretized using schemes with as low numerical diffusion as possible.

Central difference schemes benefit from having small truncation errors (producing low numerical diffusion) but on the other hand tend to produce unphysical numerical wiggles due to their unboundedness. This is shown in figure 3.5, which displays the downstream contours of respectively the axial velocity and vorticity in a plane going through the wind turbine center axis computed using a fourth-order central difference scheme (CDS4) and a grid identical to the one used in chapter 4. In the present case the numerical wiggles gradually build up with time and eventually demolish the solution. The oscillations depend on the local Peclet number  $Pe = \rho V_z \Delta z / \mu$  and it can be shown [20] that a sufficient but not necessary condition for boundedness is  $Pe \leq 2$ . This criterion, however, is obviously not fulfilled for the grid resolution and Reynolds number used in the present computations.

When using the QUICK scheme the numerical wiggles are avoided, however, due to its up-

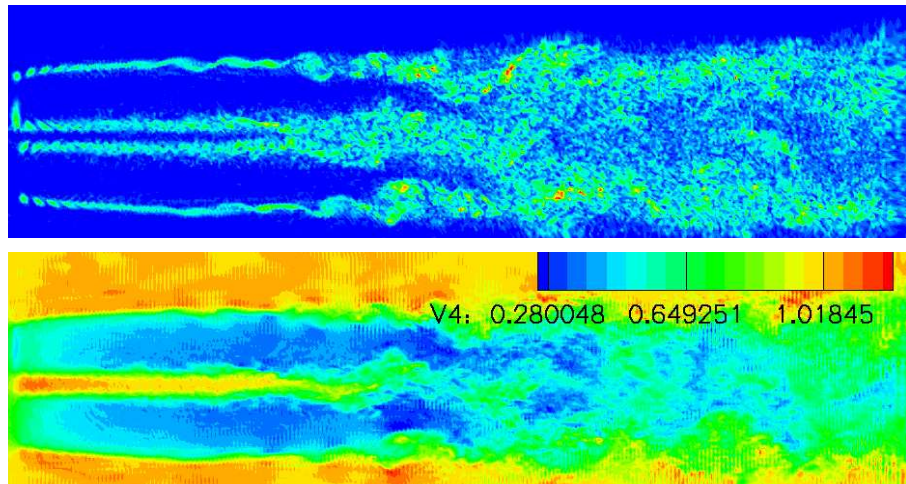


*Figure 3.5: Contours of respectively absolute vorticity (top) and axial velocity (bottom) in the wake of the turbine using CDS4. High vorticity values appear as light colors.*

wind nature, this scheme introduces artificial viscosity, which may cause a loss of details of the turbulent structures.

To overcome the problem of on one hand avoiding the unphysical numerical wiggles of the CDS4 and on the other hand limit the numerical diffusion of the QUICK it was decided to use a hybrid scheme combining 90% of the former and 10% of the latter scheme. As seen in figure 4.4 when using this hybrid scheme the wiggles are avoided, while due to the reduced false viscosity the vortex system seems more distinct and also breaks up close to the rotor than when a

pure QUICK scheme is applied.

### 3.7 Grid configuration and resolution

As mentioned in section 2.1 one of the advantages of the actuator line method is that it does not require a mesh of the actual blade geometry and thus in principle can be applied with any grid configuration. However, the selected grid of course influences the accuracy of the numerical solution and therefore it is worthwhile to study the sensitivity of the solution to the used grid. It should be appreciated that the computed solution always will exhibit a dependency on grid configuration and resolution, but what is important here is to quantify the error committed.

Here, the impact of mesh configuration was studied by comparing the results from the computations obtained on the grid as the one used in chapter 4 with those obtained on respectively a Cartesian and a regular polar grid both having higher resolutions.

The fine Cartesian grid had a layout identical to the one used in chapter 4 (and sketched in figure 2.5) except that each block of the grid contained  $80^3$  grid points resulting in a resolution of 40 grid points per rotor radii in the equidistant region.

The polar mesh had an axial extend of 43.3 rotor radii and lateral boundaries located 15 rotor radii away from the center line. The equidistant region extended 1.3 rotor radii in the radial direction and from half a rotor radius upstream to 7 rotor radii downstream of the rotor plane. The resolution in this region corresponded to 70 grid points per rotor radii. The final polar grid consisted of 40 blocks each with  $64^3$  cells resulting in a total of  $10.5 \cdot 10^6$ . It should be mentioned that in the polar formulation the actuator lines were fixed in the mesh while a rotational velocity at the boundaries created the rotational reference frame. Furthermore, the mesh comprised only one third of the rotor area, which was established by imposing periodic boundary conditions in the circumferential direction. Further details about the polar computation can be found in [36]. The distributions of the axial interference factors predicted in respectively the rotor plane and 6 rotor radii downstream using respectively the two Cartesian grids and the polar grid is compared in figure 3.6. The corresponding plot for the tangential velocity component is presented in figure 3.7. The shown distributions are averaged in the tangential direction.

As seen the agreement between the results obtained on different grids are quite good though the computation in the polar grid generally predicts lower axial and tangential induction than for the other configurations.

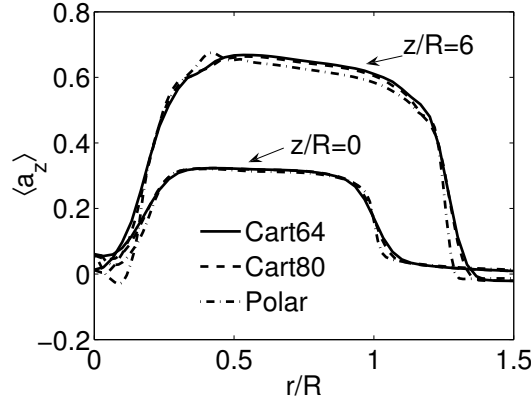


Figure 3.6: Influence of grid configuration and resolution on predictions of the radial distribution of the circumferential averaged axial interference factor in respectively the rotor plane and in the plane 6 rotor radii downstream of the rotor.

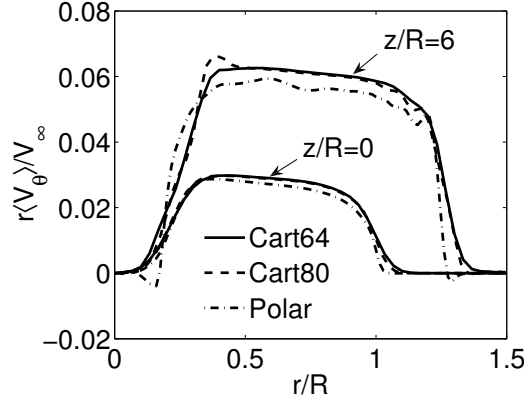
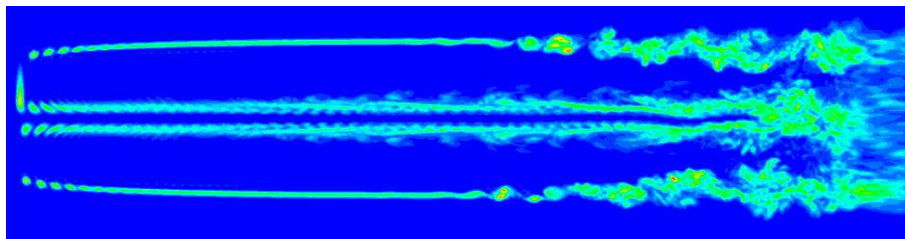


Figure 3.7: Influence of grid configuration and resolution on predictions of the radial distribution of the circumferentially averaged tangential velocity in respectively the rotor plane and in the plane 6 rotor radii downstream of the rotor.

It should be noticed that the regularization parameter is not the same in the three cases. For the Cartesian grids  $\epsilon = 2\Delta r$ , while it in the polar grid was  $\epsilon = \Delta r$ , where  $\Delta r$  is the cell length in the equidistant region. Therefore the forces are more concentrated on the finer grids and this might also affect the result. Another source for the observed deviations could be that the computation on the polar grid is carried out without application of a turbulence model.

Figure 3.8 shows the wake development computed on the fine Cartesian grid by displaying vorticity contours in the  $x/R = 0$  plane. This figure provides a qualitative validation of the computation by comparison with the corresponding plot obtained on the coarser Cartesian grid in figure 4.4.



*Figure 3.8: Downstream development of the wake at  $V_\infty = 10\text{m/s}$  computed using the fine grid. The rotor is located to the left. Regions of high vorticity appear as light colors.*

As seen the overall wake development is the same, however, there are also noticeable differences. On the fine grid the tip vortices are more concentrated and hence their distinct pattern appears clearer. Furthermore, when using the fine grid, the tip vortices are observed to break down closer to the rotor, while the root vortices appear somewhat more stable. However, considering the rather small deviations in figure 3.6 and 3.7 and due to the significantly increased computing costs associated with using the fine grid it was justified to use the coarser grid.

### 3.8 Boundary conditions

As mentioned in section 2.4 the traditional Neumann condition is used at the outlet in most of the computations presented in this thesis. This boundary condition, however, is known to cause unphysical behavior of the computed flow field near the outlet. Nevertheless, this was not considered a problem here, since the computational meshes used in the present thesis, always is stretched away from the near domain and toward the outer boundaries in order to avoid their influence on the region of interest.

Nonetheless, in connection with the computations of wind turbines operating in sheared inflow it was still found necessary to use the convective boundary condition. An example of this is illustrated in figure 3.9, which shows the streamwise velocity contours in a horizontal plane going through the center of two NM80 turbines operating in strong shear and low ambient turbulence. The details about this computation are presented in chapter 12.

From the figure it is evident that, when the Neumann condition is employed at the outlet, the flow is disturbed significantly in the region close to the outlet and far from the wake. These disturbances evolve upstream and eventually destroy the solution. The same pattern is clearly not observed when the convective boundary condition is applied.

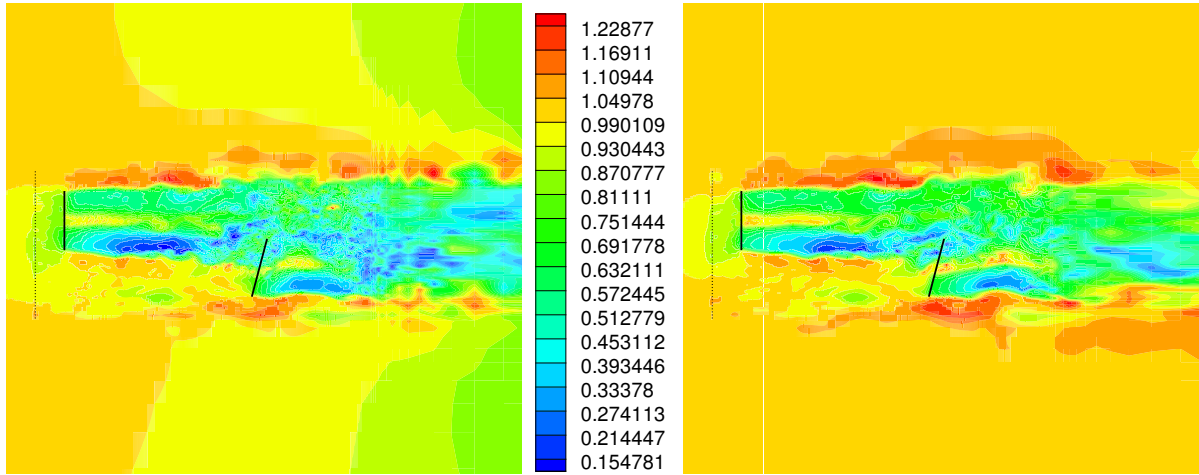


Figure 3.9: Contours of axial velocity in a horizontal plane intersecting the hub of two NM80 turbines using respectively Neumann (left) and convective (right) outflow boundary conditions.

### 3.9 Summary

This chapter presented a thorough study of the sensitivity of the numerical solutions to various solver and grid parameters.

Initially, it was shown that the cross sectional area should be at least  $18R \times 18R$  in order to avoid the influence of the boundaries on the computed solutions.

Secondly, it was revealed that the smearing parameter should be about twice the grid spacing in order to reduce oscillations along the blades without smearing out too much the loading.

Thirdly, a time step study showed that a time step corresponding to about 200 time steps per rotor revolution was sufficient to obtain accurate solutions. It was mentioned that the time step mainly is restricted by the tip speed ratio and that the CFL number therefore is very low (typically less than 0.2). Due to the low CFL number it was argued that the SIMPLE algorithm was sufficient for solving the pressure equation and therefore this scheme was chosen instead of the more accurate PISO algorithm.

Following this, it was shown that the computed solutions are fairly insensitive to changes in radius based Reynolds number provided it is at least  $10^5$ .

Thereafter, the sensitivity of the solutions to the used differencing scheme was discussed. In order to both avoid numerical wiggles and limit numerical diffusion it was proposed to use a hybrid scheme combining the CDS4 and QUICK scheme.

The influence of grid resolution and layout on the numerical solution obtained with the Cartesian grids used in the present thesis (figure 2.5), was studied by comparing with results predicted on respectively a Cartesian and a Polar mesh both having a finer resolution. The study revealed some grid dependency but the deviations were small enough to justify the use of the coarser grid.

Finally, it was shown that in the computations on wind turbines subject to wind shear it is necessary to use a convective outflow boundary condition to obtain good results.

## Chapter 4

# Wind Turbine Wake Aerodynamics in Uniform Inflow - Initial Results

This chapter presents the initial results from a series of actuator line computations carried out on the Tjæreborg wind turbine operating in a uniform inflow of respectively  $V_\infty = 6 \text{ m/s}$ ,  $10 \text{ m/s}$ ,  $14 \text{ m/s}$  and  $22 \text{ m/s}$ , corresponding to tip-speed ratios of respectively 11.78, 7.07, 5.05 and 3.21.

The objective of this chapter is to show the capabilities of the actuator line method and to establish the initial documentation of the near and far wake development for a wind turbine operating at four very different conditions. In the next two chapters a more thorough analysis of the obtained data will be presented focusing on respectively the tip vortex properties and wake turbulence characteristics.

### 4.1 Numerical Setup

The computations were carried out in a Cartesian computational domain as sketched in figure 2.5a and 2.5c. The dimensions of the grid was  $(L_x, L_y, L_z) = (18R, 18R, 26.8R)$ , where the  $z$ -coordinate is in the flow direction. The actuator lines were rotating in the  $z$ -plane located 7 rotor radii downstream of the inlet and the point of rotation was in the center of the plane.

The grid was divided into 32 blocks (2 in the  $x$  and  $y$  direction respectively and 8 in the  $z$ -direction) with 64 grid points in each direction. Thus, the used mesh contained  $128 \times 128 \times 512$  grid points corresponding to a total of  $8.4 \cdot 10^6$ .

The equidistant region (see figure 3.4), in which grid points were concentrated to resolve and preserve the generated flow structures, extended from 1R upstream the rotor to 14R downstream. Furthermore, the cross-sectional area of this region was set to  $2.6R \times 2.6R$  in order to account for wake expansion.

### 4.2 Validation - comparison with measurements

The numerical solutions obtained on the used grid have already been validated in terms of a numerical sensitivity study in chapter 3. However, in order to further validate the numerical results the power production of the Tjæreborg wind turbine was computed and compared to experiments. Figure 4.1 shows the measured and computed power coefficient as a function of

wind speed. Generally there is a good agreement between measurements and computations. The discrepancies are most probably due to inaccurate airfoil data, which are found from two dimensional flows in a wind tunnel and therefore becomes unreliable when three-dimensional effects comes into play.

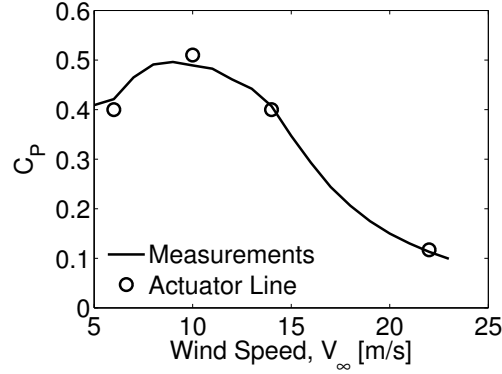


Figure 4.1: Comparison of measured and computed power coefficient for the Tjæreborg wind turbine.

### 4.3 Blade loading

Figure 4.2 shows the time averaged radial distribution of the axial interference factor,  $a_z = 1 - V_z/V_\infty$  along the blades of the turbine. In the case where  $\lambda = 11.78$  the induction is seen to undergo a rather significant increase toward the tip reaching levels BEM methods only can handle by using empirical corrections. For the rotor operating at  $\lambda = 7.07$ , where the Tjæreborg turbine has nearly optimal performance, the distribution of the axial interference factor is almost uniform, while moderate variations is observed at  $\lambda = 5.05$ . At  $\lambda = 3.21$  the maximum induction takes place at approximately  $r/R = 0.25$  and from this point on the induction decreases continuously toward the tip.

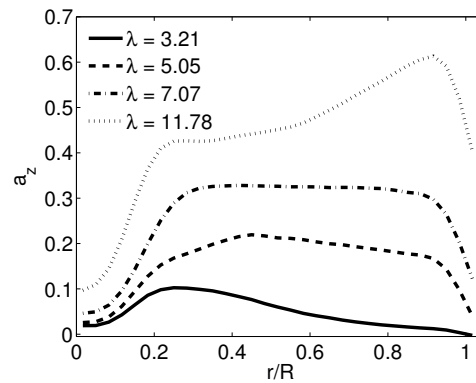


Figure 4.2: Radial distribution of the axial interference factor along the blades for each inflow velocity.

The distributions of circulation,  $\Gamma = L/(\rho V_{rel})$ , along the blades are depicted in Figure 4.3. As seen the bound circulation is nearly constant over most of the blade at  $\lambda = 7.07$  and varies only slightly at the highest tip speed ratio. At  $\lambda = 5.05$  the distribution is seen to be smoother near the tip and root, though similarly to the two higher loaded rotors the bound circulation drops somewhat abruptly in both ends of the blade. The large gradients in bound circulation near the tip and root indicates that in these situations the turbine generates a wake consisting of rather strong concentrated tip and root vortices. Furthermore the shown distributions imply that the wake in these inflow conditions presumably is characterized by only containing very little trailed vorticity.

For the lowest tip speed ratio the bound circulation is seen to vary continuously along the blade, thereby indicating that a large amount of vorticity is trailed into the wake from the entire span of the blade. Moreover, the distribution shows that for  $\lambda = 3.21$  the generated tip vortex supposedly is fairly weak and that the strongest vortices are formed near the root.

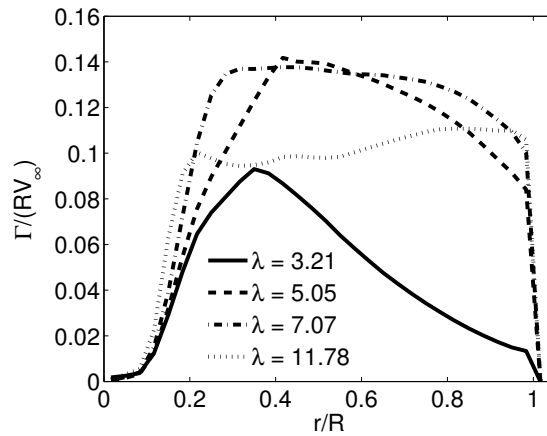


Figure 4.3: Radial distribution of circulation along the blades for each inflow velocity.

## 4.4 Wake flow characteristics

Figure 4.4 show contours of the instantaneous absolute vorticity in the vertical plane through the wind turbine center axis ( $x/R = 0$ ) for each of the tested cases. Regions of high vorticity appear as light colors. Note that the rotor is located to the left in the plots and that only the downstream development of the wake is shown.

For all cases except at  $\lambda = 3.21$ , the bound vorticity of the blades is primarily shed downstream from the tip and root of the rotor, which is consistent with the distributions of bound circulation shown in Figure 4.3. Moreover, the smoother distributions of the bound vorticity near the root at  $\lambda = 5.05$  apparently cause the hub vortices to have a somewhat larger radial extent than at the two higher tip speed ratios. As expected the wake of the rotor operating at  $\lambda = 3.21$  differs quite significantly from the other situations by having vorticity distributed over the entire radial extent of the wake.

For the three lowest tip speed ratios the bound vorticity is observed to be shed off in individual vortex tubes, whereas this does not seem to be the case at  $\lambda = 11.78$ . A closer inspection of the vorticity contours at  $\lambda = 5.05$  and  $7.07$  revealed that the distinct tip-vortex pattern is preserved



about 10 rotor radii and 1.3 rotor radii downstream respectively, where after they smear into a continuous vorticity sheet. At  $\lambda = 3.21$ , on the other hand, the vortex pattern remain distinct in the entire equidistant region, due to the high pitch of the vortex system. For the rotor oper-

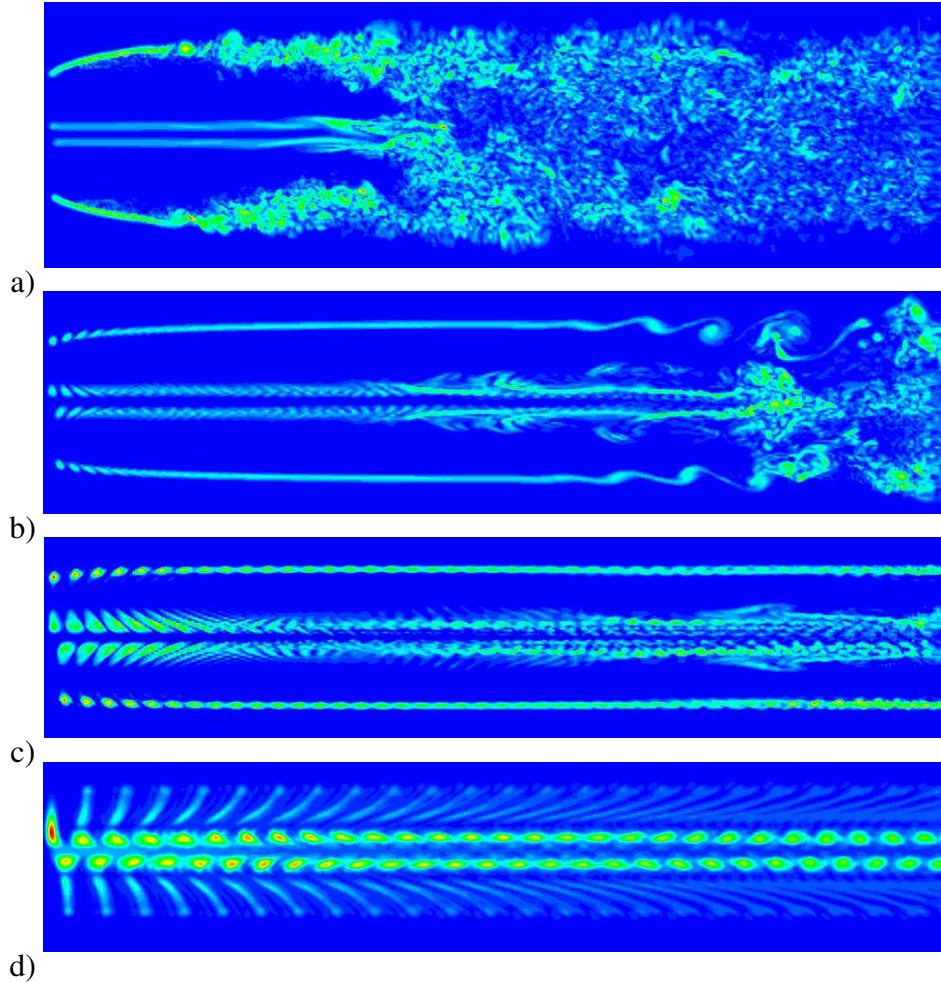


*Figure 4.4: Downstream development of the wake visualized using vorticity contours. The rotor is located to the left; a)  $\lambda = 11.78$  ( $V_\infty = 6$  m/s); b)  $\lambda = 7.07$  ( $V_\infty = 10$  m/s); c)  $\lambda = 5.05$  ( $V_\infty = 14$  m/s); d)  $\lambda = 3.21$  ( $V_\infty = 22$  m/s)*

ating at the highest tip-speed ratio instability of the tip vortices is observed to appear only 1.5 rotor radii downstream and after 5 rotor radii the wake completely breaks up. In the case where  $\lambda = 7.07$  the tip vortices are observed to undergo a Kelvin Helmholtz instability approximately 10 rotor radii downstream. The root vortices become unstable at an earlier point (about 6 rotor radii downstream of the rotor) due to their proximity and further downstream the root and tip vortices interact, which causes the wake to become fully turbulent.

In contrast to the two other cases, instability of the tip vortices does apparently not occur at  $\lambda = 5.05$  and  $\lambda = 3.21$  due to the generally higher stability of the tip vortices, when the tip-speed ratio and thus also the thrust is low.

The full three-dimensional behavior of the flow field around and downstream of the rotor is visualized in terms of iso-surface plots of vorticity in figure 4.5. The iso-surface plot show that the wake at  $\lambda = 3.21$  has a clear and stable screw surface geometry due to the large amount of trailed vorticity from the blades. For  $\lambda = 5.05$  and 7.07 the visualization give a good impres-

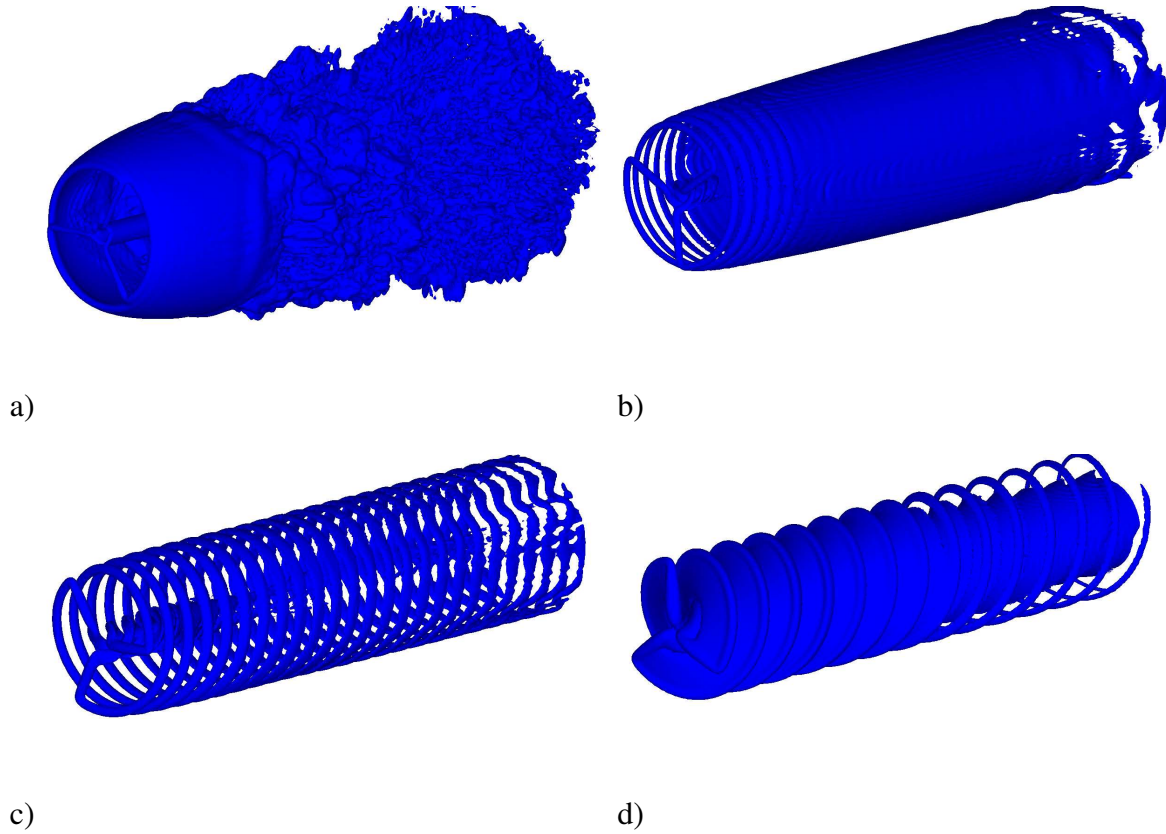


Figure 4.5: Visualization of the downstream development of the wake using iso-surface plots of vorticity; a)  $\lambda = 11.78$ ; b)  $\lambda = 7.07$ ; c)  $\lambda = 5.05$ ; d)  $\lambda = 3.21$

sion of the helical structure of the distinct tip vortices and in the latter case the transition into a continuous vortex sheet. At  $\lambda = 11.78$  the plot clearly illustrates the complete break down of the tip vortices into small scale turbulence, which as described above takes place only few rotor radii downstream.

Figure 4.6 show the development of the axial velocity distribution in the wake for each of the tested operational condition as indicated in the figure. The distributions are averaged both in time and in the circumferential direction.

Close to the rotor, the axial velocity correlates directly with the load distribution of the rotor and, due to turbulent mixing, also with the pressure field just behind the rotor.

The deficit develops at a rate depending on the loading on the rotor. For the heaviest loaded rotor wake expansion is significant and the strong break down of the tip vortices results in a rapid transition into a fully turbulent wake. As a consequence the deficit develops quickly to become nearly Gaussian approximately 7 rotor radii downstream of the rotor after which the wake deficit apparently can be assumed self-similar.

For the rotor operating at  $\lambda = 7.07$  the wake is observed to expand moderately until approximately 6 rotor radii downstream where the deficit reaches a maximum, which in agreement with BEM, is around twice the induced velocity in the rotor plane. This result is further in good agreement with laminar actuator disc computations presented by Mikkelsen [56]. From this point on the radius of the wake stays nearly constant until around 10 rotor radii after which turbulent mixing causes the distribution to develop toward a more Gaussian like shape.

For the two lightest loaded rotors the wake hardly develops and reaches equilibrium where the

axial induction again takes values approximately twice those on the rotor. Thus, in this case the boundary between the interior and the exterior of the wake stays well defined by the tip vorticity sheet for all downstream positions.

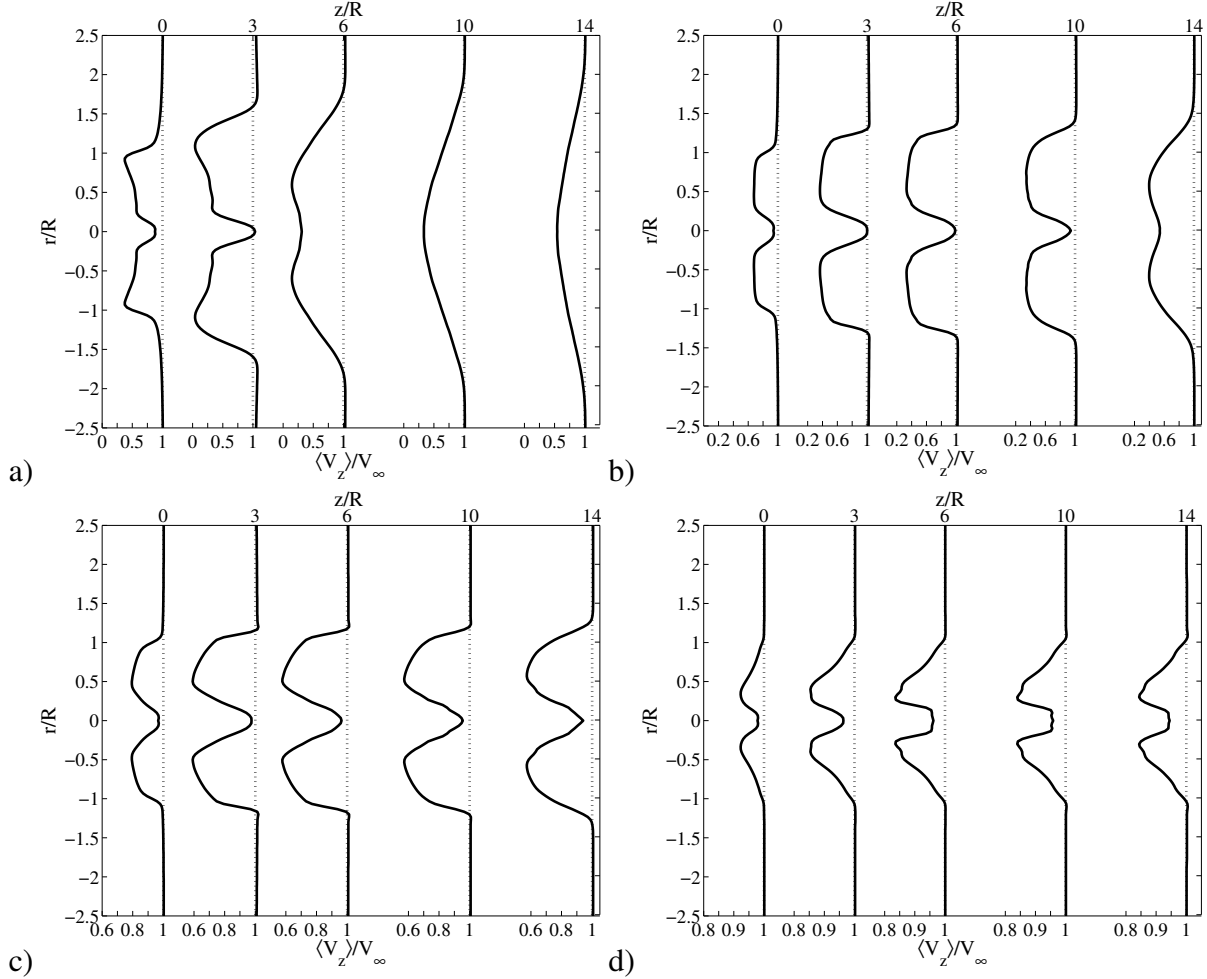


Figure 4.6: Computed profiles of the time and circumferentially averaged axial velocity at different downstream positions; a)  $\lambda = 11.78$ ; b)  $\lambda = 7.07$ ; c)  $\lambda = 5.05$ ; d)  $\lambda = 3.21$

Figure 4.7 shows the development of the velocity component in the tangential direction. Once again the shown distributions are averaged both in time and in the azimuthal direction.

The air in the wake rotates in the opposite direction to the rotor as a consequence of the reaction torque imposed upon the air by the rotor. For both  $\lambda = 5.05$  and  $7.07$  the behavior of the tangential velocity is comparable to what was observed for the axial induction factor in the sense that an equilibrium value of approximately twice the value on the rotor plane is reached though in the latter case wake rotation seems to reduce as the wake becomes unstable. Again the reached equilibrium value is in good agreement with the simple BEM methods. The plot of the development of the tangential velocity at  $\lambda = 11.78$  reveal some wake rotation within the first 3 rotor radii downstream but further downstream strong separation of the flow causes the tangential velocity to gradually diminish.

Figure 4.7 also indirectly reveal the downstream development of the averaged circulation distribution, which is computed by multiplying with  $2\pi$ , i.e. as  $\Gamma = 2\pi r V_\theta$ . It is interesting to note

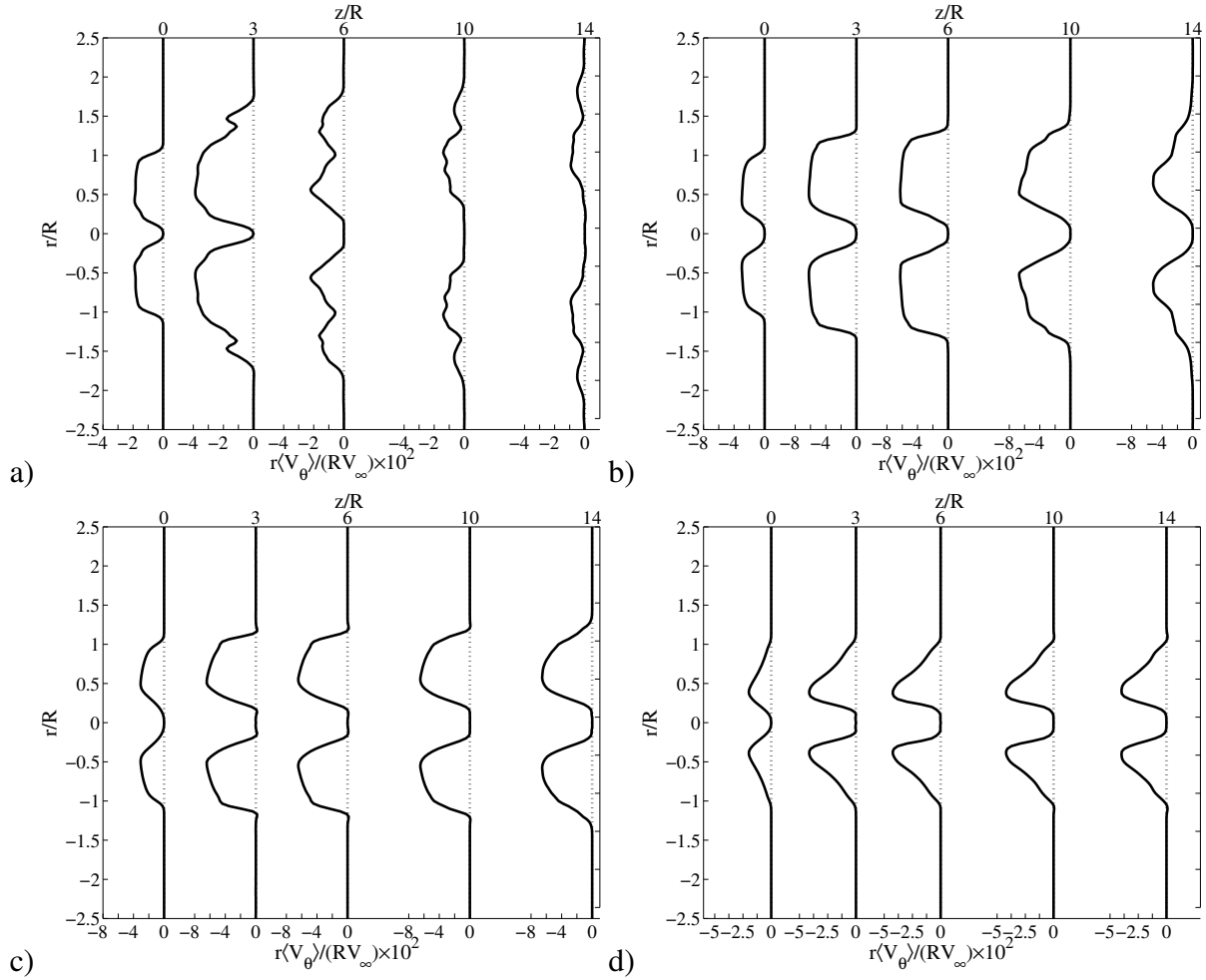


Figure 4.7: Computed profiles of the time and circumferentially averaged tangential velocity at different downstream positions; a)  $\lambda = 11.78$ ; b)  $\lambda = 7.07$ ; c)  $\lambda = 5.05$ ; d)  $\lambda = 3.21$

that the maximum circulation in the wake is approximately 3 times that of the bound circulation along one blade indicating that, in agreement with the Helmholtz theorem for vortex filaments in inviscid flows, the circulation is fairly conserved. However, it is observed that as viscous phenomena take place the theorem is generally not fulfilled. The conservation of circulation in the wake is investigated in more details in the next chapter.

## 4.5 Summary

The wake of the Tjæreborg wind turbine operating in uniform inflow at four different tip speed ratios was simulated and the initial results presented. The computations were carried out in numerical mesh, which ensured a high resolution of the region from the turbine and 7 rotor diameters downstream. For the rotor operating at  $\lambda = 11.78$  the tip vortex system was shown to completely break down around 5 rotor radii downstream and as a consequence the wake underwent a rapid transition into what could be considered a far wake, i.e. the axial velocity profiles followed closely a Gaussian shape and the tangential velocities were nearly zero.

When the rotor operated at  $\lambda = 7.07$  the tip and root vortices were shown to become unstable approximately 10 and 6 rotor radii downstream of the rotor respectively. These instabilities were observed to grow until they merged approximately 12 rotor radii downstream of the rotor, where after the wake started to become fully turbulent.

The wake of the two lightest loaded rotors was predicted to remain stable throughout the entire downstream domain. In these cases wake expansion was negligible and the general wake characteristics was observed to undergo very little development. Hence, in these two cases a larger domain is required to predict how the transition from a near wake to a far wake takes place.

Besides providing new insight into the overall development of the wake the computations also revealed other important features such as a fairly conserved circulation.

## Chapter 5

# Wind Turbine Wake Aerodynamics in Uniform Inflow - Vortex Properties

The tip and root vortex properties in the wake of the Tjæreborg wind turbine operating in uniform inflow is studied using the same computational data as presented in chapter 4. The objective is to contribute to the overall understanding of the influence of the vortices on the wake and in this connection also validate some of the common assumptions made in methods aiming at modeling the wake using respectively momentum and vortex theory. Moreover, some limitations of studying the vortex properties with the used grid resolution will be discussed.

### 5.1 Classical wake models

One of the most fundamental theories in the study of wind turbine performance is perhaps the one-dimensional momentum theory, as formulated by Froude [25]. In this theory the rotor is modeled as a frictionless uniformly loaded actuator disc in axisymmetric steady incompressible flow. By considering a balance of axial momentum and kinetic energy in a stream tube enclosing the actuator disc, it can be shown that the velocity in the rotor plane,  $V_d$  equals the average of the velocity far upstream,  $V_\infty$ , and far downstream  $V_w$ . This result is normally written in non-dimensional form as

$$V_d = (1 - a_z)V_\infty, \quad V_w = (1 - 2a_z)V_\infty \quad (5.1)$$

where  $a_z = 1 - V_d/V_\infty$  is the axial interference factor and represents the induced velocity in the rotor plane.

Besides the above fundamental result the one-dimensional momentum theory also yields the following simple expression relating the thrust coefficient of the disk to the axial induction factor

$$C_T = 4a_z(1 - a_z) \Rightarrow a_z = \frac{1}{2} \left( 1 - \sqrt{1 - C_T} \right), \quad C_T < 1 \quad (5.2)$$

Combining conservation of mass with equation 5.1 and 5.2 the wake radius,  $R_w$ , after the initial expansion can be expressed in terms of  $C_T$  as follows

$$R_w = R \sqrt{\frac{1 - a_z}{1 - 2a_z}} = R \sqrt{\frac{1 + \sqrt{1 - C_T}}{2\sqrt{1 - C_T}}}, \quad C_T < 1 \quad (5.3)$$

Hence, if the thrust coefficient is known equation 5.3 can be used to determine the far wake radius, which again can be considered an estimate of the radial position of the tip vortices. It should be appreciated, however, that methods based on the one dimensional momentum theory only is valid for  $a_z$  less than about 0.3, which can readily be seen from equation 5.1 where a negative velocity in the wake is predicted for  $a_z$  greater than 0.5. In practice a correction is normally applied for  $a_z$  greater than 0.2 [30].

Another set of classical methods are the inviscid vortex wake models, in which the shed vorticity in the wake is employed to compute the induced velocity field.

The simplest vortex models consider a rotor with an infinite number of blades with the wake described by vortex rings. Such model was e.g. developed by Øye [94], in which an iterative procedure was used to compute the relation between the induced velocities in the wake and the thrust on the disk.

Also analytical vortex wake models has been proposed where the far wake is assumed to consist of  $N$  infinitely long helical tip vortices of circulation,  $\Gamma$ , with constant radius,  $a$ , and helical pitch,  $h = 2\pi l$ , as well as a single concentrated axial hub vortex of circulation  $-N\Gamma$  in order to conserve circulation. The axial and tangential velocity induced by the  $N$  helical tip vortices may be determined analytically by the following expression, derived by Okulov [60]

$$V_{z,tip}(r, \chi) \cong \frac{\Gamma N}{2\pi l} \begin{pmatrix} 1 \\ 0 \end{pmatrix} + \frac{\Gamma}{2\pi l} \frac{\sqrt{l^2 + a^2}}{\sqrt{l^2 + r^2}} Re \sum_{n=1}^N \left[ \frac{\{\pm\} e^{i(\chi - 2\pi n/N)}}{e^{\{\mp\}\xi i} - e^{i(\chi - 2\pi n/N)}} \right] - \frac{l}{24} \left( \frac{3r^2 - 2l^2}{(l^2 + r^2)^{3/2}} + \frac{9a^2 + 2l^2}{(l^2 + a^2)^{3/2}} \right) \ln \left( 1 - e^{\{\pm\}\xi + i(\chi - 2\pi n/N)} \right) \quad (5.4)$$

$$V_{\theta,tip}(r, \chi) = \frac{\Gamma N}{2\pi r} - \frac{l}{r} V_{z,tip}(r, \chi) \quad (5.5)$$

Here, the terms in braces are defined such that the upper one corresponds to  $r < a$ , and the lower one corresponds to  $r > a$ , while  $r$  and  $\chi = \theta \pm z/l$  are the helical variables and

$$e^\xi = \frac{r \sqrt{l^2 + a^2} + l}{a \sqrt{l^2 + r^2} + l} \left( \frac{\exp(\sqrt{l^2 + r^2})}{\exp(\sqrt{l^2 + a^2})} \right)^{1/l} \quad (5.6)$$

If equation 5.4 is averaged in the circumferential direction all terms except the first vanish hence predicting a constant axial induction inside the wake. Accordingly equation 5.5 reveals that the circumferentially averaged induced tangential velocity will be inversely proportional to the radial position.

If the root vortex as mentioned above is assumed to lie along the system axis it only contributes to the tangential induction. In this case the tangential velocity induced by the complete  $(N + 1)$  vortex system becomes

$$V_\theta(r, \chi) = \frac{\Gamma N}{2\pi r} - \frac{l}{r} V_{z,tip}(r, \chi) + \frac{\Gamma_0}{2\pi r} \quad (5.7)$$

Here, the circulation of the root vortex would normally be set to  $\Gamma_0 = -N\Gamma$  in order to conserve circulation as mentioned above.

Equation 5.5 directly shows that, for vorticity fields with helical symmetry, the velocity tangential to the helical lines remains constant i.e. [60]

$$V_z \pm \frac{r}{l} V_\theta = \pm const \quad (5.8)$$

## 5.2 Vortex positions and pitch

The positions of the tip and root vortex centers can be identified directly from the vorticity contours presented in figure 4.4 as the location of highest local vorticity.

It should be noted that, with the current resolution of the wake, the center of the tip vortices could only be identified up to about 1.3 rotor radii downstream of the rotor at  $\lambda = 7.07$ , while at  $\lambda = 11.78$  it was not possible at all to identify distinct local extremes from the contours. Therefore, in these situations the actual downstream location of the vortex centers could not be extracted. However, their radial position was in these cases taken as the centre of the vorticity sheet at selected downstream positions. It should further be emphasized that using the absolute value of the vorticity as a means of identifying vortex cores is limited by its strong dependence on the chosen contour levels and especially far from the rotor the method is accompanied with some uncertainties.

Figure 5.1 shows the radial location of the tip vortex centers as a function of their downstream position. The horizontal dotted lines also shown in the figure indicate the far wake radius computed from equation 5.3, i.e. the predictions of 1D momentum theory for a uniformly loaded disk with the same thrust coefficient as determined from the corresponding actuator line computations (shown in table 5.1). Note, that the classical 1D momentum theory cannot be applied for the case  $\lambda = 11.78$ , where  $C_T = 1.16$  since this value clearly is outside the theory's bounds of application. For this reason the predictions of the 1D momentum theory is only shown for thrust coefficients corresponding to those of the three lightest loaded rotors.

$\lambda(V_\infty)$	3.21(22 m/s)	5.05(14 m/s)	7.07(10 m/s)	11.78(6 m/s)
$C_T$	0.14	0.56	0.85	1.16

Table 5.1: Predicted thrust coefficient as a function of tip speed ratio

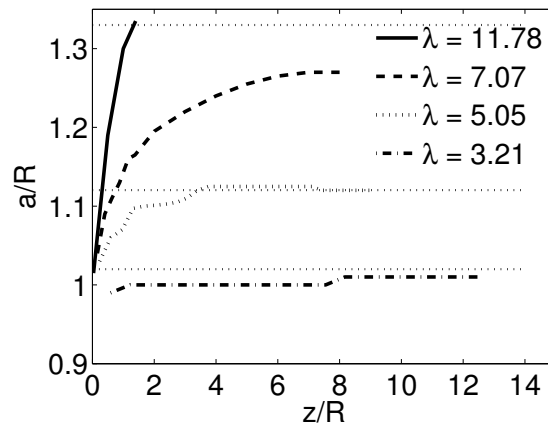


Figure 5.1: Radial location of the tip vortices as a function of downstream position. The horizontal dotted lines indicate the corresponding predictions by 1D momentum theory (equation 5.3) in the cases (from top to bottom)  $\lambda = 7.07$ ,  $\lambda = 5.05$  and  $\lambda = 3.21$

For the two lowest tip speed ratios, where the expansion of the wake is also lowest, the agreement between 1D momentum theory and the actuator line method is good. The observed differ-



ences might very well be due to uncertainties in the determination of the vortex core positions. On the other hand, at  $\lambda = 7.07$  where the thrust coefficient is  $C_T = 0.85$ , 1D momentum theory is observed to over-estimate the wake expansion compared to that predicted by the actuator line computations. Figure 5.2 shows the downstream position of respectively the tip and root vortex

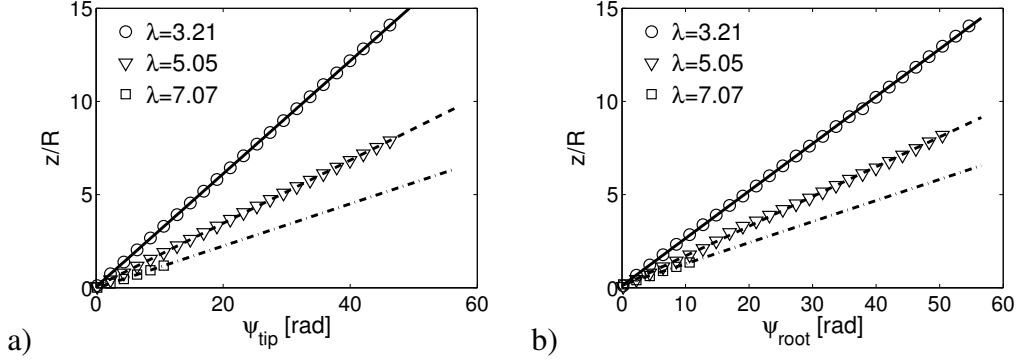


Figure 5.2: Angular positions of tip (a) and root (b) vortex cores as a function of their downstream location determined from contour plots of vorticity

cores as a function of their angular location,  $\psi$  (wake age). Because of the above mentioned difficulties in identifying distinct extremes from the contours this procedure could not be applied for the case  $\lambda = 11.78$ . Note that the results have been obtained by phase-lock ensemble averaging over a number of rotor revolutions. From figure 5.2 the helical pitch of the vortices can be estimated as

$$h = 2\pi \frac{\partial z}{\partial \psi} \quad (5.9)$$

As seen the results are well estimated with straight lines and thus, the root and tip vortex pitch in all cases appears to be approximately constant. The latter result is consistent with the experimental results presented by Ebert and Wood [18] and by Grant and Parkin [28].

By determining the slope of the fitted lines the tip vortex pitch was found to be approximately 1.90, 1.06 and 0.7 for respectively  $\lambda = 3.21$ , 5.05 and 7.07, while the corresponding root vortex pitch was found to be respectively 1.6, 1.0 and 0.7.

The estimated tip and root vortex pitch values are plotted against the tip speed ratio in figure 5.3 and are compared with the values in the case of zero induction i.e. where the vortices are traveling at free stream velocity.

The figure shows an overall trend of decreasing pitch with increasing tip speed ratio as expected. The nearly uniform loading of the rotor at  $\lambda = 5.05$  and 7.07 causes the tip and root vortex pitch to be nearly equal in these cases. On the other hand the difference between the root and tip vortex pitch is rather large at  $\lambda = 3.21$  where the rotor is non-uniformly loaded. Furthermore, as a consequence of the very low induction near the tip at  $\lambda = 3.21$  the tip vortex pitch is close to the zero induction curve.

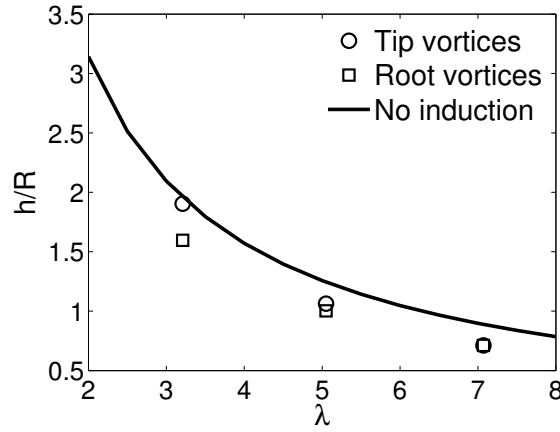


Figure 5.3: Pitch of respectively tip- and root vortices as a function of tip speed ratio

As described above the relation given in equation 5.10 is valid for flows with helical symmetry and therefore can be used to evaluate the radial distribution of the pitch of the vortex system in the wake, i.e.

$$l = \frac{rV_\theta}{const - V_z} \Leftrightarrow h = 2\pi \frac{rV_\theta}{const - V_z} \quad (5.10)$$

The constant appearing in the above expression is evaluated at the centre axis ( $r = 0$ ), where it according to equation 5.8 equals the axial velocity, i.e.  $const = V_z(r = 0)$ .

Figure 5.4 presents the computed distributions of the pitch for various downstream positions in the wake. At  $\lambda = 3.21$ , results are only shown for the inner part of the wake because the denominator in equation 5.10 becomes very small in the region  $r/R = 0.8 - 1$ . The computed pitch at  $\lambda = 3.21$  undergoes large variations indicating that in this case the vorticity field formed behind the turbine is not well modeled by assuming helical symmetry. The same can be concluded for the case  $\lambda = 11.78$ . On the other hand, at  $\lambda = 5.05$  and  $7.07$  the computed profiles of the pitch (at least for radial positions between the root and tip vortices) attains fairly constant values of about respectively 1.02 and 0.63. Even though the values differs somewhat from those estimated directly from the contours the constant profiles indicate that at least a large part of the wake can be considered helical symmetric.

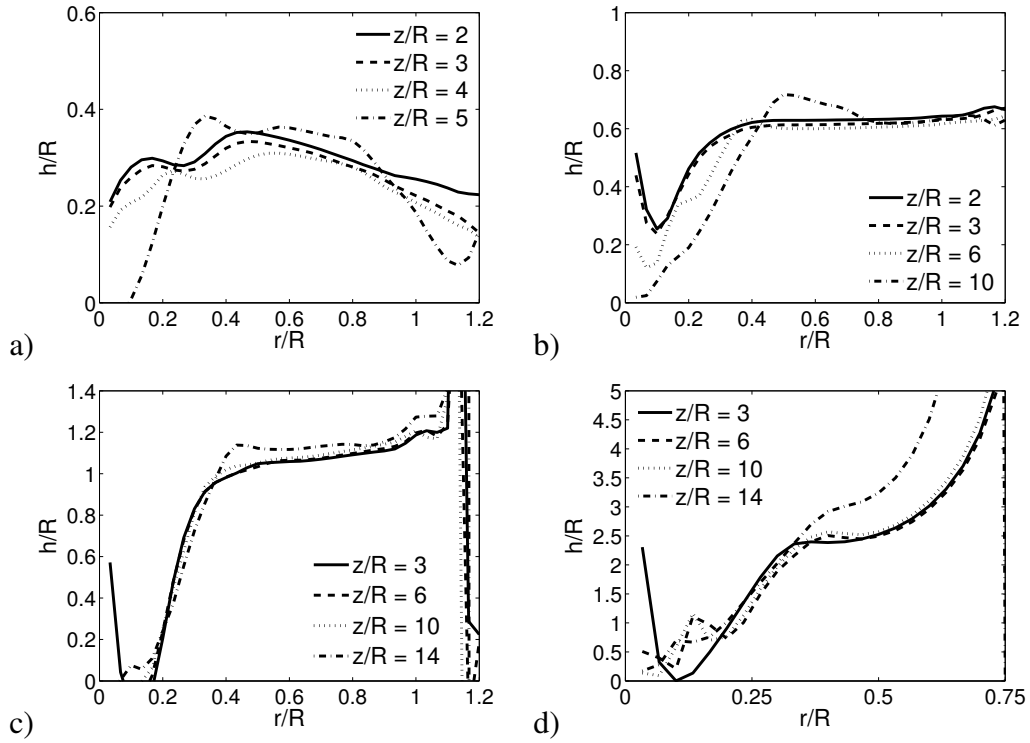


Figure 5.4: Radial distribution of pitch computed from equation 5.10 for various downstream positions. a)  $\lambda = 11.78$ ; b)  $\lambda = 7.07$ ; c)  $\lambda = 5.05$ ; d)  $\lambda = 3.21$

### 5.3 Circulation

Figure 5.5 shows the downstream development of the circumferentially and time averaged circulation distribution computed as  $\Gamma = 2\pi r \langle V_\theta \rangle$ . Also shown in the plot is,  $N\Gamma_{bound}$ , the profile of the bound circulation along the blades (as shown in figure 4.3) multiplied with the number of blades. Thereby, the plot directly reveals if the circulation in the wake is conserved as stated by the Helmholtz theorem for vortex filament in inviscid flows.

As seen at  $\lambda = 3.21$  and  $5.05$  circulation is generally well conserved throughout all the investigated downstream positions.

As revealed from the maximum of the circulation profiles, circulation is also fairly well conserved at  $\lambda = 7.07$  but only until approximately 12 rotor radii downstream, where after the breakdown of the vortex system causes the circulation to decrease. In the latter case the circulation is furthermore observed to undergo considerably redistribution with downstream position. However, the distribution of circulation is in this case still rather uniform 6 rotor radii downstream of the rotor, hence indicating stable tip vortices at this position. Even though the circulation profiles are not as uniform at  $\lambda = 5.05$ , the sharp drops observed in the inner and outer part of the wake indicates strong tip and root vortices in agreement with figure 4.4. A uniform circulation distribution furthermore, directly reveal that the tangential velocity varies approximately inversely proportional to the radial positions which is in agreement with equation 5.5. For  $\lambda = 11.78$ , the circulation is far from being conserved even close to the rotor but in this case the flow conditions is also dominated strongly by viscous phenomena.

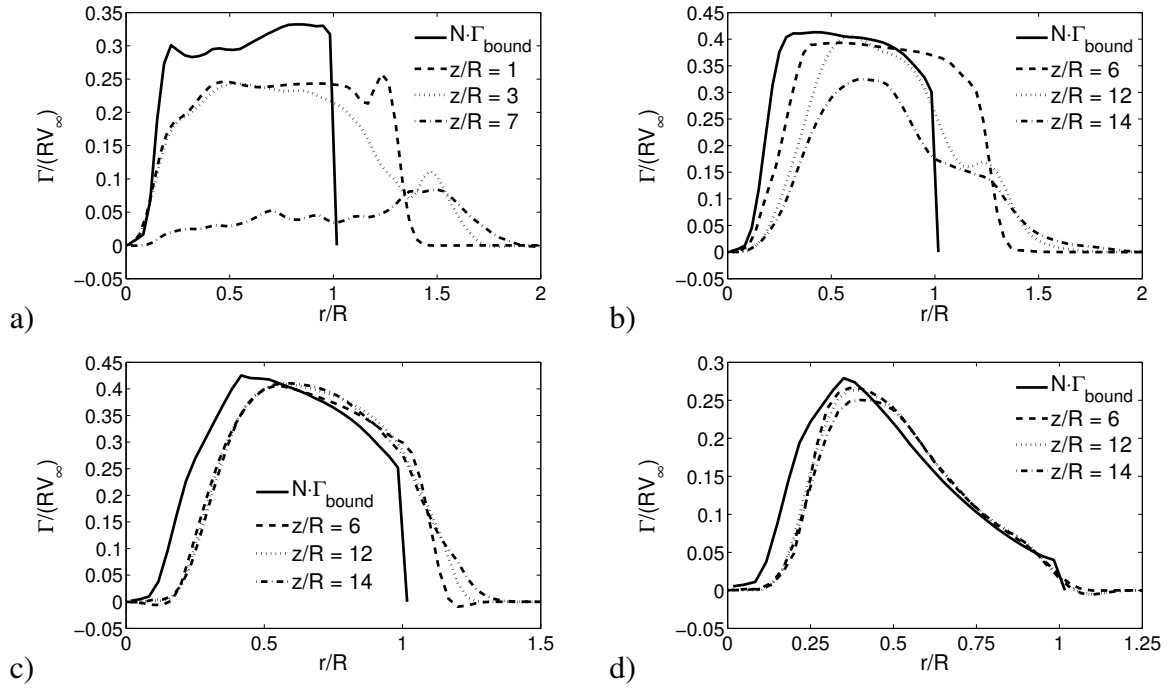


Figure 5.5: Profiles of time and circumferentially averaged circulation at different downstream positions in the wake compared to the bound circulation of the blades. a)  $\lambda = 11.78$ ; b)  $\lambda = 7.07$ ; c)  $\lambda = 5.05$ ; d)  $\lambda = 3.21$

## 5.4 Induced velocities

Figure 5.6-5.8 show the axial velocity component as a function of rotor azimuth angle at different radial and downstream positions for the three lowest tip speed ratios. The corresponding figures at  $\lambda = 11.78$  are not shown here because the induced velocities in this case do not vary in the circumferential direction since the grid resolution, as mentioned above, was insufficient to capture the distinct nature of the tip vortices.

In all the shown cases there are three distinct peaks associated with the passage of the vortices. At  $\lambda = 3.21$  these peaks remain clear for all tested downstream sections and the vortex passage is felt throughout the entire radial extent of the wake due to the strong hub vortex and the large amount of vorticity shed from the blades. Moreover, the figure shows that the peaks associated with the various radial positions are out of phase due to the non-uniform loading.

For the two shown sections downstream of the rotor operating at  $\lambda = 5.05$  the influence of the distinct vortex system is visible for nearly all radial positions though they are most clear near the tip vortices. As expected, there is a phase shift of about  $90^\circ$  between the curves obtained at radial positions inside and outside the location of the tip vortices due to the change of sign of the induction.

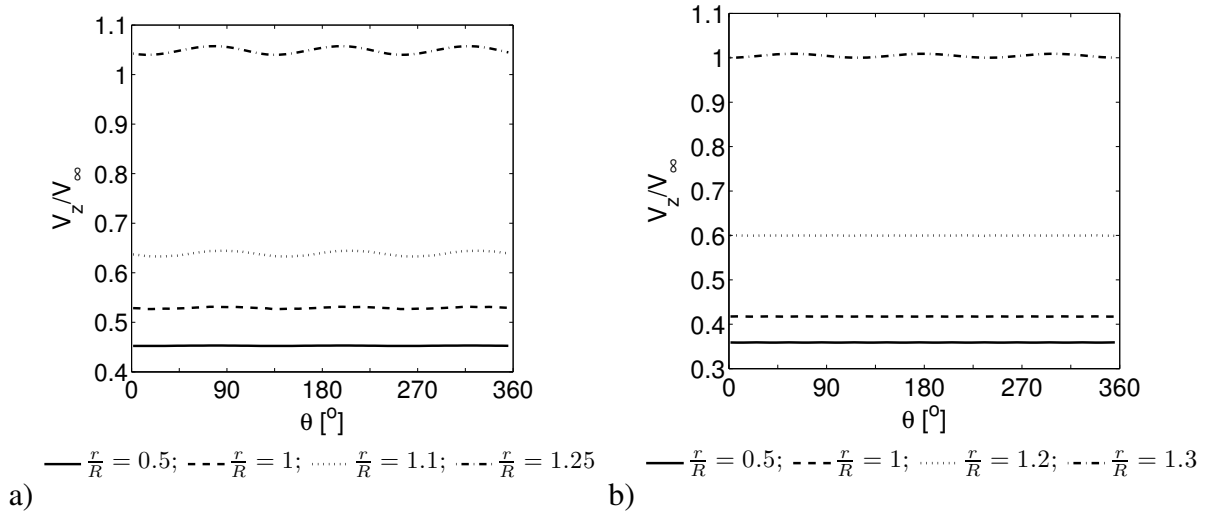


Figure 5.6: Axial velocities as a function of azimuth angle downstream of the rotor at  $\lambda = 7.07$ .  
a)  $z/R = 1$ ; b)  $z/R = 3$ .

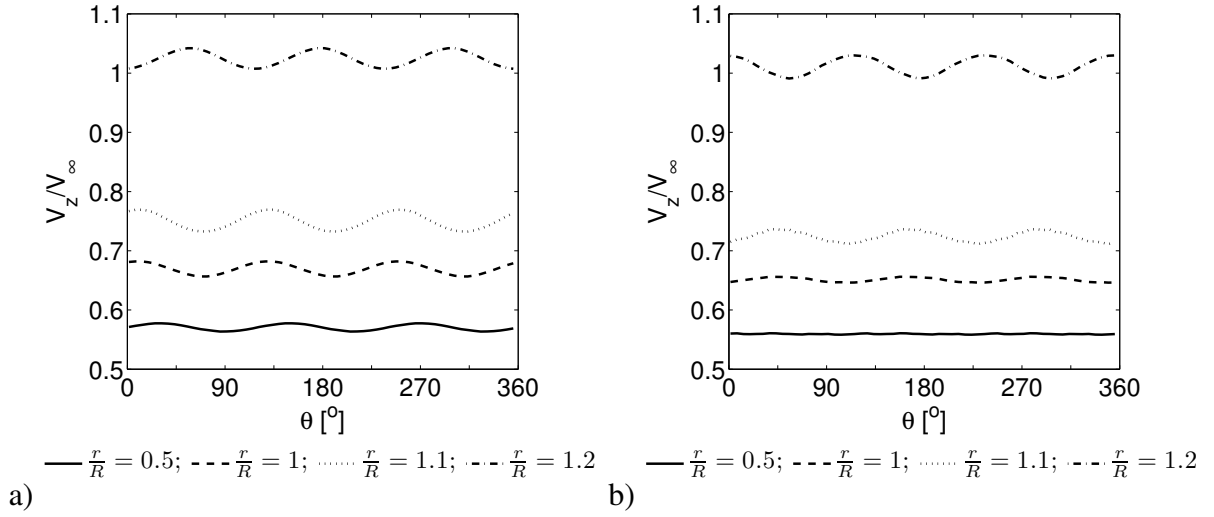


Figure 5.7: Axial velocities as a function of azimuth angle downstream of the rotor at  $\lambda = 5.05$ .  
a)  $z/R = 3$ ; b)  $z/R = 6$ .

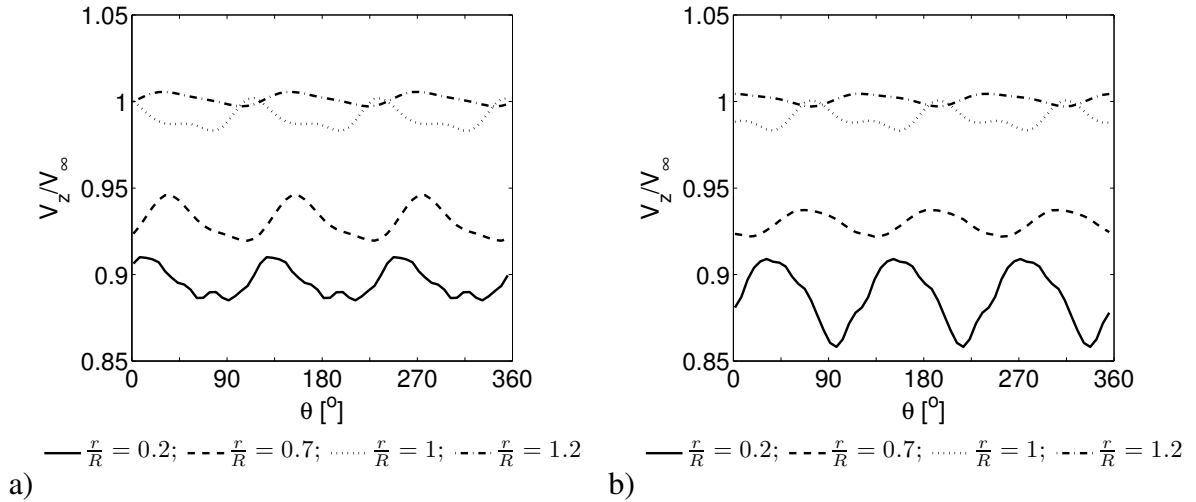


Figure 5.8: Axial velocities as a function of azimuth angle downstream of the rotor at  $\lambda = 3.21$ .  
a)  $z/R = 6$ ; b)  $z/R = 10$ .

At  $\lambda = 7.07$  the peaks are only visible for radial positions close to the tip vortices and tend to be rather weak as a consequence of the limited resolution. The lack of resolution also causes the peaks from the tip vortices to decay rapidly with downstream position and 3 rotor radii downstream they are only vaguely visible. However, this was expected from figure 4.4, where it was shown that the distinct tip vortices smeared into a continuous vorticity sheet about 1.3 rotor radii downstream.

In figure 5.9 and 5.10 the temporally and circumferentially averaged profiles of respectively the axial and tangential induction in a section located 6 rotor radii downstream of the rotors at respectively  $\lambda = 5.05$  and 7.07 are compared with the corresponding predictions from equation 5.4 and 5.7, with the used parameters chosen as summarized in Table 5.2.

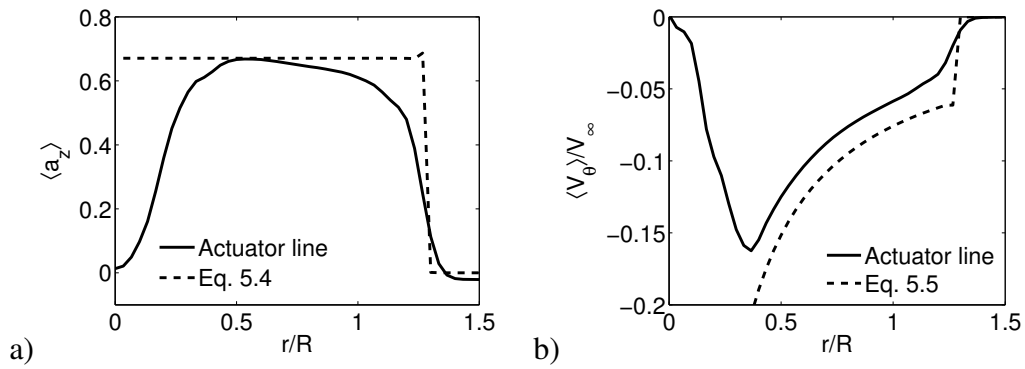


Figure 5.9: Comparison of respectively; a) the axial interference factor and; b) the tangential induction predicted from respectively the actuator line computations and equation 5.4-5.5. The distribution has been averaged both in time and in the circumferential direction. ( $\lambda = 7.07$ ,  $z/R = 6$ )

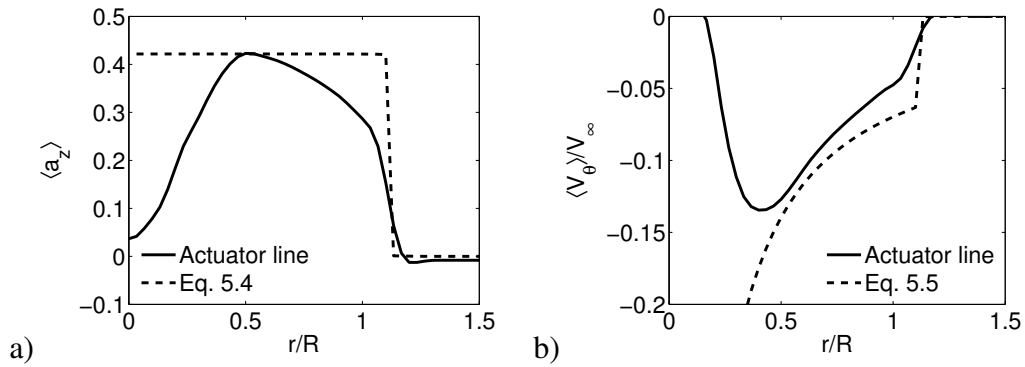


Figure 5.10: Comparison of respectively; a) the axial interference factor and; b) the tangential induction predicted from respectively the actuator line computations and equation 5.4-5.5. The distribution has been averaged both in time and in the circumferential direction. ( $\lambda = 5.05$ ,  $z/R = 6$ )

A more relevant comparison would of course have been of the predicted circumferential variation of the induced velocities since these are provided by the analytical expressions of Okulov (equation 5.4-5.5). However, due to the limited resolution in the computations a comparison of the induction near the individual vortices could not be properly carried out. Recall from chapter 4 that 6 rotor radii downstream of the rotor the wake at  $\lambda = 5.05$  and 7.07 has reached a state of equilibrium where the induced velocities are approximately twice those at the rotor plane, cor-

responding to the far wake of the one-dimensional momentum theory. The two cases  $\lambda = 3.21$  and  $11.78$  are not shown here since they obviously do not compare well with expression 5.4 and 5.5, which only include the induction of the tip vortices and a concentrated centre vortex.

$\lambda$	$a/R$	$h = 2\pi l$	$\Gamma/(RV_\infty)$
7.07	1.27	0.70	0.13
5.05	1.13	1.05	0.13

*Table 5.2: Parameters used in the comparison shown in figure 5.9 and 5.10. The values have been estimated from respectively figure 5.1, 5.4 and 5.5*

As seen there is generally a good agreement between the predictions of maximum axial induction for both of the shown cases, however, as equation 5.4 only includes the influence of the tip vortices and not the vorticity shed from the blades and the hub, this expression cannot capture the correct shape of the profiles. The influence of the shed vorticity from the blades and hub could be accounted for by adding an extra term in equation 5.4 such as proposed by Sørensen and Okulov [76], nevertheless, it is generally difficult to establish a correction, which can be used for all wake situations.

The tangential induced velocity is seen to compare less well than the axial component but at least the predictions, especially at  $\lambda = 7.07$ , agree fairly well in terms of shape in the outer part of the wake. The huge over prediction of the induced tangential velocity by expression 5.5 in the inner part of the wake is due to the unphysical assumption of the root vortex being concentrated on the centre axis, which in turn causes the tangential velocity to be inversely proportional to the radius.

## 5.5 Summary

This chapter has presented the properties of the tip and root vortices in the wake of the Tjæreborg turbine operating in a uniform inflow at various tip-speed ratios. It was shown that both the tip and root vortex pitch was constant in the wake and that it increased with decreasing tip speed ratio.

Moreover, it was found that at  $\lambda = 3.21$ ,  $5.05$  and  $7.07$  the circulation in the wake is fairly conserved. However, in the latter case circulation underwent significant redistribution and was only conserved until the vortex system started to break up. In the wake of the rotor operating at  $\lambda = 11.78$ , where the wake breaks up close to the rotor, circulation was not conserved at all. In addition, it was shown that at  $\lambda = 5.05$  and  $7.07$  most of the circulation was contained in the tip and root vortices.

Furthermore, a study of the azimuthal variation of the velocities revealed that at  $\lambda = 3.21$  the induction of the individual vortices was felt throughout all the explored downstream positions, while this individual pattern, due to limited grid resolution, was less pronounced for higher tip speed ratios.

Besides the above findings some of the results of the actuator line computations were compared with models based on classical theory.

The azimuthally averaged axial induction predicted by the analytical vortex model of Okulov [60] at  $\lambda = 5.05$  and  $7.07$  compared well with the corresponding prediction of the actuator

line simulation in terms of maximum induction but deviated somewhat in terms of shape. Furthermore, it was found that the model of Okulov captured the correct shape of the azimuthally averaged tangential induction quite accurately but that it generally was over predicted compared to the result of the actuator line computations.

Finally, it was shown that the one dimensional theory captured the wake expansion well at  $\lambda = 3.21$  and  $5.05$  but over predicted it at  $\lambda = 7.07$ .



## Chapter 6

# Wind Turbine Wake Aerodynamics in Uniform Inflow - Turbulence Properties

The basic turbulence properties in the wake of the Tjæreborg turbine operating in a uniform inflow are characterized using the same computational data as presented in chapter 4. However, the main focus here is in the cases  $\lambda = 11.78$  and  $\lambda = 7.07$  which represents the most interesting wake dynamics. The study includes calculation of Reynolds-stresses, self-similarity profiles, length-scales, spectral characteristics and coherence properties.

### 6.1 Reynolds stresses

Figure 6.1-6.4, for each tip speed ratio, presents the radial distribution of the four main components of the Reynolds-stress tensor,  $\langle v_i v_j \rangle$ , at different positions downstream of the turbine. All the shown curves are averaged in the circumferential direction. The two components  $\langle v_z v_\theta \rangle$  and  $\langle v_r v_\theta \rangle$  are zero due to circumferential symmetry [63] and hence are not shown in the figures. It should be noted that the scale of the figure axes are not the same and that the magnitude of the Reynolds-stresses generally increase with increasing tip speed ratio.

In the near wake of the rotor operating at  $\lambda = 11.78$  the Reynolds stresses has a distinct maximum in the region of the tip vortices but further downstream the Reynolds-stress distributions develop toward a bell shaped form. Comparing figure 6.1 with figure 4.6 it is evident that the generated turbulence is more persistent than the mean velocity deficit. Furthermore, it is observed that for increasing distance to the rotor, the three normal stresses approaches each other and the shear stress goes toward zero, which indicate that the wake exhibit increasing isotropy with downstream position. Both of these observations are consistent with field measurements presented in [31] and [10].

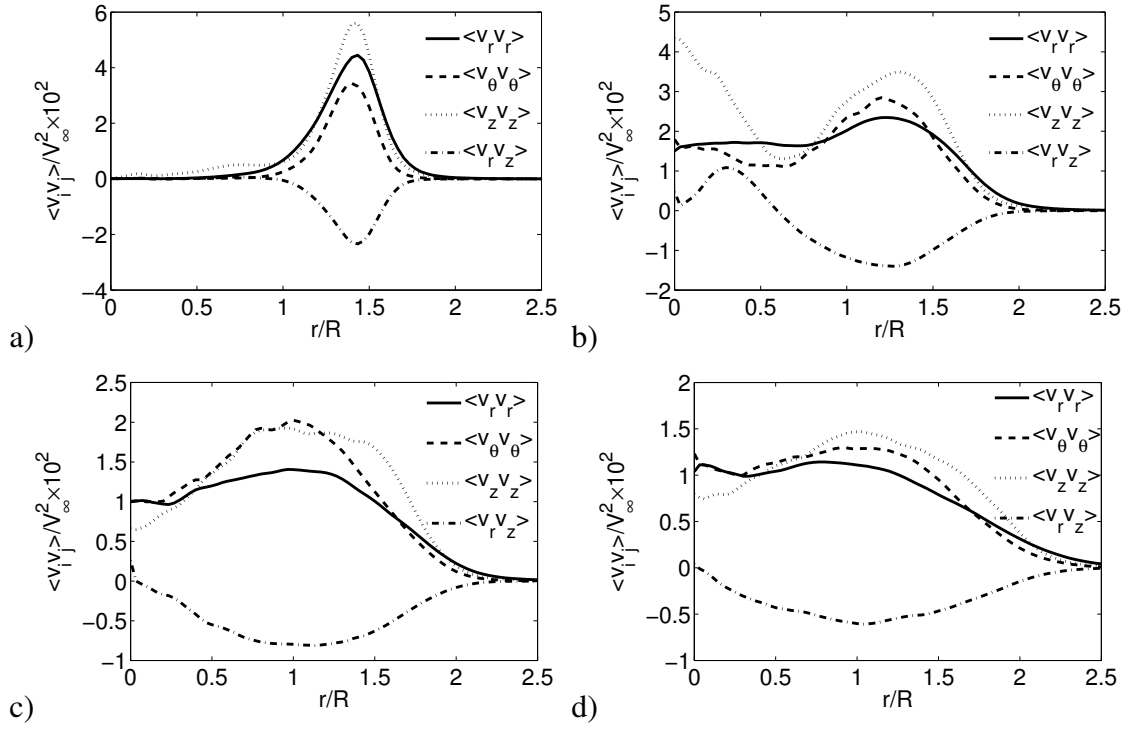


Figure 6.1: Profiles of the Reynolds-stresses at  $\lambda = 11.78$  for different downstream sections. a)  $z/R = 3$ ; b)  $z/R = 6$ ; c)  $z/R = 10$ ; d)  $z/R = 14$ .

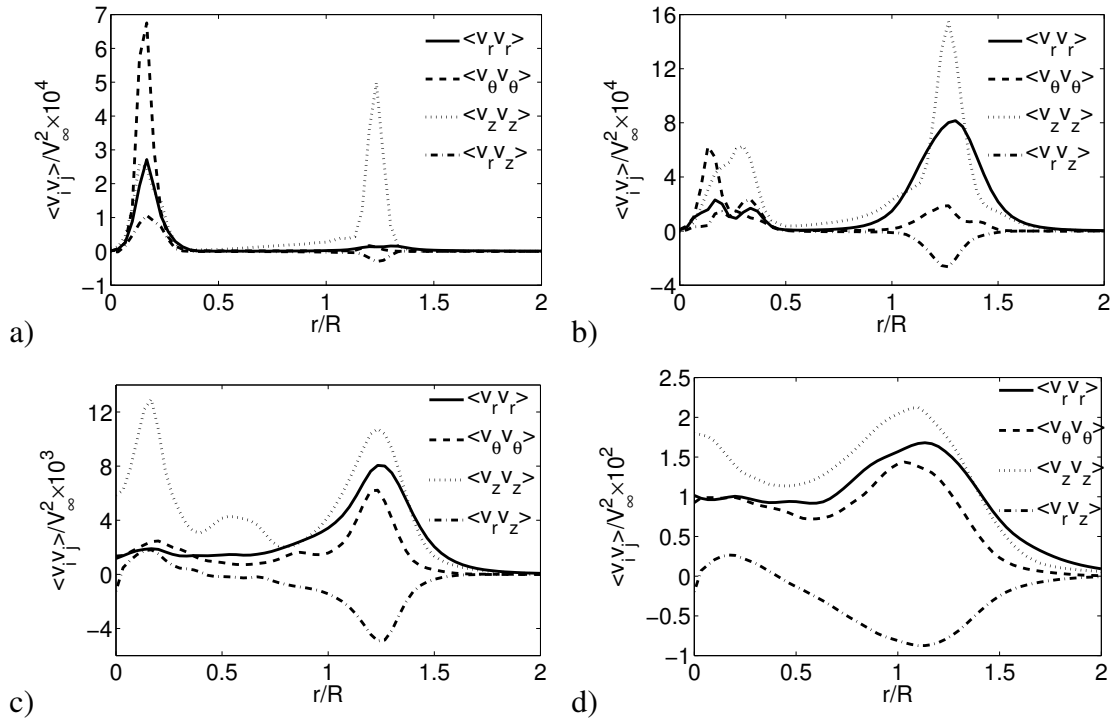


Figure 6.2: Profiles of the Reynolds-stresses at  $\lambda = 7.07$  for different downstream sections. a)  $z/R = 3$ ; b)  $z/R = 6$ ; c)  $z/R = 10$ ; d)  $z/R = 14$ .

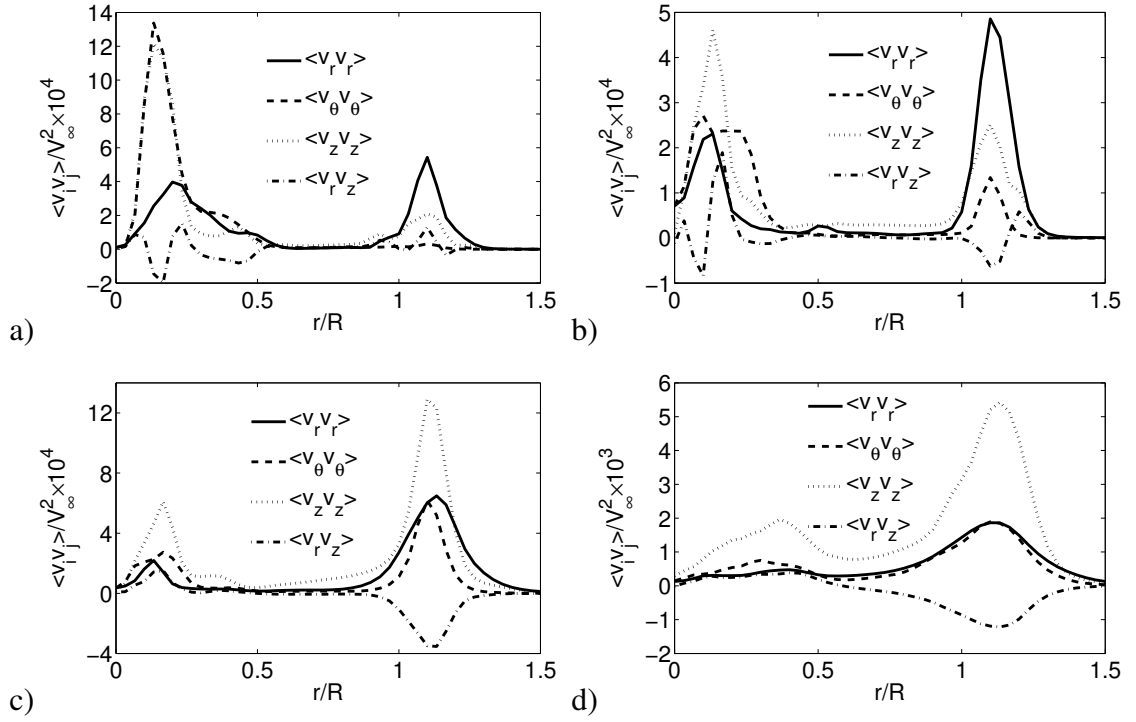


Figure 6.3: Profiles of the Reynolds-stresses at  $\lambda = 5.05$  for different downstream sections. a)  $z/R = 3$ ; b)  $z/R = 6$ ; c)  $z/R = 10$ ; d)  $z/R = 14$ .

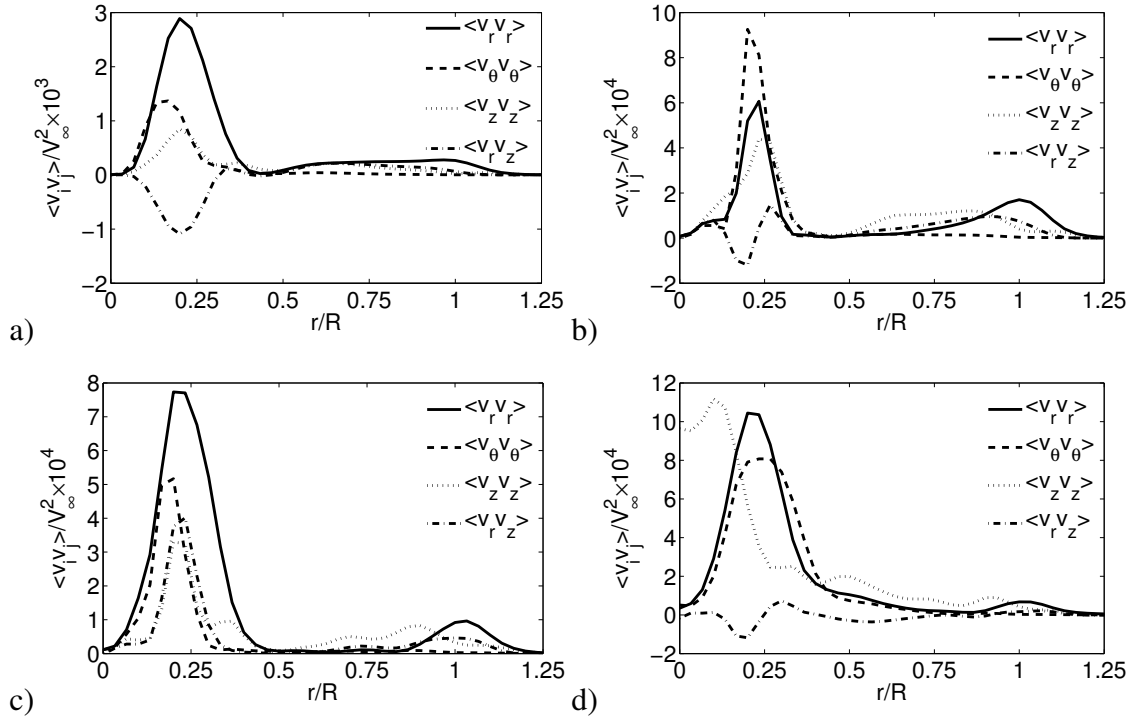


Figure 6.4: Profiles of the Reynolds-stresses at  $\lambda = 3.21$  for different downstream sections. a)  $z/R = 3$ ; b)  $z/R = 6$ ; c)  $z/R = 10$ ; d)  $z/R = 14$ .

At  $\lambda = 5.05$  and  $7.07$  the Reynolds stresses are largest in the region of the root and tip vortices, however especially in the latter case, where the vortex system breaks up (see figure 4.4), the downstream development is significant and the Reynolds stresses become more distributed over the entire radial extent of the wake.

In the final case,  $\lambda = 3.21$ , the Reynolds stresses maximizes in the inner part of the wake and only a small peak is observed due to the presence of the tip vortices. This is consistent with figure 5.5 and 4.4, showing that the wake in this case is characterized by significant shed vorticity and a dominating root vortex.

It should be noted that for  $\lambda = 3.21$  and  $5.05$  the levels of the Reynolds-stresses are generally very small and indeed, in a rotating frame of reference the wake can almost be considered steady in these two cases.

## 6.2 Self-similarity

In appendix A the concept of self-similarity is briefly described and it is noted that the axisymmetric wake actually does not become exactly self-similar but only approaches this stage asymptotically in the far wake as  $V_s/V_\infty$  tends to zero. In practice self-similarity is observed for  $V_s/V_\infty$  less than about 0.1, however, looking at figure 4.6 it is clear that this requirement is not exactly fulfilled within the range of investigated downstream positions. For this reason only self-similarity in relation to the mean velocity deficit will be tested here, since it as mentioned above develops faster than the turbulence.

In Figure 6.5 the scaled velocity profile defined by equation A.24 is shown for respectively  $\lambda = 11.78$  and  $7.07$  at different downstream sections and the result is compared to the analytical constant eddy-viscosity solution given by (see appendix A)

$$f_v(\xi) = \exp(-\alpha\xi^2) \quad (6.1)$$

where  $\alpha = \ln 2$  and  $\xi = r/r_{1/2}$ .

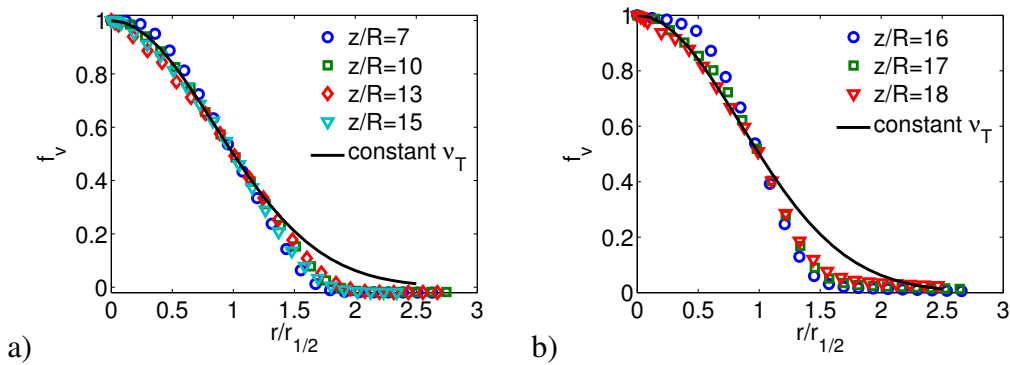


Figure 6.5: Scaled mean velocity downstream of the rotor operating at a)  $\lambda = 11.78$  and b)  $\lambda = 7.07$

As seen the wake of the rotor operating at  $\lambda = 11.78$  can be assumed self-similar in terms of the mean axial velocity after approximately 7 rotor radii since all scaled profiles after this point nearly collapse on a single curve. For  $\lambda = 7.07$  self-similarity seems a fair assumption beyond 16 rotor radii. The analytical solution and the computed results compare very well in the inner

part of the wake but differ in the outer part. The same results are typically observed in the wake of cylinders and flat plates [63].

### 6.3 Spectral characteristics

Figure 6.6 and 6.7 show the spectral characteristics of the streamwise velocity component at different radial and downstream positions for respectively  $\lambda = 11.78$  and  $\lambda = 7.07$ . All the shown spectra have been computed using spectral averaging in the circumferential direction. The corresponding spectra of the radial and tangential velocity components are not shown here since they were found to be similar to those of the axial velocity. However, these spectra will be characterized in the next section by the standard deviation  $\sigma_k$  and the characteristic Kaimal length scale  $L_k$  using the procedure outlined in appendix A.

It should be appreciated, that the rather steep drop of the shown spectra observed at high frequencies mainly is attributed to a combination of the limited spatial resolution and numerical diffusion. Finally, it is noted that the spectral estimates in the wake center ( $r/R = 0$ ) is considerably more noisy than the spectra at the other radial positions because the spectral averaging in the azimuth direction result in no averaging at  $r/R = 0$ .

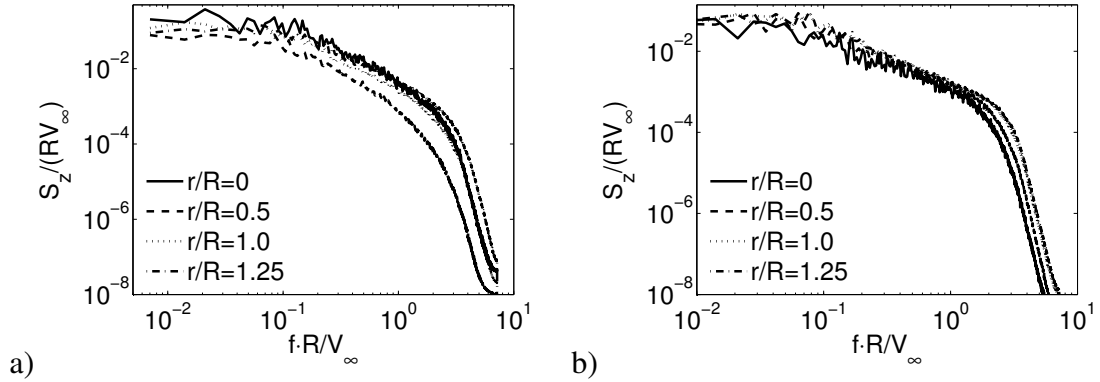


Figure 6.6: Spectral characteristics of the axial velocity component in the wake of the rotor operating at  $\lambda = 11.78$ . a)  $z/R = 6$ ; b)  $z/R = 14$ .

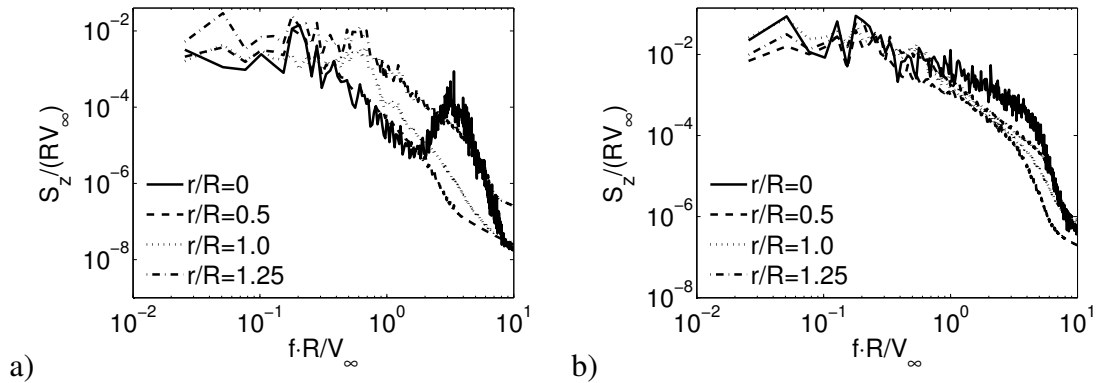


Figure 6.7: Spectral characteristics of the axial velocity component in the wake of the rotor operating at  $\lambda = 7.07$ . a)  $z/R = 10$ ; b)  $z/R = 13$ .

Comparing spectra obtained at the various tested radial positions with figure 6.1 and 6.2 it is seen that a general characteristic of the turbulence is that it has the largest energy contents in the regions with the highest gradients. At  $\lambda = 11.78$  the shown spectra furthermore indicate that the wake turbulence decays and tend to become more spatial homogeneous with downstream position. The trend toward more spatial homogeneous turbulence with downstream position is also observed at  $\lambda = 7.07$ , however in this case the energy level is increasing in agreement with figure 6.2.

At  $\lambda = 11.78$  none of the spectra show sign of organized structures at distinct frequencies, however, there is a clear region with an approximate slope of  $-5/3$ , which is characteristic for the initial sub-range.

For the rotor operating at  $\lambda = 7.07$ , the spectra obtained 13 rotor radii downstream has more or less the same characteristic shape as those found at  $\lambda = 11.78$ , whereas the spectra obtained 10 rotor radii downstream has a clear sign of a organized hub vortex in agreement with the contour plots shown in figure 4.4.

## 6.4 Characteristic length scales

In the following the characteristic length scales,  $L_{k,i}$  of the wake will be estimated at different radial and downstream positions by fitting the various computed spectra with the Kaimal spectrum as described in appendix A. The analysis is only carried out for the rotor operating at  $\lambda = 11.78$  since only in this case the wake could be considered fully turbulent for all tested positions.

Figure 6.8 shows the estimated standard deviation,  $\sigma_{k,i}$ , and the Kaimal length scale,  $L_{k,i}$  of each velocity component as a function of radial and downstream position.

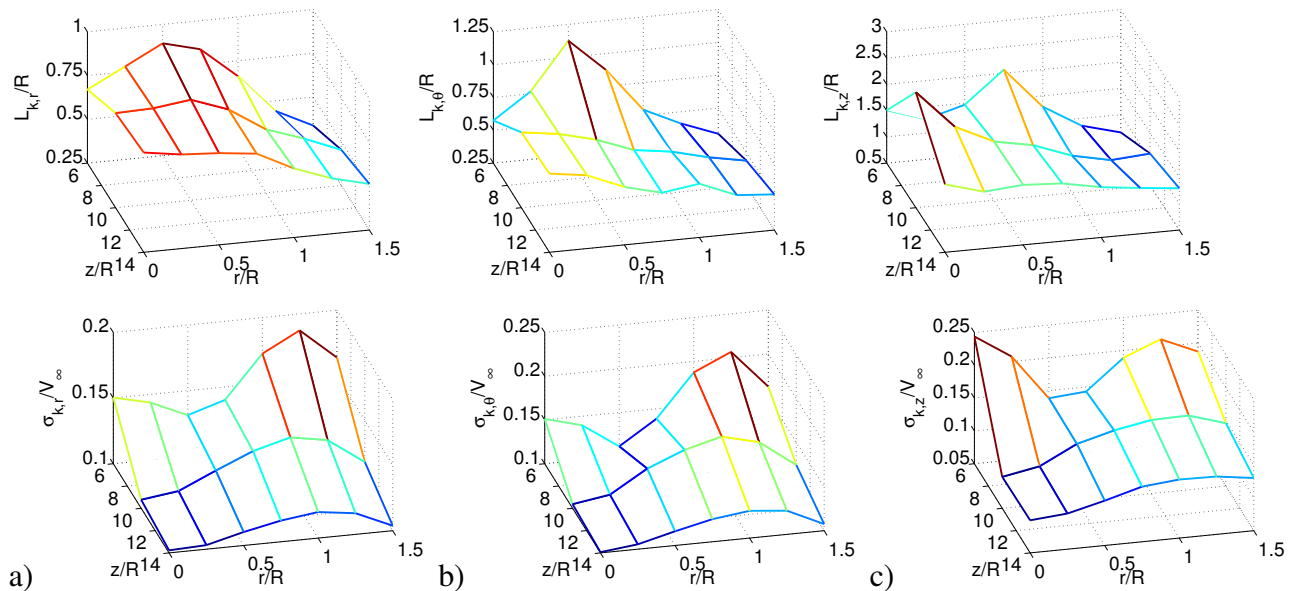


Figure 6.8: Downstream development of  $L_{k,i}$  (top figures) and  $\sigma_{k,i}$  (bottom figures) in the wake of the Tjæreborg turbine operating at  $\lambda = 11.78$ . a) Radial component; b) Tangential component; c) Axial component.

The surface plots of  $\sigma_{k,i}$  displays the same features as figure 6.1, i.e. that the wake generated

turbulent energy is largest in the regions associated with the largest gradients and that the turbulence attenuates and tend to become more spatial homogeneous with downstream position. The variation of the corresponding length scales  $L_{k,i}$  is modest and without a clear trend. However, it seems like the length scales generally correlates negatively with the turbulence intensity. From the figure it is revealed that the typical Kaimal length scale in the wake is respectively in the order  $0.7R$ ,  $0.7R$  and  $1.5R$  for respectively the radial, tangential and axial velocity component. For comparison the corresponding characteristic length scale of the velocity component in the flow direction associated with the atmospheric boundary layer is specified in the IEC code [34] as

$$L_k = 8.1L; \quad L = \begin{cases} 0.7 y & y \leq 60 \text{ m} \\ 42 \text{ m} & y > 60 \text{ m} \end{cases} \quad (6.2)$$

Hence, for the Tjæreborg wind turbine with a radius of  $R = 30.56 \text{ m}$  a characteristic length scale is about  $11R$  which as expected is considerably larger than in the wake.

## 6.5 Coherence

In appendix A it is shown how the coherence can be quantified in terms of the coherence decrement  $C(r_m, \phi_m, \theta, z)$ , where  $r_m$ ,  $\phi_m$  and  $\theta$  are defined in figure A.4. In the following, the coherence is only studied for the axial velocity component since the coherence properties of the other components were expected to be similar.

Figure 6.9 displays the spatial variation of the circumferentially averaged coherence decrement at two sections downstream of the rotor operating at  $\lambda = 11.78$ .

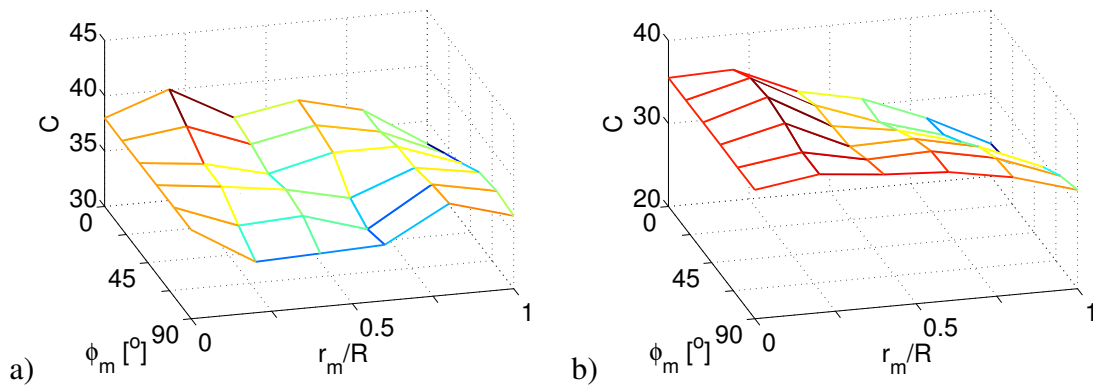


Figure 6.9: Spatial variation of the coherence decrement in the wake of the rotor at  $\lambda = 11.78$ .  
a)  $z/R = 6$ ; b)  $z/R = 14$ .

The coherence decrement is observed to undergo rather small and sporadic variations at  $z/R = 6$  while there at  $z/R = 14$  appears to be a tendency toward smaller values in the outer part of the wake. Furthermore, it seems that the overall level of the coherence decrement is decreasing vaguely with downstream position, which is consistent with the length scales generally being somewhat smaller at  $z/R = 6$  than at  $z/R = 14$ .

## 6.6 Large scale dynamics

In order to study the large scale dynamics of the wake the temporal evolution of the wake center was computed. Inspired by the definition of a center of mass a wake center is here defined in terms of the axial interference factor  $a_z = 1 - V_z/V_\infty$  as follows:

$$\mathbf{R}_c(z, t) = (x_c(z, t), y_c(z, t)) = \frac{\sum_i |a_z(x_i, y_i, z, t)| \mathbf{r}_i}{\sum_i |a_z(x_i, y_i, z, t)|}, \quad \mathbf{r}_i = (x_i, y_i) \quad (6.3)$$

where the summation is carried out over all grid cell at a given downstream position.

Figure 6.10 shows how the x and y coordinates of the wake center evolves in time for a section located 14 rotor radii downstream of the rotor.

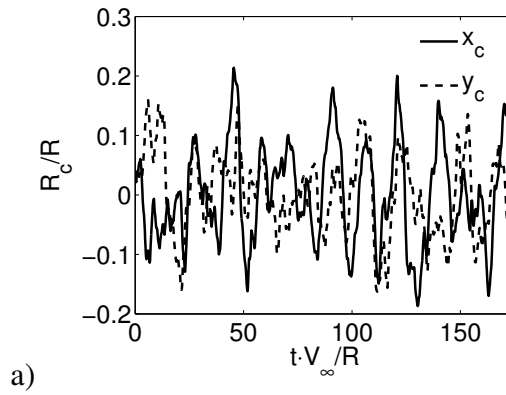


Figure 6.10: Temporal evolution of wake center coordinates in a section located  $14R$  downstream of the rotor operating at  $\lambda = 11.78$

As seen the variability of the two signals is quite small, the standard deviations being in the order of 0.07-0.08, which suggests that wake meandering is modest.

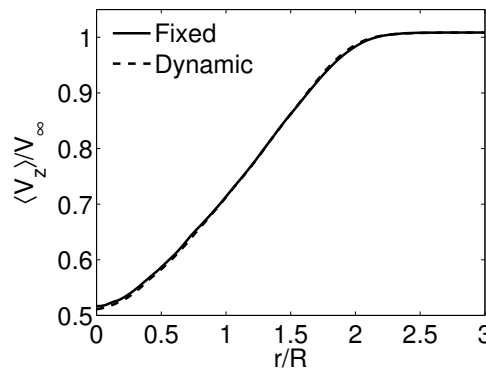


Figure 6.11: Comparison of the mean axial velocity profile with the corresponding profile computed in a frame of reference, which follows the wake center ( $z/R = 14$ ,  $\lambda = 11.78$ ).

The rather insignificant meandering is further illustrated in figure 6.11, which compares the ensemble averaged axial velocity profile computed around the dynamic wake center with the corresponding profile in the fixed frame of reference. As expected, the difference between the two profiles is small due to the vague influence of large scale dynamics.



## 6.7 Summary

This chapter has presented a comprehensive study of the turbulence characteristics in the wake of the Tjæreborg turbine operating in a uniform inflow at tip speed ratios ranging from  $\lambda = 3.21$  to 11.78.

A study of the Reynolds-stresses revealed that, for  $\lambda = 5.05, 7.07$  and 11.78, most of the turbulence is produced in the shear layer formed by the tip and root vortices and that turbulence in the latter case tend to become increasingly isotropic with downstream position. For  $\lambda = 3.21$  the Reynolds-stresses were generally very low and developed fairly insignificantly within the range of explored downstream positions.

For the rotors operating at respectively  $\lambda = 7.07$  and 11.78 it was found that the axial velocity deficit can be considered self-similar for downstream positions beyond respectively, 16 and 7 rotor radii.

An investigation of the spectral characteristics for the same two cases revealed that the turbulent energy generally is distributed on a broad range of frequencies. However, at a position 10 rotor radii downstream of the rotor operating at  $\lambda = 7.07$  there was a clear indication of a rhythmic root vortex.

At  $\lambda = 11.78$  the characteristic length scales of each velocity component was estimated and it was shown that they are considerably lower than those of typical atmospheric turbulence.

Following this, the coherence properties in the wake of the rotor at  $\lambda = 11.78$  was investigated and it was found that the coherence decrement was undergoing moderate variations.

Finally, a study of the dynamics of the wake center revealed rather insignificant wake meandering.

## Chapter 7

# Wind Turbine Wake Aerodynamics in Atmospheric Shear Flow

This chapter explores the wake of the Tjæreborg wind turbine operating in an atmospheric shear flow. The objective is to document the overall development of the wake and to extract some general features of rotor aerodynamics in a standard shear flow.

### 7.1 Mesh configuration

The computations were carried out in a Cartesian computational domain as sketched in figure 2.5b and 2.5c. The dimensions of the grid was  $(L_x, L_y, L_z) = (20R, 24R, 26.8R)$ , where the z-coordinate is in the flow direction. The actuator lines were rotating in the z-plane located 7 rotor radii downstream of the inlet and the point of rotation was placed at  $H = 2R$  above ground.

The grid structure and resolution was comparable to the grid used for the uniform computations, i.e. it was divided into 32 blocks (2 in the x and y direction respectively and 8 in the z-direction) with 64 grid points in each direction and having an equidistant region extending from  $1.3R$  upstream the rotor to  $14R$  downstream. Furthermore, the cross-sectional area of the equidistant region was set to  $2.6R \times 2.6R$  in order to account for wake expansion.

### 7.2 Atmospheric shear layer modeling

The mean wind shear of the atmospheric boundary layer was modeled according to a power law profile

$$V_0(y) = V_\infty \left( \frac{y}{H} \right)^\alpha \quad (7.1)$$

Where the exponent  $\alpha$  was set to 0.2, which is representative for the flow over flat terrain, the mean velocity in hub height was set to  $V_\infty = 10 \text{ m/s}$  and the hub height was set to  $H = 2R$ .

### 7.3 Blade loading

Figure 7.1 shows the azimuth variation of the axial velocity for various radial positions along the blade. Note that an azimuthal angle of  $90^\circ$  corresponds to the blade being oriented vertically upwards.

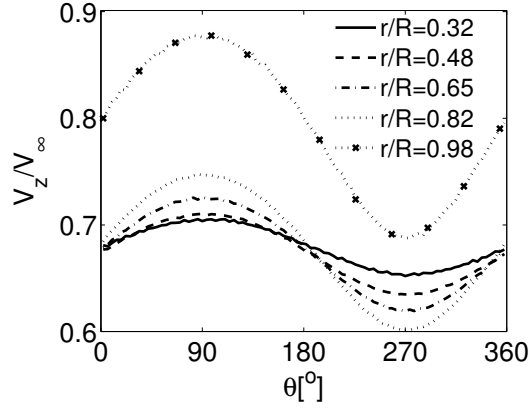


Figure 7.1: Azimuth variation of the axial velocity for various spanwise positions on the blade

As expected the sheared inlet velocity profile causes a nearly sinusoidal behavior of the velocities seen by the blade. From the figure, it also appears that there is no significant phase shift of the velocities. This is more clearly shown in figure 7.2, which depicts the spanwise distribution of the axial velocity at four distinct azimuth positions. Any differences in the axial velocities at the two horizontal positions ( $0^\circ$  and  $180^\circ$ ) are barely visible hence indicating a high degree of horizontal symmetry of the rotor loading.

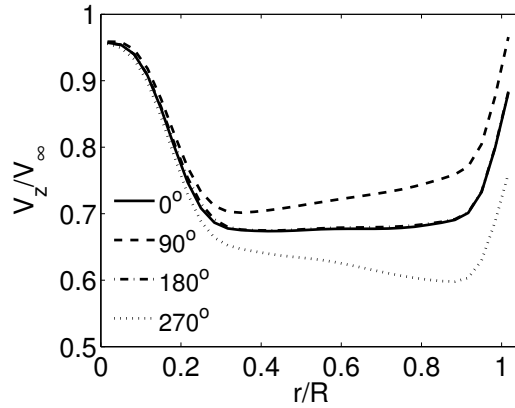


Figure 7.2: Radial distribution of the axial velocity for different azimuth positions.

Figure 7.3 shows the corresponding spanwise distributions of the axial interference factor computed as

$$a_z(r, \theta) = \frac{V_0(y) - V_z(r, \theta)}{V_\infty} = \left(\frac{y}{H}\right)^\alpha - \frac{V_z(r, \theta)}{V_\infty} = \left(\frac{r \sin \theta + H}{H}\right)^\alpha - \frac{V_z(r, \theta)}{V_\infty} \quad (7.2)$$

where  $V_0$  represents the inflow velocity profile given by equation 7.1 and  $V_z$  is the axial velocity at the blade. Comparing figure 7.3 and 7.2 it is evident that the azimuthal variation of the axial

induction is far less than that of the axial velocity. Furthermore, it is interesting to observe that the distribution of the axial induction compares quite well to the induction of the rotor operating in a uniform inflow (figure 4.2), both in terms of shape and level.

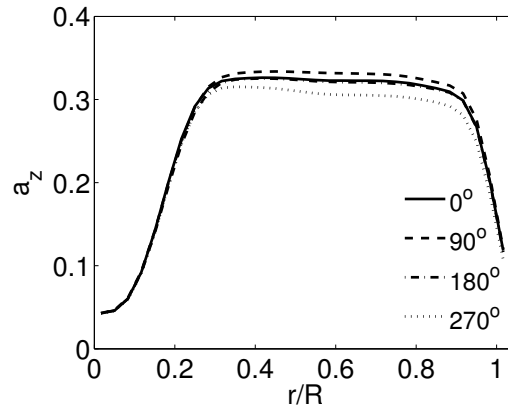


Figure 7.3: Radial distribution of the axial interference factor for different azimuth positions.

Figure 7.4 shows the distributions of circulation,  $\Gamma = L/(\rho V_{rel})$ , along the blade at the four azimuth positions. As in the corresponding uniform inflow case, see figure 4.3, the bound circulation is nearly constant along the blade at all azimuth positions, though as might be expected the circulation is lower when the blade is pointing downwards. The nearly uniform distribution of the bound circulation indicates a wake characterized by concentrated tip and root vortices, while trailing vorticity is marginal.

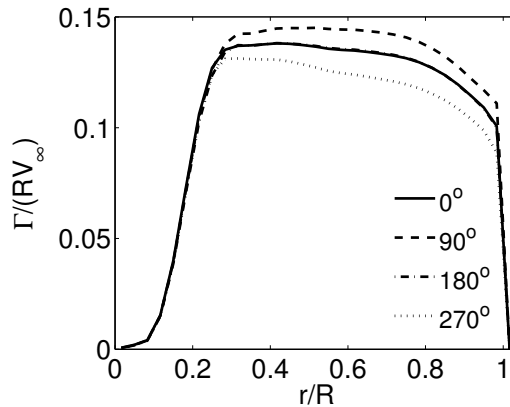


Figure 7.4: Radial distribution of the bound circulation for different azimuth positions.

The radial distribution of respectively the axial and tangential blade forces are depicted in figure 7.5 at the four different azimuth positions. As expected the loading is generally highest when the blade is in its upright position (90°) and lowest when it is pointing downwards (270°). Moreover, in agreement with the observations made about the normal velocities the blade loading is observed to be almost identical at the two horizontal positions 0° and 180°, thereby indicating an insignificant phase-lag. In a recent CFD study on two different wind turbines operating in a strongly sheared flow Zahle and Sørensen [93] reported a modest phase-lag of the blade forces, which caused the loading on the blade to be slightly larger at the horizontal position where the

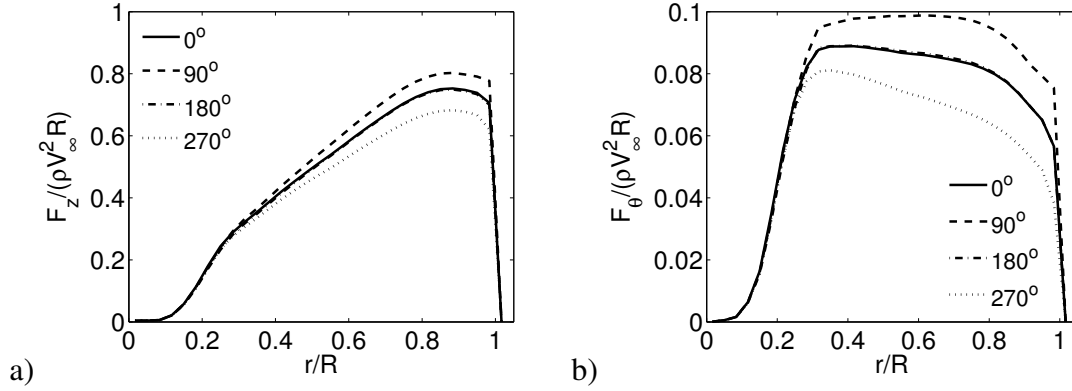


Figure 7.5: Radial distribution of respectively; a) the axial and; b) the tangential force for different azimuth positions.

blade is on its way down ( $180^\circ$ ) than when it is in the horizontal position where it is moving upwards. The phase-lag of the loading can be explained as being attributed to the unsteady effect of vortex shedding due to changes in circulation on the airfoil. This also explains why the phase-lag observed by Zahle and Sørensen [93] was most significant at the inner part of the blade since the local reduced frequency ( $k = \omega c/(2V_{rel})$ ) here is higher due to the larger chord and lower relative velocity.

The reason that a phase-lag do not occur in the actuator line computation is probably that the grid resolution is too coarse to capture the circulatory effect of the airfoil wake. However, it should be emphasized that the phase-lag observed in [93] for a typical MW wind turbine operating in a very strong shear flow was rather small, especially at the outer part of the blade, which, from a load perspective, is most important, and therefore the absence of a phase-lag in the actuator line computations is not considered to be a major issue.

## 7.4 Wake characteristics

Figure 7.6 show contours of the instantaneous absolute vorticity in the vertical plane through the wind turbine center axis ( $x/R = 0$ ). Regions of high vorticity appear as light colors. Note that the rotor is located to the left in the plot and that only the downstream development of the wake is shown.

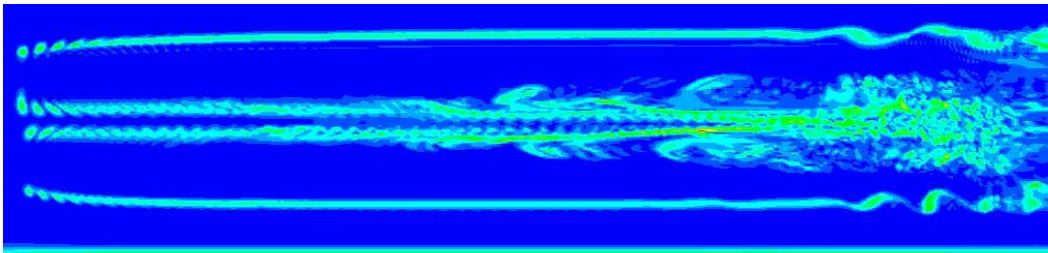


Figure 7.6: Downstream development of the first 15 rotor radii of the wake visualized using vorticity contours. The rotor is located to the left. Regions of high vorticity appear as light colors.

The wake is, as expected from the distributions of bound vorticity (figure 7.4) dominated by the tip and root vortices, while the vorticity trailed from the blades is negligible. Comparing figure 7.6 and figure 4.4 it appears that the behavior of the wake vortex system in the sheared inflow has many similarities to that observed in the corresponding uniform inflow case. However, as expected, a consequence of the inflow velocity shear is that the transport of the tip vortices is slightly larger when in the top position than in the bottom position.

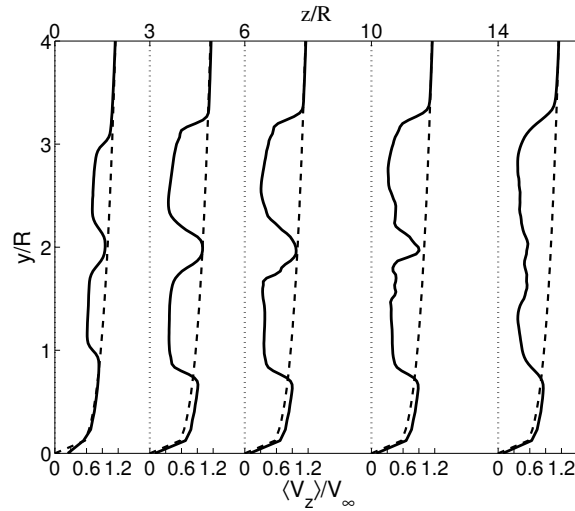


Figure 7.7: Computed profiles of the time averaged axial velocity in a vertical plane going through the rotor center axis. The downstream location is indicated in the top axis.

Figure 7.7 shows the downstream development of the time averaged axial velocity in a vertical plane going through the rotor center axis ( $x/R = 0$ ). In order to give an impression of the induction, the inlet velocity profile defined by equation 7.1 is also included in the figure. The non-symmetric development of the wake is apparent where, in agreement with figure 7.3, the induction is largest in the upper part of the wake. This, however, is not a common feature for wakes in shear flow and generally depends on the degree of shear, the wind turbine and the operational conditions. In the present case the intensity of the tip vortices is highest when in the top position (see figure 7.4) but at the same time the pitch of the vortices is also largest here due to the inflow velocity shear and therefore it is generally difficult to predict in advance whether the largest deficit will occur in the upper or lower part of the wake. The presence of the ground causes the wake to expand more upwards than downwards and also make the ambient flow accelerate below the rotor and the wake. Another interesting feature to observe is that the wake, in contrast to the uniform inflow case, apparently does not, to the same extent, reach an equilibrium stage as e.g. it is evident that the velocity deficit 6 and 10 rotor radii downstream differs somewhat from each other. Finally, it is noted that even though the wake is not fully developed 14 rotor radii downstream it is evident that the wake does not develop toward the same Gaussian shape as observed in the uniform inflow case.

In figure 7.8 the axial interference factor is plotted as a function of height for various downstream positions. Also included in the figure, is the curve representing the induction in the rotor plane multiplied with two, in order to facilitate a direct comparison with the predictions of the BEM method. Evidently, in the upper part of the wake the induction is generally more than twice that in the rotor plane, while the opposite is true in the lower part of the wake.

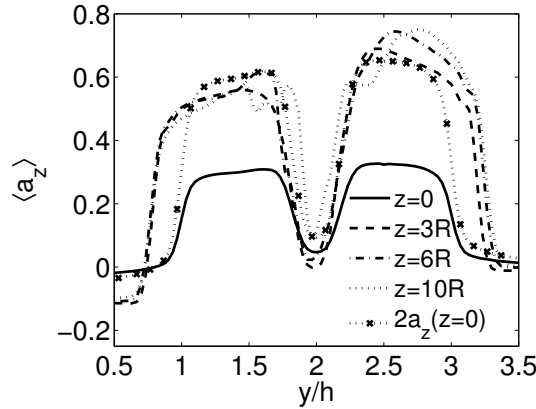


Figure 7.8: Computed profiles of the time averaged axial interference factor in a vertical plane through the rotor center axis. The different downstream positions are indicated in the figure.

Figure 7.9 shows the development of the normalized tangential velocity in the same cuts as in figure 7.7 and again the asymmetric development is clearly visible. It is interesting to note that despite the bound circulation being lowest when the blade is in its downward position (figure 7.4) this is not reflected in the development in the wake, where it is clear that the tangential velocity develops toward the largest values in the lower part of the wake. This behavior of the tangential velocity could be related to the wake expanding more upwards than downwards as revealed from figure 7.7.

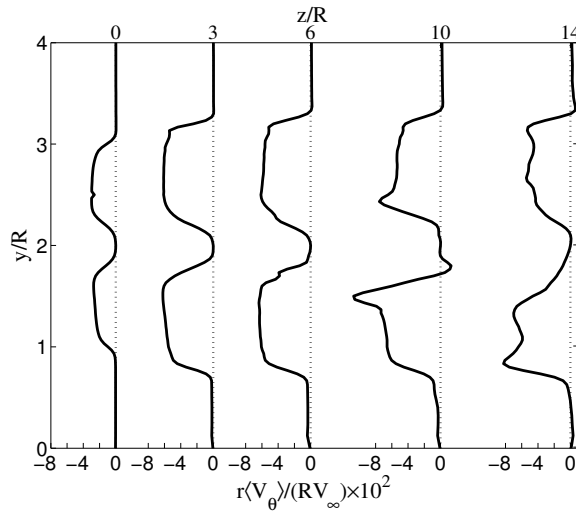


Figure 7.9: Computed profiles of the time averaged tangential velocity in a vertical plane going through the rotor center axis. The downstream location is indicated in the top axis.

In order to give a more clear impression of the asymmetric development of the wake figure 7.10 presents the contours of the time averaged axial velocity at various downstream positions. The mean in-plane velocity field is presented as vectors. The view is from downwind, i.e. the azimuth position corresponding to  $0^\circ$  is to the right.

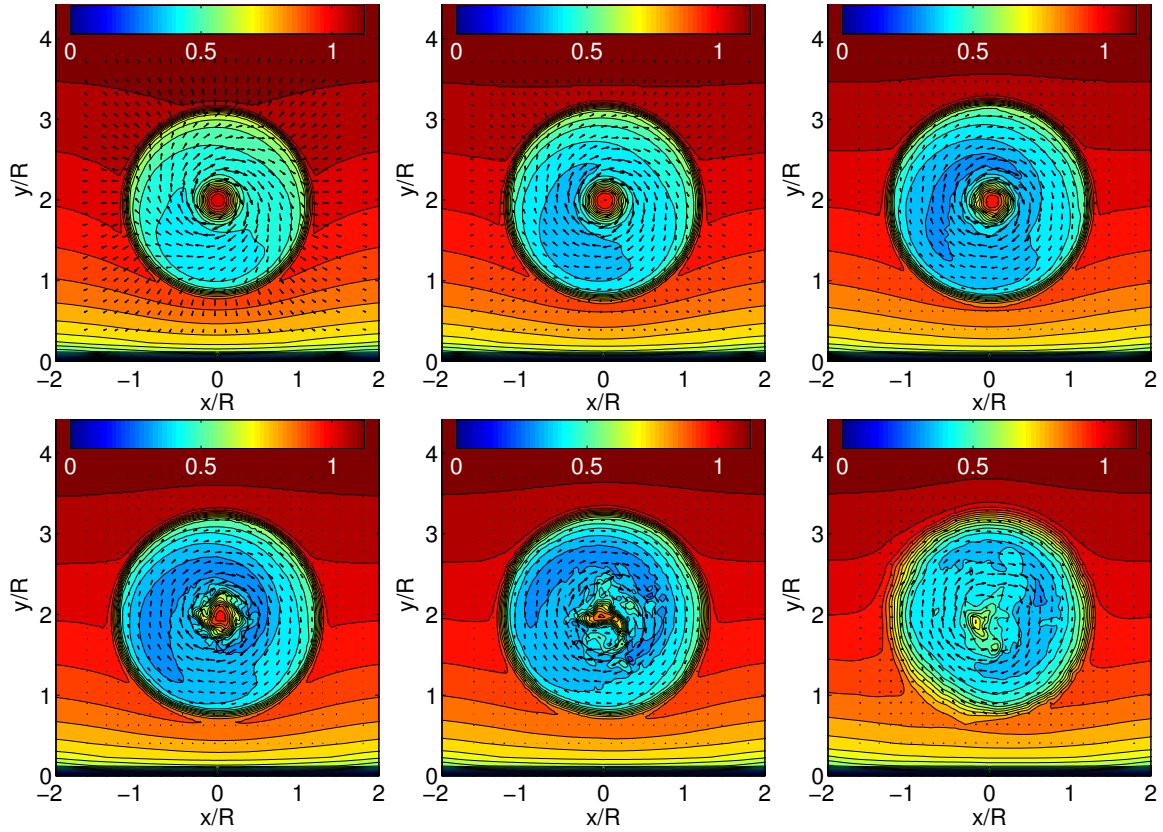


Figure 7.10: Contours of the mean axial velocity field in the wake. The mean in-plane velocity is presented as vectors. From left to right:  $1R$ ,  $2R$ ,  $4R$ ,  $6R$ ,  $10R$  and  $14R$  downstream of the turbine.

The most important observation to make from the figure is that the rotation of the wake seems to cause a redistribution of the axial velocity deficit and thereby the wake becomes horizontally asymmetric as it is transported downstream. This behavior is in very good qualitative agreement with both the CFD study of Zahle and Sørensen [93] as well as with measurements presented in [10].

Figure 7.11-7.14 presents the contours of the four main components of the Reynolds stress tensor at three downstream positions. Again the view is from downwind. Below each contour plot the radial distribution of the respective Reynolds stress is presented for four distinct azimuth positions in order to give a more quantitative impression of its behavior. Note, that as the wake is no more rotationally symmetric the two components  $\langle v_r v_\theta \rangle$  and  $\langle v_\theta v_z \rangle$  are now non-zero. However, a closer inspection of these components revealed that they were still significantly lower (an order of 3 – 4 times less) than the component  $\langle v_r v_z \rangle$  and hence they are not shown here. Generally, the normal stress in the flow direction is the dominant component attaining approximately twice as large values as the in-plane normal stresses. The shear stress attains values comparable to the in-plane normal stresses, though as expected with a different sign over the bulk of the wake. The non-zero shear stress and the difference in the normal stresses reveal that the Reynolds stresses exhibit significant anisotropy.



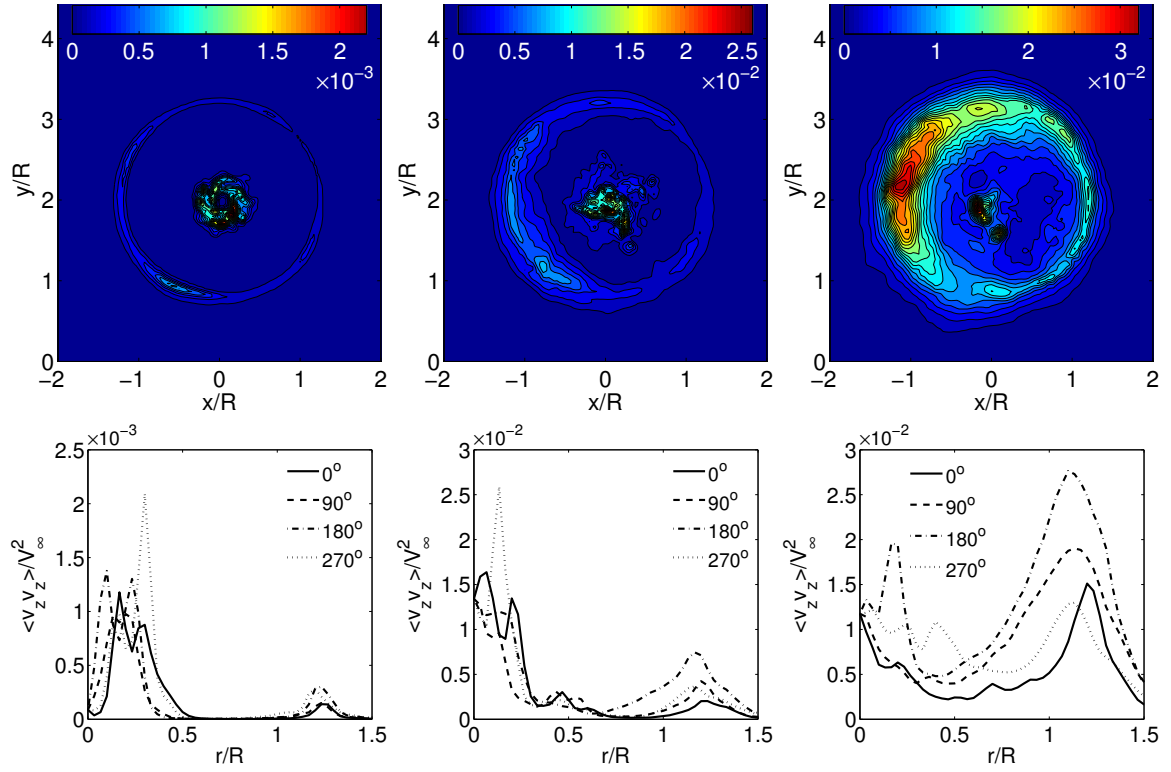


Figure 7.11: Contours of  $\langle v_z v_z \rangle$ . From left to right: 6R, 10R and 14R downstream. The figures below each contour plot show the corresponding radial distribution for four different azimuth positions.

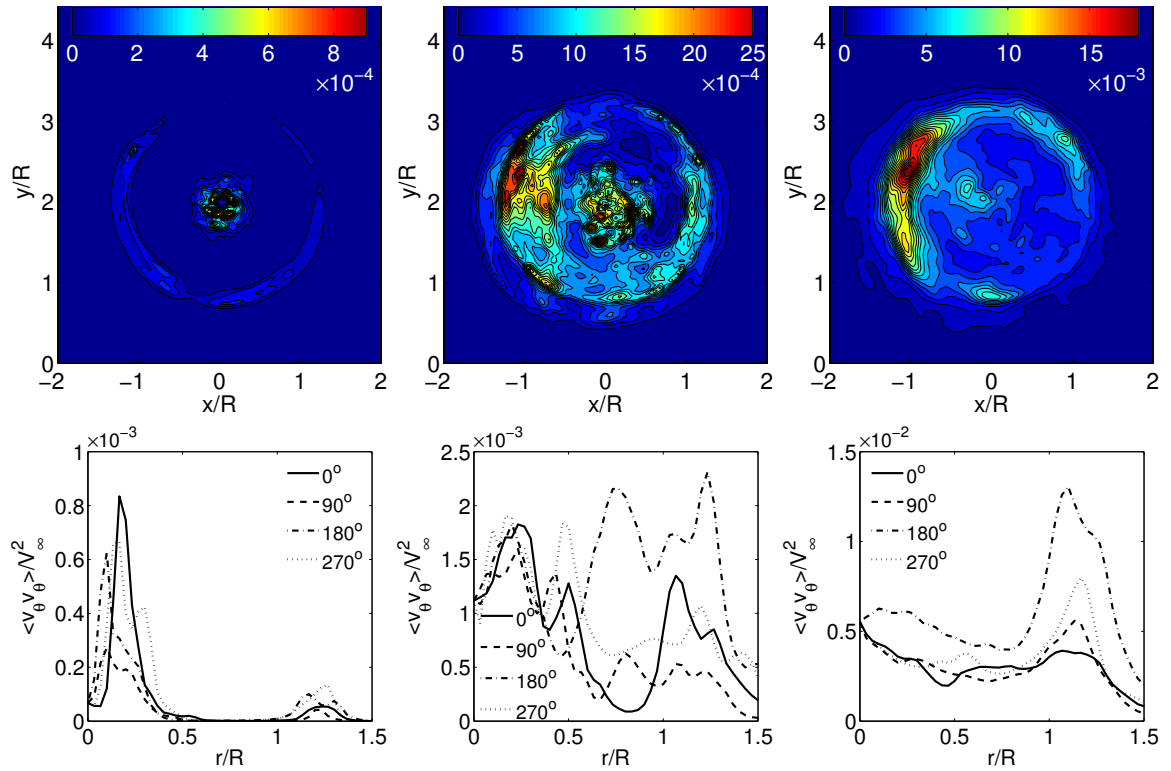


Figure 7.12: Contours of  $\langle v_\theta v_\theta \rangle$ . From left to right: 6R, 10R and 14R downstream. The figures below each contour plot show the corresponding radial distribution for four different azimuth positions.

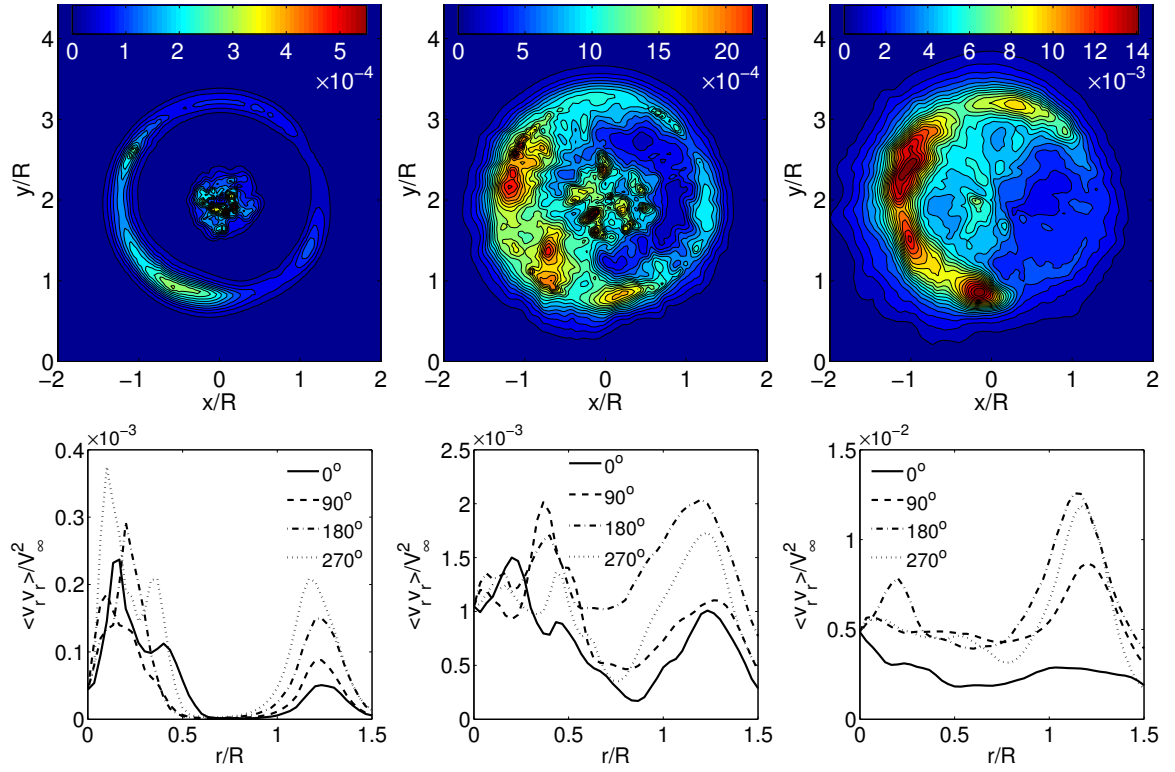


Figure 7.13: Contours of  $\langle v_r v_r \rangle$ . From left to right: 6R, 10R and 14R downstream. The figures below each contour plot show the corresponding radial distribution for four different azimuth positions.

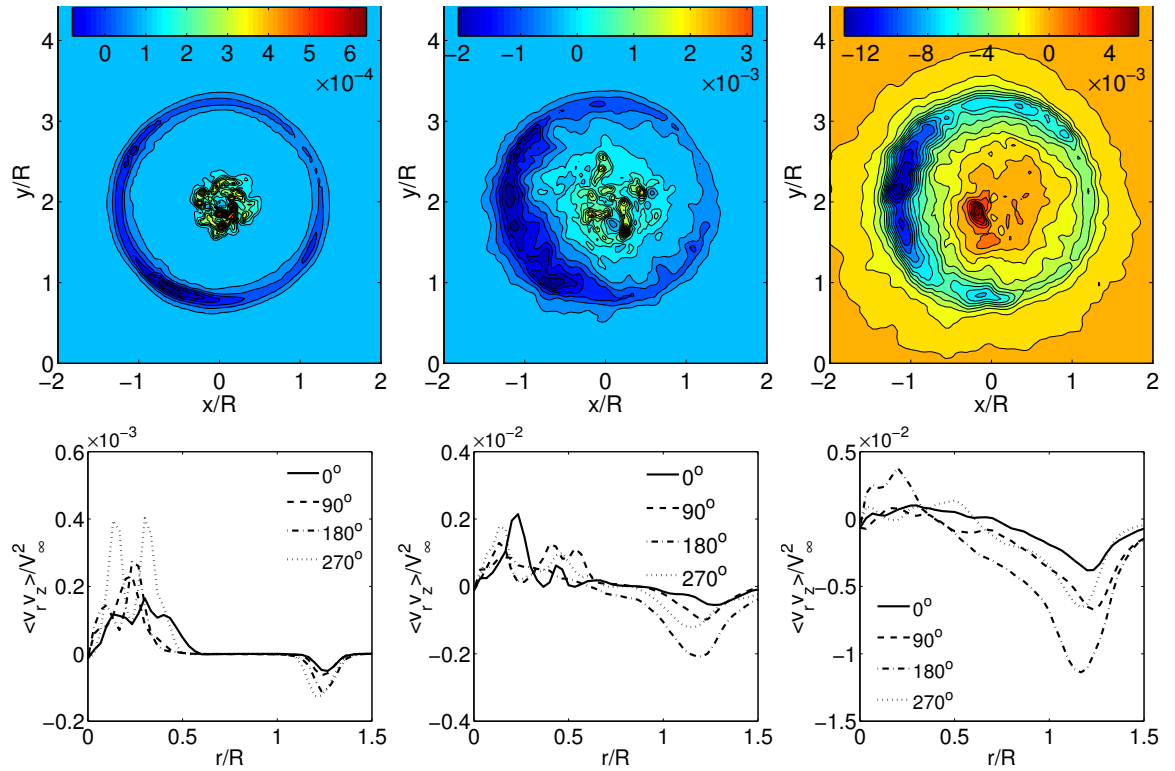


Figure 7.14: Contours of  $\langle v_r v_z \rangle$ . From left to right: 6R, 10R and 14R downstream. The figures below each contour plot show the corresponding radial distribution for four different azimuth positions.

At the section located 6 rotor radii downstream of the rotor all components of the Reynolds stress tensor are generally small and are mainly located in the center of the wake, due to the unstable root vortices. As the tip vortices become increasingly unstable with downstream position the Reynolds stresses in the shear layer located in the annular domain surrounding the blade tips increase significantly. However, it is clear that, due to the rotation of the wake, the turbulence generated in the shear layer is not rotationally symmetric within the investigated downstream positions.

Furthermore, the figures reveal how the thickness of the shear layer formed by the tip vortices increase due to turbulent diffusion. Evidently, at the final investigated stage the shear layer is still distinct revealing that most of the turbulence is produced by the shear from the tip vortices at this point and that the wake is not fully developed.

## 7.5 Summary

The wake of the Tjæreborg wind turbine operating in a moderately sheared inflow has been simulated.

Initially, it was shown that while the velocities experienced by the blades as expected varied significantly during one rotor revolution the induced velocities were rather constant over the rotor disk. Furthermore, it was shown that the loading on the blades revealed very little horizontal asymmetry, which however most probably is due insufficient grid resolution.

Secondly, it was shown that the vortex instabilities formed downstream of the turbine was quite similar to those observed in the corresponding uniform inflow case, though as expected the vortex system was clearly skewed due to the velocity shear.

Besides an expected vertical skew of the velocities and the Reynolds stresses in the wake it was also observed that these quantities were gradually becoming more asymmetric in the horizontal direction as the wake was transported downstream. This horizontal asymmetry appeared to be a consequence of the rotation of the wake, which caused low velocity air from the bottom part of the wake to move upwards on one side and high velocity air from the upper part of the wake to move downwards on the other side. Moreover, it was shown that the wake due to the presence of the ground expanded more upwards than downwards and that the ambient flow accelerated below the rotor and the wake.

# Chapter 8

## Wind Turbine Wake Aerodynamics in Turbulent Inflow - Initial Results

The wake of the Tjæreborg wind turbine operating in an atmospheric turbulent inflow without mean wind shear is simulated and the results are compared to those obtained in laminar inflow with the objective of studying the overall influence of ambient turbulence on the wake behavior. Besides providing the initial results of the wake characteristics of a turbine operating in a turbulent inflow this chapter also presents a validation of the method used for imposing inflow turbulence. The contents of this chapter were originally presented in [82].

### 8.1 Numerical setup

The computations were carried out in a numerical grid identical to the one used in chapter 4-6. The atmospheric turbulence was modeled using the method described in 2.3.2 where artificial turbulent fluctuations from a pre-generated turbulence field are introduced in a plane located upstream of the rotor.

The turbulence field was generated using the algorithm by Mann [48], [49] assuming a mean wind speed of  $V_\infty = 10 \text{ m/s}$ , a height above ground of  $y = 60 \text{ m}$  and a roughness height of  $y_0 = 0.05 \text{ m}$ . The given parameters correspond to a friction velocity  $u_*$  of  $0.54 \text{ m}$  and a turbulence intensity of approximately 0.09. The turbulence field was furthermore fitted to all three components of the Kaimal spectrum  $S_{k,i}$ , which in its two-sided form is given by [49]:

$$\frac{f S_{k,x}}{u_*^2} = \frac{8.5n}{(1 + 9.5n)^{5/3}}; \quad \frac{f S_{k,y}}{u_*^2} = \frac{1.05n}{1 + 5.3n^{5/3}}; \quad \frac{f S_{k,z}}{u_*^2} = \frac{52.5n}{(1 + 33n)^{5/3}}; \quad (8.1)$$

Here  $f$  is the frequency and  $n \equiv fy/V_\infty$ .

The dimensions of the generated turbulence box was  $L_x \times L_y \times L_z = 8R \times 8R \times 128R$  and from this domain a box of dimensions  $4R \times 4R \times 128R$  was extracted to avoid problems related to the periodicity of the turbulence field as mentioned in section 2.3.2. The number of grid points in the final turbulence box was  $64 \times 64 \times 2048$  resulting in a grid with a resolution corresponding to 16 grid point per rotor radii. The turbulence field was introduced in a  $z$ -plane located 6 rotor radii downstream of the inlet (i.e. 1 rotor radius upstream of the rotor) and with its center point in the center of the domain.

## 8.2 Inflow turbulence decay

Obviously, with the used method for modeling inflow turbulence the turbulent fluctuations will decay as they are transported downstream since there is no production to balance the dissipation.

In order to quantify the rate of turbulence decay the generated turbulence field was initially imposed in a purely uniform flow field (i.e. without including the wind turbine) and its development was studied in a number of downstream sections.

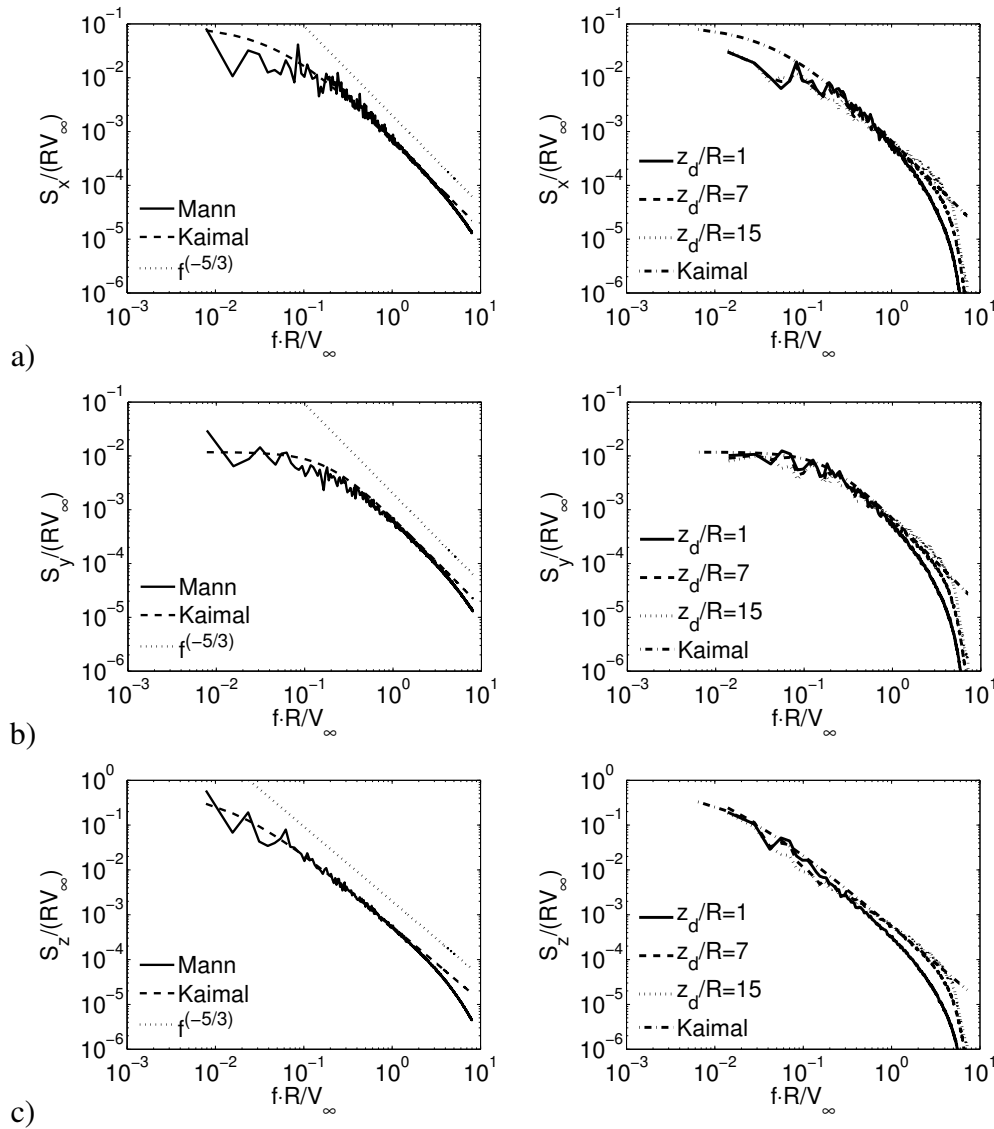


Figure 8.1: Comparison of the analytical Kaimal spectrum with the spectrum of the introduced turbulence field. Left: Initial spectra. Right: Downstream development of one dimensional spectra. a)  $x$ -velocity; b)  $y$ -velocity; c)  $z$ -velocity.

Figure 8.1 compares the theoretical Kaimal spectra with respectively the spectra computed directly from the input turbulence field produced by the Mann algorithm (left) as well as with the spectra obtained at three different sections downstream of the turbulence grid (right). Please, note that the spectra are averages over the entire domain.

The left figures show the initial spectral characteristics of the turbulence field. As seen the resemblance between the theoretical and computed spectra is generally good over most of the frequency range. The reason that the computed turbulence field has somewhat lower energy at the highest frequencies is that the turbulence wind field is spatially averaged over each grid cell [49].

The right plots of figure 8.1 show the evolution of the spectral characteristics with downstream position. As seen the spectra obtained  $1R$  downstream of the turbulence plane is characterized by having a rather steep slope in the inertial sub range, however, further downstream the slope apparently return to the theoretical value. This transient behavior occurs because the input turbulence field is not a solution to the full Navier Stokes equations and hence needs to adapt to the numerical solver.

From figure 8.1 it appears that the decay of turbulence is rather low but it is somewhat difficult to see. A clearer plot is obtained by integrating the one dimensional spectra over the entire frequency range to obtain an estimate of the variance,  $\sigma^2$ , of the turbulent velocity, i.e.

$$\sigma_i^2 = \int_0^\infty S_i df \quad (8.2)$$

Figure 8.2 shows the estimated standard deviation of each velocity component as a function of the distance to the turbulence plane.

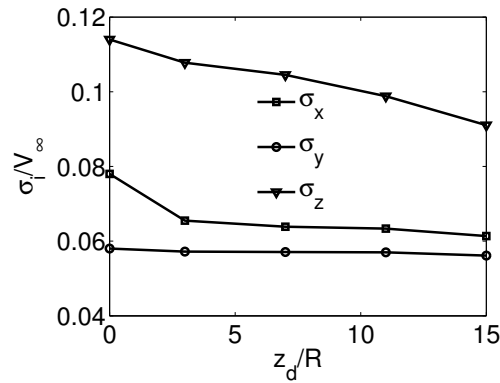


Figure 8.2: Downstream development of the spatially averaged standard deviation of each velocity component

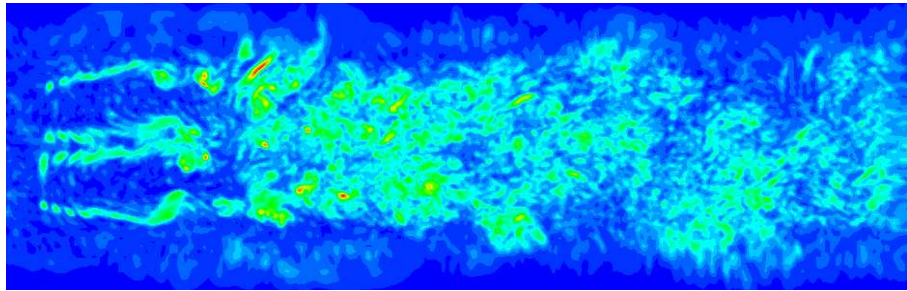
As seen the standard deviation of the axial component,  $\sigma_z$  decreases continuously with downstream position and reaches a level of approximately 80% of the initial value. The component  $\sigma_x$  initially drops rapidly and then reaches a rather constant value, whereas the last component stays nearly constant over the entire region.

The above study verifies that the imposed turbulent fluctuations, though of course decaying, remain significant throughout the region of interest and hence should be useful for the present study. It should be appreciated, however, that the method may be problematic in studies on large wind farms since the turbulence decay in these cases may be significant for turbines placed far from the turbulence plane.

### 8.3 Wake characteristics

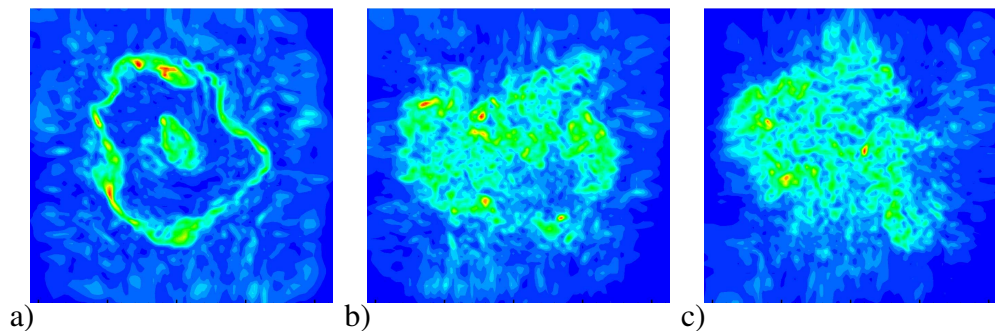
This section presents the initial results from the simulation of the wake generated behind the Tjæreborg wind turbine operating in an unsteady inflow. In the computation the mean wind speed was  $V_\infty = 10 \text{ m/s}$  corresponding to a tip speed ratio of  $\lambda = 7.07$ . The wake of the turbine operating in laminar inflow at the same tip speed ratio was presented in chapter 4-6 and thus a comparison can reveal the overall influence of the unsteady inflow on the wake.

Figure 8.3 shows the development of the first 15 rotor radii of the wake by displaying instantaneous contours of the absolute vorticity in a slice intersecting the wind turbine center axis.



*Figure 8.3: Downstream development of the wake visualized using vorticity contours. The rotor is located to the left.*

Comparing with the corresponding figure for the turbine operating in a uniform inflow (figure 4.4) it is evident that the ambient turbulence causes dramatic changes in the wake development. The external turbulent fluctuations perturb the vortex system, whereby the wake become unstable much closer to the rotor. From the visualization it is possible to identify various coherent flow structures in the wake the largest of which are clearly much larger than the diameter of the rotor and appears as a meandering of the wake. Organized structures due to the presence of the tip and root vortices can be distinguished up to approximately 6 rotor radii behind the rotor but further downstream the interior of the wake seems to be fully turbulent. It is interesting to observe that at the shown instant there is a region approximately 7 rotor radii downstream where the wake apparently undergoes a contraction so that the radial extent of the wake at this point appear smaller than the rotor diameter. The same observation was made in the work of Binöl et al. [9] and is most likely due to a combination of large scale out of plane motion and stretching of the wake. The stretching of the wake is more apparent in figure 8.4, which shows



*Figure 8.4: Absolute vorticity contours in sections located respectively 2 (a), 6 (b) and 10 (c) rotor radii behind the turbine*

vorticity contours at three different downstream cross sections in the wake. From the figure it is further seen that the tip and root vortices are unstable already 2 rotor radii downstream of the turbine and that the wake in the section 10 rotor radii downstream clearly has broken down to small scale turbulence.

In figure 8.5 the development of the axial velocity in the wake is shown and compared to the corresponding results in uniform inflow. The shown profiles are averaged in both time and in the circumferential direction.

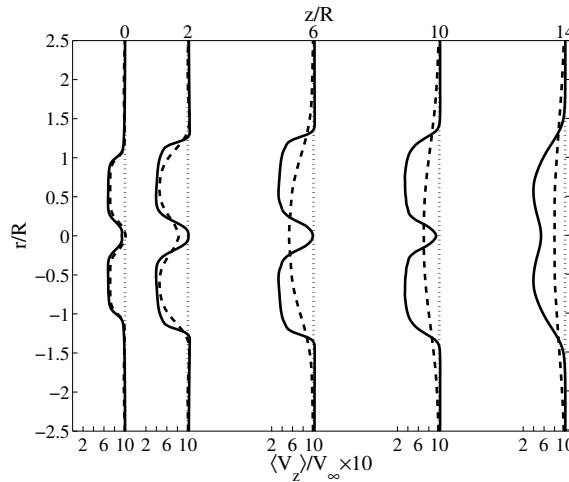


Figure 8.5: Downstream development of the time and circumferentially averaged axial velocity deficit for the turbine in respectively a uniform (full line) and a turbulent inflow (dashed line).

The wake of the rotor in uniform inflow is characterized by having a nearly constant velocity over most of the radial distance, which indicate a wake governed by the induction of stable tip and root vortices. On the other hand, the wake of the rotor operating in a turbulent inflow is seen to undergo a rapid transition into a bell shaped velocity deficit indicating that the wake becomes dominated by small scale turbulence. However, this wake shape could also be partly attributed to large scale wake meandering - indeed a sharper wake deficit might be found if the computed average velocity profiles were based on a point following the center of the wake. This issue is addressed in more details in the next chapter.

Figure 8.6 shows the azimuthally and temporally averaged normalized tangential velocity profiles at various downstream sections for both the tested cases.

The figure clearly reveals that, while swirl in the wake is significant for all downstream sections in the uniform inflow case, it decays rapidly toward zero when inflow turbulence is present. Note, that the quantity presented in figure 8.6 is also a measure of the amount of circulation in the wake. In chapter 5 it was found that circulation is fairly conserved in the wake of a rotor in uniform inflow as long as viscous phenomena are not too dominant. However, the rapid decay of the tangential velocity when turbulence is introduced to the inflow indicates that circulation is generally not well conserved in the wake.



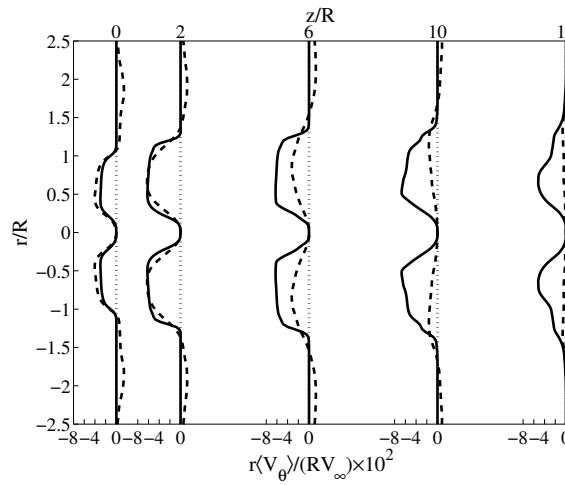


Figure 8.6: Averaged tangential velocity profiles at different downstream positions for the rotor operating respectively in uniform inflow (full line) and turbulent inflow (dashed line).

## 8.4 Summary

The wake of the Tjæreborg wind turbine operating in an atmospheric turbulent flow without shear has been simulated and the initial results presented. Through a comparison with a similar simulation carried out on the same wind turbine subject to uniform inflow the influence of atmospheric turbulence on the wake dynamics has been studied. The ambient turbulence field was shown to perturb the tip vortices whereby the wake breaks up much closer to the rotor than in a laminar inflow. The break down of the vortices causes the wake to undergo a transition into a fully turbulent state characterized by a bell-shaped mean axial velocity profile and a nearly negligible mean tangential velocity.

Besides the studies of the wake development an investigation of the decay of the imposed atmospheric turbulence in a uniform flow field was also conducted. The study showed that even though the turbulence, as expected, decays as it is convected downstream it remains significant throughout the entire region of interest and therefore it was concluded that the method of imposing artificial turbulence upstream of the rotor is useful for studying the influence of inflow turbulence on the wake behavior.

# Chapter 9

## Wind Turbine Wake Aerodynamics in Turbulent Non-Sheared Inflow - Turbulence Characteristics

The fundamental turbulence characteristics of the wake of respectively the Tjæreborg and the NM80 wind turbine operating in atmospheric turbulent inflow without a mean shear are studied and the results are compared with the aim of extracting general features of wind turbine wake turbulence. The investigation of the Tjæreborg Turbine is based on the simulation presented in the previous chapter. The simulation of the NM80 turbine was conducted at  $V_\infty = 10 \text{ m/s}$  and using the same numerical mesh as the one used for the Tjæreborg turbine. Hence the numerical setup in the two computations is identical in every respect except for the characteristics of the imposed turbulence field.

Most of the contents of the present chapter were presented in [83] and it basically follows the same steps as shown in chapter 6 for a turbine in laminar inflow, i.e. includes calculation of Reynolds-stresses, length scales, spectral characteristics and coherence properties as well as a study of whether the results are consistent with the assumption of self-similarity. Finally, this chapter presents a POD analysis and in this connection discusses some large scale wake phenomena.

### 9.1 Inflow turbulence characteristics

The most relevant characteristics of the inflow turbulence fields in connection with the present analysis are presented in table 9.1 and 9.2. Note that since the inflow turbulence is spatially

<i>Dir</i>	$L_{k,i}/R$	$\sigma_i/V_\infty$ [%]	$C_{i,\Delta x}$	$C_{i,\Delta y}$
<i>x</i>	3.1	7.8	—	—
<i>y</i>	1.3	5.8	—	—
<i>z</i>	10.8	11.2	9.8	6.1

*Table 9.1: Characteristics of inflow turbulence used in the computation on the Tjæreborg turbine*

homogeneous the Kaimal length scales, the standard deviation and the coherence decrement,  $C$ ,

$Dir$	$L_{k,i}/R$	$\sigma_i/V_\infty$ [%]	$C_{i,\Delta x}$	$C_{i,\Delta y}$
$x$	2.3	6.2	—	—
$y$	0.9	4.6	—	—
$z$	8.2	8.8	10.9	6.7

Table 9.2: Characteristics of inflow turbulence used in the computation on the NM80 turbine

is constant and that the results presented in table 11.1 and 11.2 are computed as an average over the entire cross-section. The subscripts  $i = \{x, y, z\}$  refer to the velocity component and the subscript,  $\Delta x$  and  $\Delta y$  of  $C$  refer to separation in respectively x and y direction. Furthermore, it should be emphasized that the length scales of the two turbulence fields in fact are very similar the reason for the differences being that they are scaled with two different rotor radiuses.

## 9.2 Validation - comparison with measurements

Table 9.3 presents the computed thrust coefficient as well as the computed and measured power coefficient for both wind turbines.

Wind turbine	$C_T$ (computed)	$C_P$ (computed)	$C_P$ (measured)
Tjæreborg	0.8	0.51	0.49
NM80	0.70	0.48	0.47(electrical)

Table 9.3: Thrust and power coefficient for respectively the Tjæreborg and NM80 wind turbine at a mean wind speed of  $V_\infty = 10$  m/s.

The table reveals good agreement between measured and computed power coefficient for both turbines, the differences being most likely due to inaccurate airfoil data.

To further validate the simulations, the computed profiles of respectively the mean axial velocity and the standard deviation of the axial velocity obtained 5 rotor radii downstream of the NM80 wind turbine was compared with measurements at the same downstream positions. The result is presented in figure 9.1. Note that for the measured mean velocity data, ambient wind speeds in the range 9 – 11 m/s have been considered, reflecting the usual balance, between amount of available data and the selected bin size [43].

The scatter of the mean velocity measurements is considered mainly to be due to the applied binning. On the other hand the binning does not influence the scatter of the measured standard deviation since these are normalized with respect to the actually observed mean wind speed. The scatter in the measured standard deviation is therefore most likely associated with varying atmospheric stability conditions.

The simulated results of both mean velocity and standard deviation agree reasonable with the corresponding measured data, both with respect to shape, expansion and magnitude. The observed discrepancies between measured and simulated results are most likely due to differences in the inflow conditions. However, in the center of the wake both the mean velocity and standard deviation are over predicted because the nacelle is not present in the simulation.

It should be appreciated that validating the simulations in terms of a limited set of mean wake measurements, as the one used here, may be questionable because any observed agreement or disagreement might be somewhat coincidental.

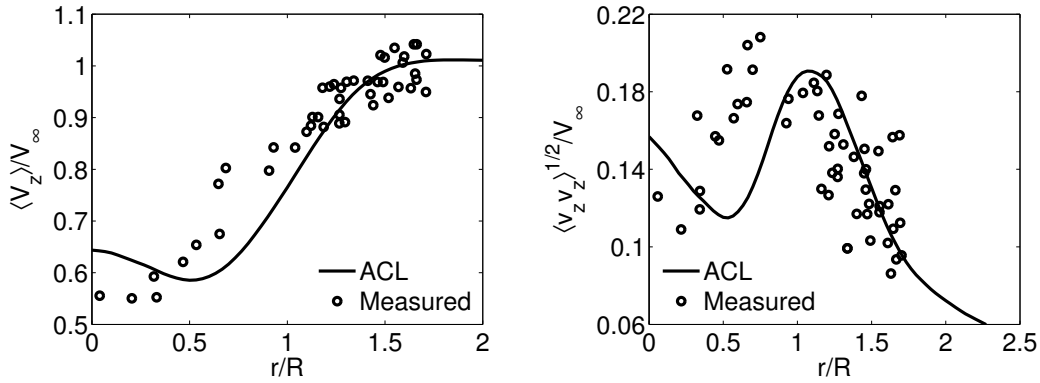


Figure 9.1: Computed and measured profiles of respectively a) mean axial velocity and b) axial turbulence intensity in a section located  $5R$  downstream of the NM80. The ambient mean wind speed is  $V_\infty = 10 \text{ m/s}$  and the axial turbulence intensity is 9%.

### 9.3 Reynolds stresses

Figure 9.2-9.3, presents the radial distribution of the four main components of the Reynolds-stress tensor at different positions downstream each turbine. All the shown curves are averaged in the circumferential direction. The two components  $\langle v_r v_\theta \rangle$  and  $\langle v_\theta v_z \rangle$  are not shown here since they are zero due to circumferential symmetry [63].

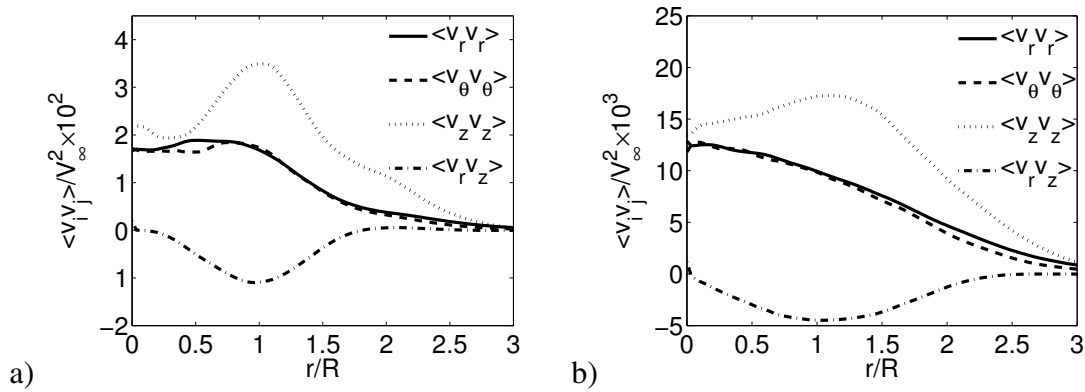


Figure 9.2: Profiles of the Reynolds-stresses at different sections downstream of the Tjæreborg turbine. a)  $z/R = 6$ ; b)  $z/R = 14$

As seen the Reynolds stresses at  $z/R = 6$  generally maximizes in the region of the tip vortices but as the wake move downstream the Reynolds-stress distributions develop toward a bell shaped form. As in the steady uniform inflow case the transition toward a bell shaped profile is cf. figure 8.5 observed to be slower for the Reynolds stresses than for the mean velocity profile revealing that the decay of turbulence is less rapid than the decay of the mean velocity deficit. However, as expected the development is stronger in the present cases than when the turbine operates in a laminar inflow because the vortex system breaks up much earlier, when it is perturbed by the ambient turbulence field. Another important observation is that the Reynolds-stresses exhibit increasingly isotropy with downstream position, nevertheless the wake is still rather far from being isotropic at  $z/R = 14$ .

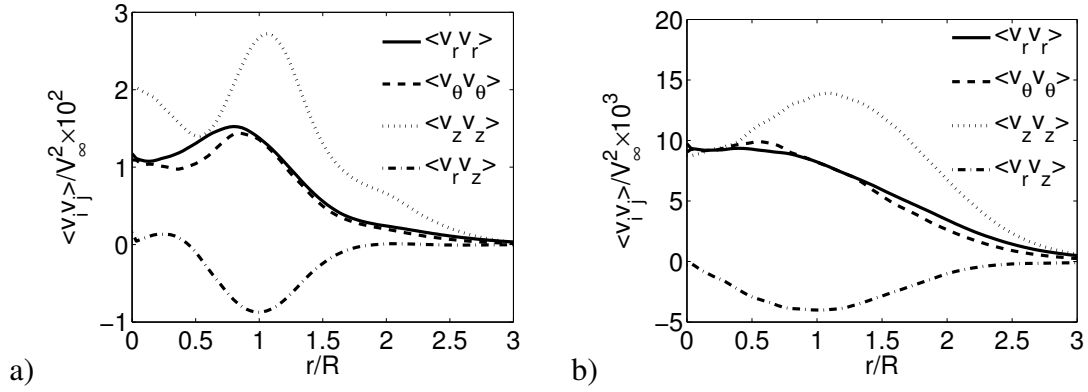


Figure 9.3: Profiles of the Reynolds-stresses at different sections downstream of the NM80 turbine. a)  $z/R = 6$ ; b)  $z/R = 14$

## 9.4 Self-similarity

Figure 9.4 presents the mean axial velocity profiles in the wake of each turbine in terms of the scaled velocity variable,  $f_v$  defined in equation A.24 of appendix A. For comparison the figure also includes the analytical constant eddy-viscosity solution, which is given by

$$f_v(\xi) = \exp(-\alpha\xi^2) \quad (9.1)$$

where  $\alpha = \ln 2$  and  $\xi = r/r_{1/2}$ .

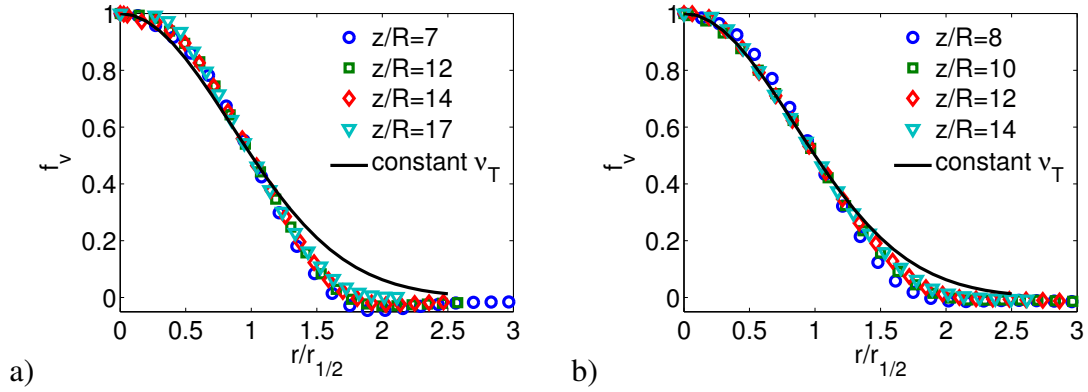


Figure 9.4: Self-similar velocity profiles downstream of each turbine. a) Tjæreborg; b) NM80

As seen the mean axial velocity can be assumed self-similar approximately 7 and 8 rotor radii downstream of respectively the Tjæreborg and the NM80 since all scaled profiles after this point nearly collapse on a single curve. The analytical solution compare very well with the computed results in the inner part of the wake but differ in the outer part, as expected.

## 9.5 Spectral characteristics

Figure 9.5-9.6 show the spectral characteristics of the streamwise velocity component at different radial and downstream positions for each turbine. All the spectra have been computed using

spectral averaging in the circumferential direction. The corresponding spectra of the radial and tangential velocity components are not shown here since these, as for the uniform inflow case, were found to exhibit a spectral behavior similar to the axial velocity. However, in section 9.6 all spectra will be characterized by the standard deviation  $\sigma_{k,i}$  and the characteristic length scale  $L_{k,i}$ . For comparison the analytical Kaimal spectrum (equation 8.1) of the input turbulence is also shown in the figures.

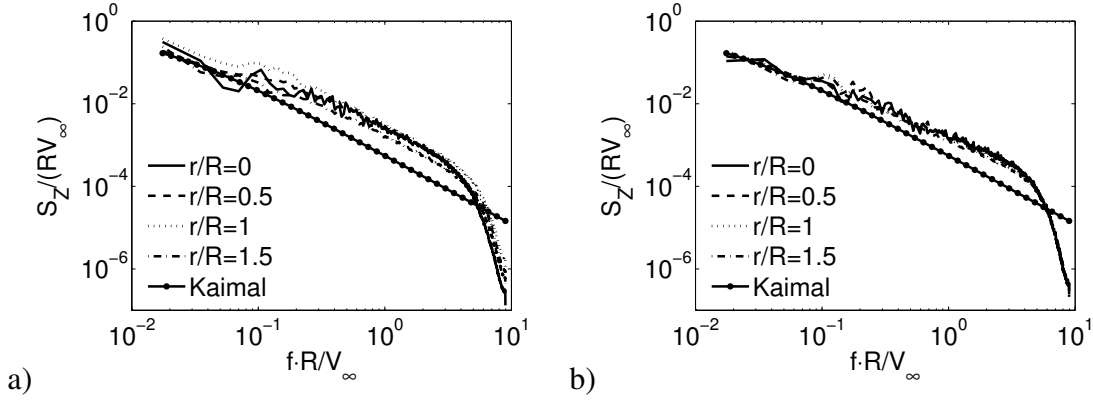


Figure 9.5: Spectra of the axial velocity in the wake of the Tjæreborg turbine at a)  $z/R = 6$  and b)  $z/R = 14$ .

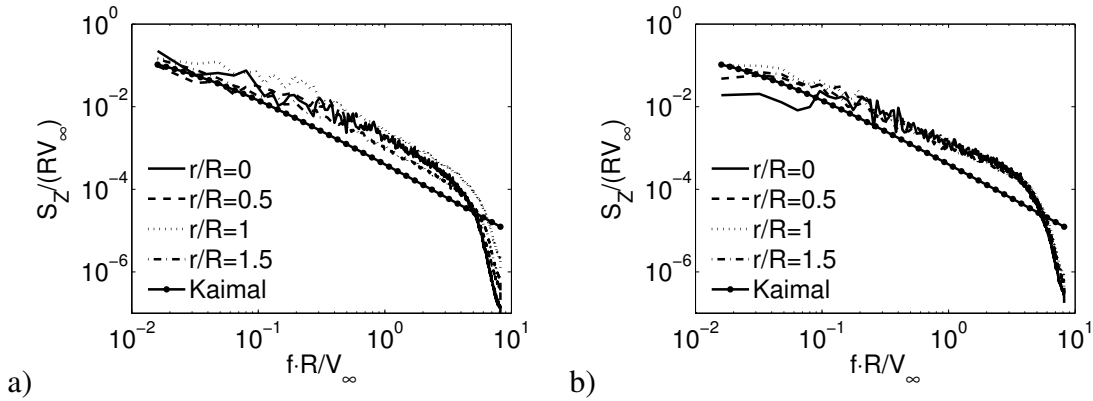


Figure 9.6: Spectra of the axial velocity in the wake of the NM80 turbine at a)  $z/R = 6$  and b)  $z/R = 14$ .

In all cases the shape of the spectra inside the wake is similar to the Kaimal spectrum, though, as expected, the energy level in the wake is, due to the turbulent mixing of the wind turbine, higher at the upper frequency range. Comparing spectra, associated with the various radial positions it is characteristic that the turbulence has the largest energy content in the regions of highest velocity gradients cf. figure 9.2 and 9.3. Furthermore, it appears that the wake turbulence attenuates and tends to become more spatially homogeneous with increasing downstream position. Finally, it is noted that none of the spectra show sign of organized structures at distinct frequencies.

## 9.6 Characteristic length scales

Figure 9.7 presents the radial and downstream development of respectively the estimated standard deviations and the Kaimal length scale of each velocity component in the wake of the

Tjæreborg turbine. The corresponding results for the NM80 turbine are similar and hence are not shown.

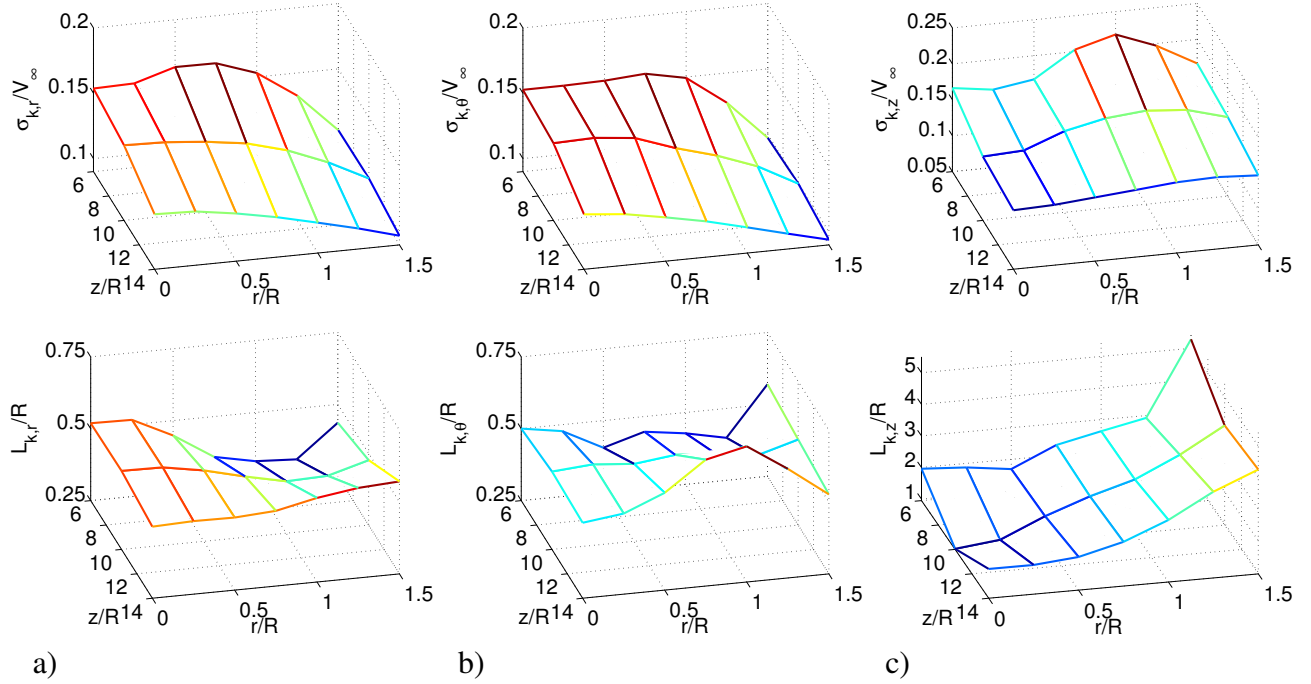


Figure 9.7: Downstream development of respectively the estimated standard deviations (top figures) and length scales (bottom figures) in the wake of the Tjæreborg turbine; a) Radial component; b) Tangential component; c) Axial component

The estimated standard deviations reveal the same features as already presented in figure 9.2 i.e. that the wake generated turbulence has the largest energy level in the regions of largest gradients and that the turbulence attenuates and tend to become more spatial homogeneous with downstream position.

The radial and tangential length scales show modest variations without a clear trend, whereas the axial length scale clearly is increasing with radial position. From the figure the wake is clearly identified as the region of reduced axial length scales compared to the ambient flow field. Furthermore, it is seen that inside the wake the axial length scale,  $L_{k,z}$  is the dominant component, attaining approximately 2-4 times larger values than the radial and tangential length scales.

## 9.7 Coherence

The coherence properties of the wake turbulence have been studied in terms of the coherence decrement using the approach described and validated in appendix A.

Figure 9.8-9.9 display the circumferentially averaged coherence decrement,  $C$ , as a function of  $r_m$  and  $\phi_m$  in two sections downstream of respectively the Tjæreborg and the NM80 turbine. As seen the coherence decrement in the wake is generally increased substantially compared to the inflow, cf. table 9.1. Furthermore,  $C$  is observed to undergo considerable variations inside

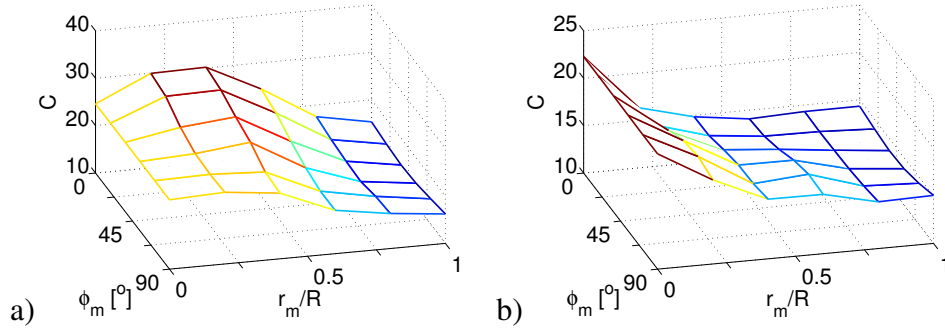


Figure 9.8: Spatial variation of the coherence decrement in the wake of the Tjæreborg turbine; a)  $z/R = 6$ ; b)  $z/R = 14$ .

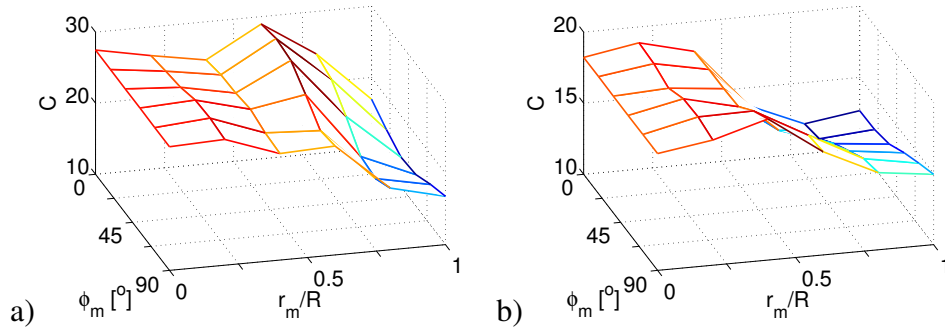


Figure 9.9: Spatial variation of the coherence decrement in the wake of the NM80 turbine; a)  $z/R = 6$ ; b)  $z/R = 14$ .

the wake showing the inhomogeneous nature of the turbulence. Generally, it appears that  $C$  varies most significantly with the radial position, usually attaining the largest values in the inner part of the wake, while it seems less sensitive to changes in  $\phi_m$ . This behavior suggests that the turbulence is least correlated in the center of the wake, which is consistent with the length scales at the same time being smallest here as revealed in figure 9.7. Moreover, there is clear tendency for both the variations and the mean level of  $C$  to decay with downstream position presumably toward the level of the inflow.

## 9.8 Large scale dynamics

The Proper Orthogonal Decomposition (POD), described in appendix A, has been applied in order to extract the dominant flow structures of the wake and to analyze some features of the large scale dynamics of the wake. The analysis was carried out for both turbines but in the following the main focus will be on the results obtained for the Tjæreborg turbine and thus unless otherwise stated this is the turbine used in the present investigation. The analysis was based on a dataset consisting of  $N = 709$  snapshots of the three velocity components taken in different planes downstream of the turbine. The snapshots were in all cases sampled at a rate corresponding to 5.3 times the rotational frequency of the turbine.

In the following representative results from the analysis will be presented.

Figure 9.10, shows the relative energy of the first 25 POD modes compared to the total energy



of the dataset.

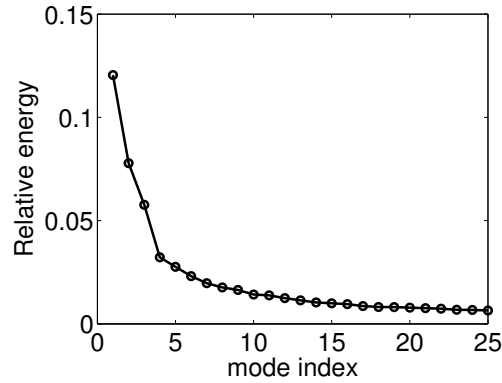


Figure 9.10: Relative energy of the first 25 POD modes in the wake of the Tjæreborg turbine.

The curve decays rapidly in the beginning but becomes less steep with increasing mode number. Note that the first modes, containing the most energy, represent the dominant structures of the wake, while the lower energy levels indicate smaller flow structures.

Figure 9.11 show the velocity field associated with respectively POD mode 1, 2, 4 and 8. These modes represent 12%, 7.8%, 3.2% and 1.8% of the total turbulent energy, respectively. Note that the view is from downwind, i.e. the azimuth position corresponding to  $0^\circ$  is to the right in the plots.

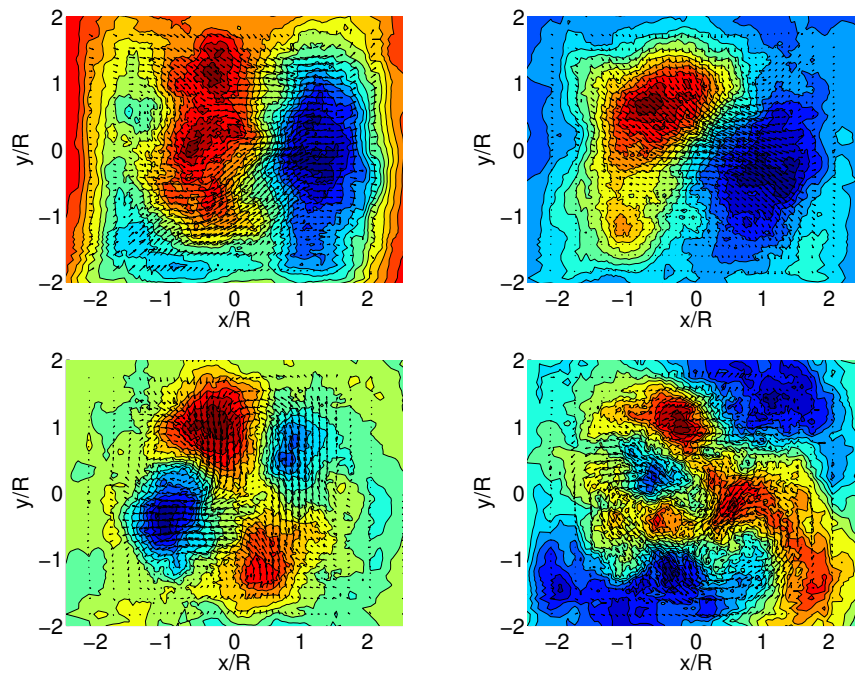


Figure 9.11: From left to right: POD modes 1, 2, 4 and 8 in the wake of the Tjæreborg turbine.

The first two modes are characterized by large regions with significant out-of-plane motion, which roughly divides them into two regions of opposite sign whereas no common trend is observed for the in-plane motion. It should be mentioned that the POD coefficients associated

with the shown modes are alternating between positive and negative values and hence the sign of the out-of-plane motion is not constant. Thus for the shown downstream position the POD analysis reveals significant large scale oscillations, which may be interpreted as a meandering of the wake. For increasing mode number the size of the coherent structures decrease and the level of detail in each mode increase.

To evaluate the dynamics of the wake the POD coefficients associated with each mode have been computed and their temporal behavior was compared to the corresponding coefficients for the inflow. For the POD analysis of the inflow turbulence field a dataset consisting of 1024 snapshots was extracted at a rate corresponding to 7.1 times per rotor revolution.

In Figure 9.12 the fluctuating part of the first mode of respectively the inflow and the wake is plotted as a function of time. It should be noted, that due to the spatial displacement between the input turbulence plane and the investigated wake section the two signals of the modes are not in phase and therefore, for clarity, the shown time signal of the wake mode has been phase-shifted to fit the signal of the inflow mode.

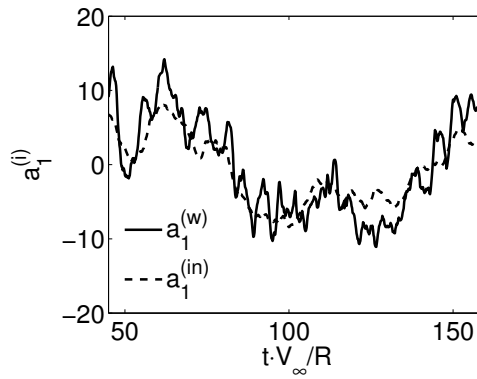


Figure 9.12: Temporal variation of the first mode of respectively the wake and the inflow. The signal of the wake mode has been phase-shifted to fit the signal of the inflow mode.

As seen there is a high degree of correlation between the two modes revealing that the large scale dynamics of the wake is strongly governed by the large scale lateral and vertical velocity components of the ambient turbulence.

To elaborate more on this observation the correlation between each mode of the wake and the corresponding mode of the inflow was studied in terms of the correlation coefficient

$$\rho_{i,i} = \frac{\langle a_i^{(w)}(t + t_0) a_i^{(in)}(t) \rangle}{\left[ \langle a_i^{(w)}(t)^2 \rangle \langle a_i^{(in)}(t)^2 \rangle \right]^{1/2}} \quad (9.2)$$

Here,  $\langle \rangle$  denote ensemble averaging,  $t_0$  is the phase-shift giving the optimal correlation between the  $i$ 'th mode of the inflow and the  $i$ 'th mode of the wake while the superscripts  $w$  and  $in$  refers to respectively wake and inflow modes.

In figure 9.13 the correlation coefficient is plotted as a function of mode number. The figure clearly shows how the most energetic modes of the wake are correlated with the corresponding modes of the inflow and that the correlation coefficient, as expected, is decreasing for increasing mode number.

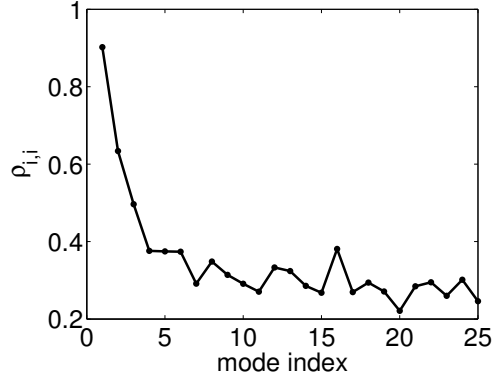


Figure 9.13: Correlation coefficient between respective modes of the wake and the inflow.

As described in appendix A, the original flow field can be reconstructed from the POD modes and their corresponding coefficients using equation A.23. Having accepted that the most energetic modes of the wake are due to the meandering of the wake the reconstructed velocity field may be divided into three parts

$$\begin{aligned} V_{rec}(\mathbf{x}, t^{(n)}) &= \mathbf{v}^{(1)}(\mathbf{x}, t^{(n)}) + \mathbf{v}^{(2)}(\mathbf{x}, t^{(n)}) + \langle \mathbf{V}(\mathbf{x}) \rangle \\ &= \sum_{i=1}^{i_0} a_i^{(n)} \phi(\mathbf{x}) + \sum_{i=i_0+1}^m a_i^{(n)} \phi(\mathbf{x}) + \frac{1}{N} \sum_{j=1}^N \mathbf{V}_j \end{aligned} \quad (9.3)$$

where the first term,  $\mathbf{v}^{(1)}(\mathbf{x}, t^{(n)})$ , represents the large scale wake meandering, the second term,  $\mathbf{v}^{(2)}(\mathbf{x}, t^{(n)})$ , represents the turbulence field in the meandering frame of reference and the last term is the mean velocity field.

From figure 9.13 it is seen that there is a significant correlation between the first three modes of the inflow and the wake and hence  $i_0$  was set to  $i_0 = 3$ .

Initially, the velocity field was reconstructed without including the term  $\mathbf{v}^{(2)}(\mathbf{x}, t^{(n)})$  in order to get a representation of the wake meandering. From this low dimensional field a wake center was computed from the axial induction factor  $a_z^{(1)} = 1 - (\langle V_z \rangle + v_z^{(1)})/V_\infty$  using an approach similar to that presented in chapter 6, i.e.

$$\mathbf{R}_c(z, t) = (x_c(z, t), y_c(z, t)) = \frac{\sum_i |a_z^{(1)}(x_i, y_i, z, t)| \mathbf{r}_i}{\sum_i |a_z(x_i, y_i, z, t)|}, \quad \mathbf{r}_i = (x_i, y_i) \quad (9.4)$$

where the summation is carried out over all grid cell at the given downstream position.

It should be appreciated that the wake center coordinates predicted from equation 9.4, as expected, are nearly identical to the predictions of equation 6.3 where the small scale turbulence is not neglected.

Figure 9.14 shows the temporal variation of the coordinates of the wake center at a section located 10 rotor radii downstream of the Tjæreborg turbine. As seen the variability of the x-coordinate is larger than the y-coordinate, which is in agreement with the turbulent scales of the atmosphere being larger in the horizontal direction than in the vertical direction.

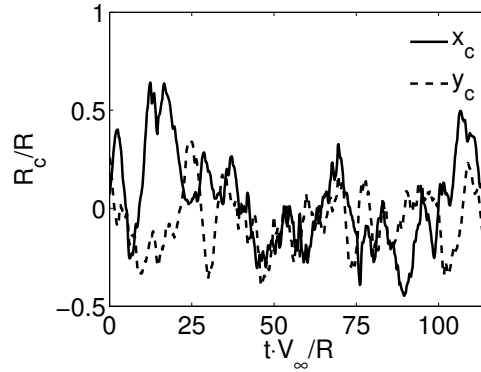


Figure 9.14: Temporal variation of wake center coordinates in a section located  $10R$  downstream of the Tjæreborg turbine

Figure 9.15 shows the ensemble averaged axial velocity profile computed around the dynamic wake center in a section located 10 rotor radii downstream of the rotor and the result is compared to the corresponding profile in the fixed frame of reference. Both profiles have been averaged in the circumferential direction.

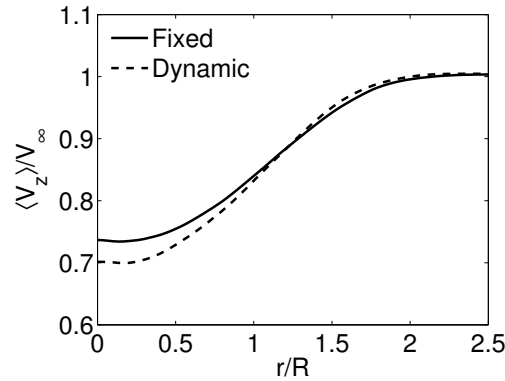


Figure 9.15: Comparison of time and circumferentially averaged axial velocity profile in a fixed and a meandering frame of reference.

As seen the mean velocity profile in the moving frame of reference is characterized by a deeper deficit and a smaller radial extent compared to the profile computed in the fixed frame. The nearly bell shaped velocity profile obtained in the moving frame of reference is indicative of a turbulence field governed by small scale turbulence.

Secondly, the velocity field  $\mathbf{v}^{(2)}(\mathbf{x}, t^{(n)})$  was studied in order to characterize the turbulence described in a meandering frame of reference.

The radial distribution of the azimuthally averaged components of the Reynolds stress tensor in the meandering frame of reference has been computed and as representative examples figure 9.16 shows the result obtained 10 rotor radii downstream of both the Tjæreborg and the NM80 turbine. The result for the other downstream positions show similar behavior and hence are not shown here. Comparing the shown distributions with figure 9.2 it is evident that the behavior of the turbulence is much closer to being isotropic in the meandering frame of reference than in the fixed frame of reference. This is an important observation and reveals that the main source of the anisotropy in the wake is due to the nature of the ambient turbulence field.

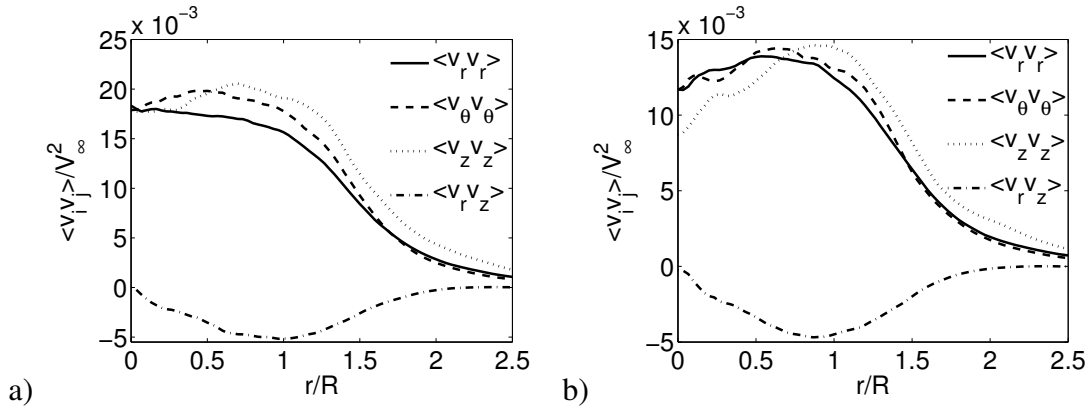


Figure 9.16: Components of the Reynolds stress tensor computed in a meandering frame of reference; a) Tjæreborg; b) NM80

In figure 9.17, the radial and downstream development of the estimated Kaimal length scales of the turbulence in the meandering frame of reference is presented.

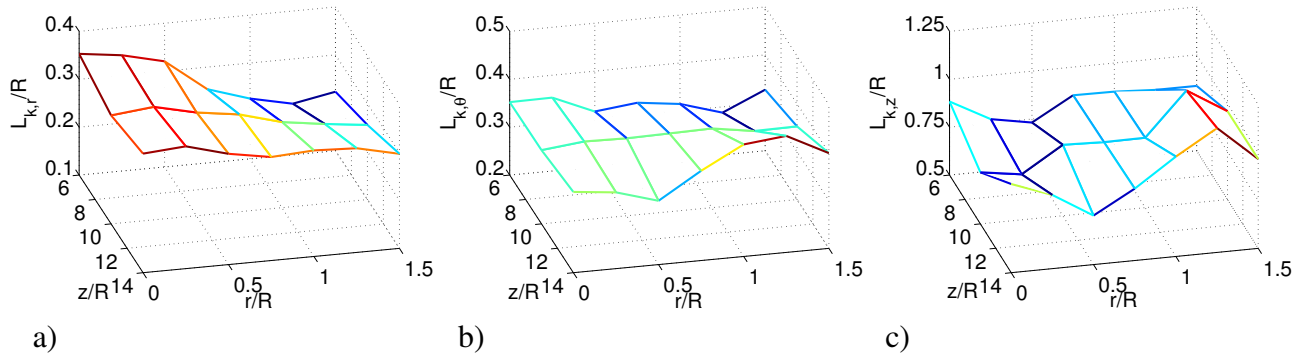


Figure 9.17: Radial and downstream development of the Kaimal length scales in the meandering frame of reference; a) Radial component; b) Tangential component; c) Axial component

The surface plots clearly reveal that the turbulence in the meandering frame of reference is characterized by smaller length scales than those found in the fixed frame of reference. Moreover, it is observed that even though the axial length scale still is larger than the two other components the difference between them is now much smaller.

Finally figure 9.18 display the downstream development of the coherence decrement in the moving frame of reference.

From the figure it is seen that compared to the turbulence expressed in a fixed frame the coherence decrement is generally undergoing more moderate variations. Another interesting observation is that the overall level of the coherence decrement of the turbulence in the meandering frame of reference, in contrast to the length scales, is fairly unaltered compared to the coherence decrement in the fixed frame.

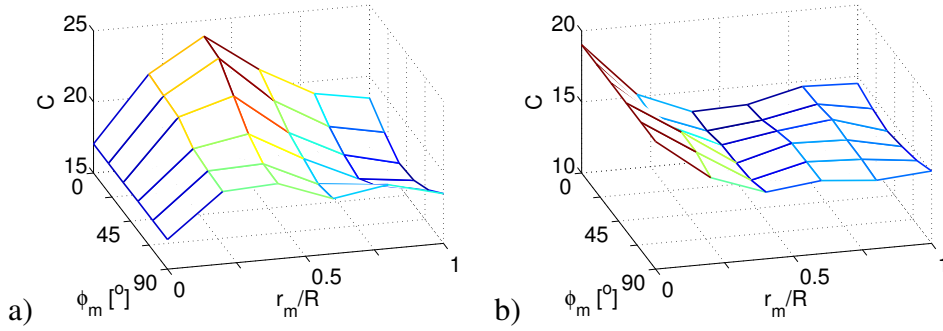


Figure 9.18: Spatial variation of  $C$  in the meandering frame of reference; a)  $z/R = 6$ ; b)  $z/R = 14$

## 9.9 Summary

A thorough study of the turbulence properties of the wake of respectively the Tjæreborg and the NM80 turbine operating in a turbulent non-sheared flow have been presented.

The chapter initially showed some general features of wind turbine wakes including the development of the Reynolds stresses, turbulent length scales, spectral contents and coherence. This investigation revealed an inhomogeneous and anisotropic wake characterized by having considerably smaller length scales than the ambient flow field.

Furthermore, it was shown that the axial velocity in the wake can be considered self-similar about 7 – 8 rotor radii downstream of the rotor.

Secondly, a POD analysis was conducted in order to study the large scale dynamics of the wake. By studying the temporal variation of the most energetic POD modes it was clearly shown that the large scale dynamics of the wake correlates significantly with the large scale motions of the ambient turbulence field.

The results from the POD analysis was subsequently used to reconstruct the original turbulence flow field and divide it into two parts: one representing the large scale meandering and one representing the turbulence in the meandering frame of reference. From the first part a wake center was computed and its temporal evolution was studied. From this analysis it was found that the wake undergoes significant meandering. Thereafter, the mean axial velocity deficit in the meandering frame of reference was computed and found to be deeper and narrower than the corresponding deficit in the fixed frame.

The analysis of the second part of the reconstructed turbulence field revealed that the turbulence in the meandering frame of reference is characterized by being much more isotropic than in the fixed frame of reference, thereby suggesting that the main source of anisotropy in the wake is the ambient turbulence field.

# Chapter 10

## Wind Turbine Wake Aerodynamics in Atmospheric Sheared and Turbulent Inflow

The wake of the Tjæreborg turbine operating in an atmospheric turbulent inflow with a standard mean shear is studied. The numerical setup of the simulation used for the investigation is in every aspect identical to the one used in chapter 7 except that a turbulence field with characteristics given in table 9.1 is now added to the inflow. Hence the mean inflow velocity at hub height is  $V_\infty = 10 \text{ m/s}$  and the power law exponent is  $\alpha = 0.2$ .

The objective is to document the overall development of the wake and to study how the turbulence characteristics of the wake is affected by the combined effect of wind shear and inflow turbulence.

### 10.1 Overall wake characteristics

As in the previous chapters a qualitative impression of the flow field is initially given by showing contours of the instantaneous absolute vorticity in a vertical section along the wind turbine center axis.

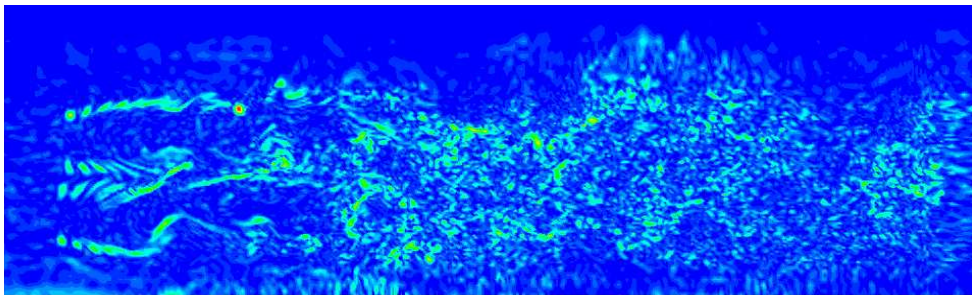


*Figure 10.1: Vorticity contours of the first 15 rotor radii of the wake. Regions of high vorticity appear as light colors. The rotor is located to the left.*

Comparing with the corresponding development where the inflow is laminar (figure 7.6) it is evident that the wake in the present case breaks up much closer to the rotor, as expected. The inflow shear is apparent by the larger pitch of the tip vortices in the top position than in

the bottom position. Otherwise, by comparing with figure 8.3, it appears that the flow field has many similarities to the corresponding non-sheared case.

In order to give an impression of the full three-dimensional behavior of the wake figure 10.2 shows the development of the mean velocity field at different downstream positions. The view is from downwind, i.e. the azimuth angle  $\theta = 0^\circ$  is to the right in the plots.

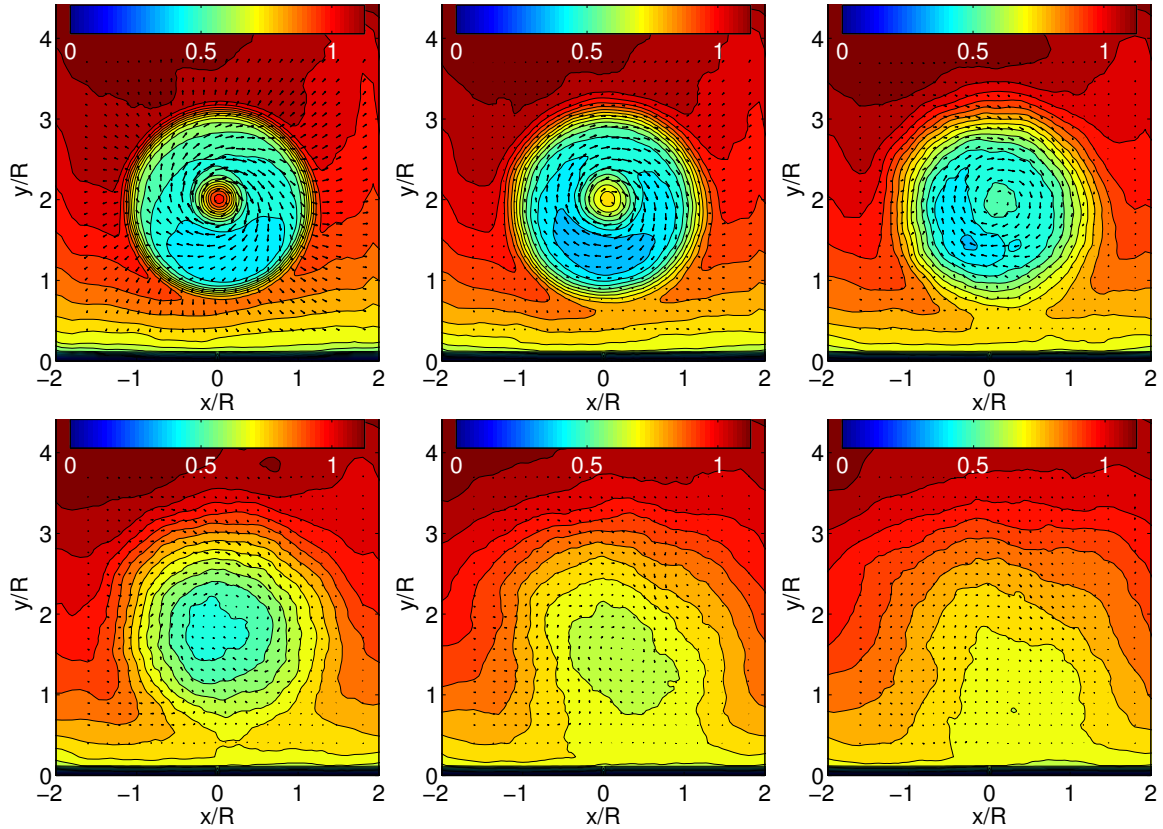


Figure 10.2: Contours of the mean axial velocity field in the wake. The view is from downwind and the mean in-plane velocity is presented as vectors. From left to right:  $1R$ ,  $2R$ ,  $4R$ ,  $6R$ ,  $10R$  and  $14R$  downstream of the turbine.

The figure reveals many of the same features as was observed in the corresponding laminar inflow case (chapter 7), the most apparent being that the rotation of the wake creates a horizontal asymmetry of the velocity deficit. However, as the wake breaks up into small scale turbulence, it appears that the mean rotational speed goes toward zero and thus the horizontal asymmetry gradually diminishes.

Figure 10.3 presents the downstream development of the mean axial velocity in a vertical plane going through the rotor center axis ( $x/R = 0$ ) and the result is compared with the corresponding development in the laminar inflow case. Also included in the figure is the mean inlet velocity profile in order to provide an impression of the induction.

Similarly to what was observed for a non-sheared turbulent inflow (chapter 8) the induction on the rotor itself is more or less unchanged but the ambient turbulence field causes the wake to undergo a more rapid transition into a bell shaped form than when the inflow is laminar. Furthermore, it appears that the maximum deficit is located slightly above the wind turbine center axes, which is a reminiscent from the near wake, where the induction is largest in the upper part of the wake.



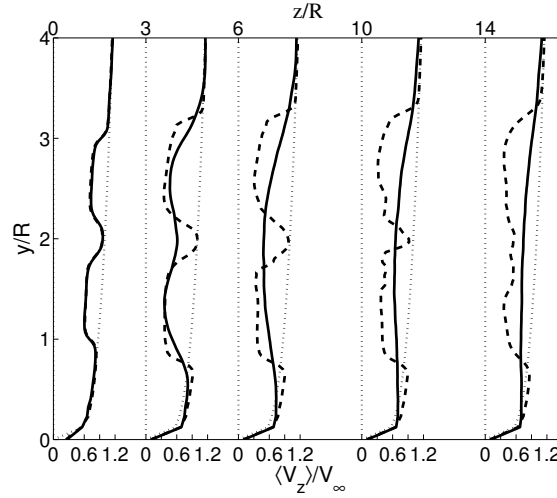


Figure 10.3: Downstream development of the averaged axial velocity in the wake of the Tjæreborg turbine operating in respectively a turbulent (full line) and a laminar inflow (dashed line) with a mean shear.

## 10.2 Self-similarity

In chapter 6 and 9 it was shown that the axial velocity in the far wake of a turbine operating in uniform mean flow is self-similar and may be fairly well described by a constant eddy viscosity solution (equation A.27). However, it is not obvious that the property of self-similarity also is true when the wake development is influenced by the presence of the ground and the velocity shear. Therefore, it is of interest to study whether the far wake in the present case can be considered self-similar.

Due to the sheared inflow the wake is not rotationally symmetric and therefore the scaled velocity variable  $f_v$  defined in equation A.24 will now also be a function of the azimuth position, i.e.

$$f_v(\xi) = \frac{V_0(r, \theta) - \langle V_z(r, \theta, z) \rangle}{V_s(z)}, \quad \xi = r/r_{1/2}(\theta, z) \quad (10.1)$$

Where  $V_0$  is the mean inflow velocity, which as mentioned in the beginning of the chapter is defined by a power law profile, with  $V_\infty = 10 \text{ m/s}$  and  $\alpha = 0.2$

$$V_0(r, \theta) = V_\infty \left( \frac{y}{H} \right)^\alpha = V_\infty \left( \frac{r \sin \theta + H}{H} \right)^\alpha \quad (10.2)$$

The characteristic velocity difference  $V_s$  and the wake half width,  $r_{1/2}$  is defined as in the axisymmetric case (equation A.25 and A.26) except that  $r_{1/2}$  now also is a function of the azimuth position, i.e.

$$\langle V_z(r_{1/2}, \theta, z) \rangle = V_0(r, \theta) - \frac{1}{2} V_s(z) \quad (10.3)$$

Figure 10.4 shows the self-similar axial velocity profiles at different downstream positions for four distinct azimuth positions as indicated in the figure caption. As seen the scaled velocity profile collapse fairly closely on a single curve in the inner part of the wake, which seems to

suggest self-similarity. However, in the outer part of the wake the scaled velocity becomes more scattered and it appears that the self-similarity condition especially in the lower region ( $\theta = 270^\circ$ ) is not fulfilled. The analytical constant eddy viscosity solution (equation A.27) is as in the uniform inflow cases observed to capture the inner part of the wake fairly well but over predicts in the outer part.

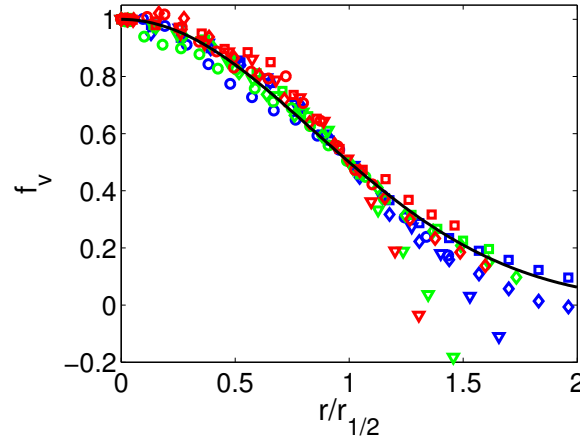


Figure 10.4: Self-similar axial velocity profiles at different azimuth and downstream positions in the wake. Blue:  $z/R = 9$ , Green:  $z/R = 13$ , Red:  $z/R = 15$ . Circles:  $\theta = 0^\circ$ , Squares:  $\theta = 90^\circ$ , Diamonds:  $\theta = 180^\circ$ , Triangles:  $\theta = 270^\circ$ . Solid line constant eddy viscosity solution (equation A.27)

### 10.3 Characteristic length scales

The radial distributions of the Kaimal length scales,  $L_{k,i}$  and the corresponding standard deviations  $\sigma_{k,i}$  of each velocity component have been estimated using the method described in appendix A and the result is shown in figure 10.5 and 10.6 for different downstream and azimuthal positions in the wake. Please note that the shown distributions of  $\sigma_{k,i}$  may be interpreted indirectly as measures of the normal stresses in the wake.

Similarly to what was observed in the sheared non-turbulent inflow case there are considerable azimuth variations of the estimated standard deviations in the wake with the largest values occurring in the upper part of the wake. However, by comparing with figure 7.11-7.13 it appears that the difference between the estimated standard deviations at  $0^\circ$  and  $180^\circ$  is smaller in the present case than when the inflow is laminar.

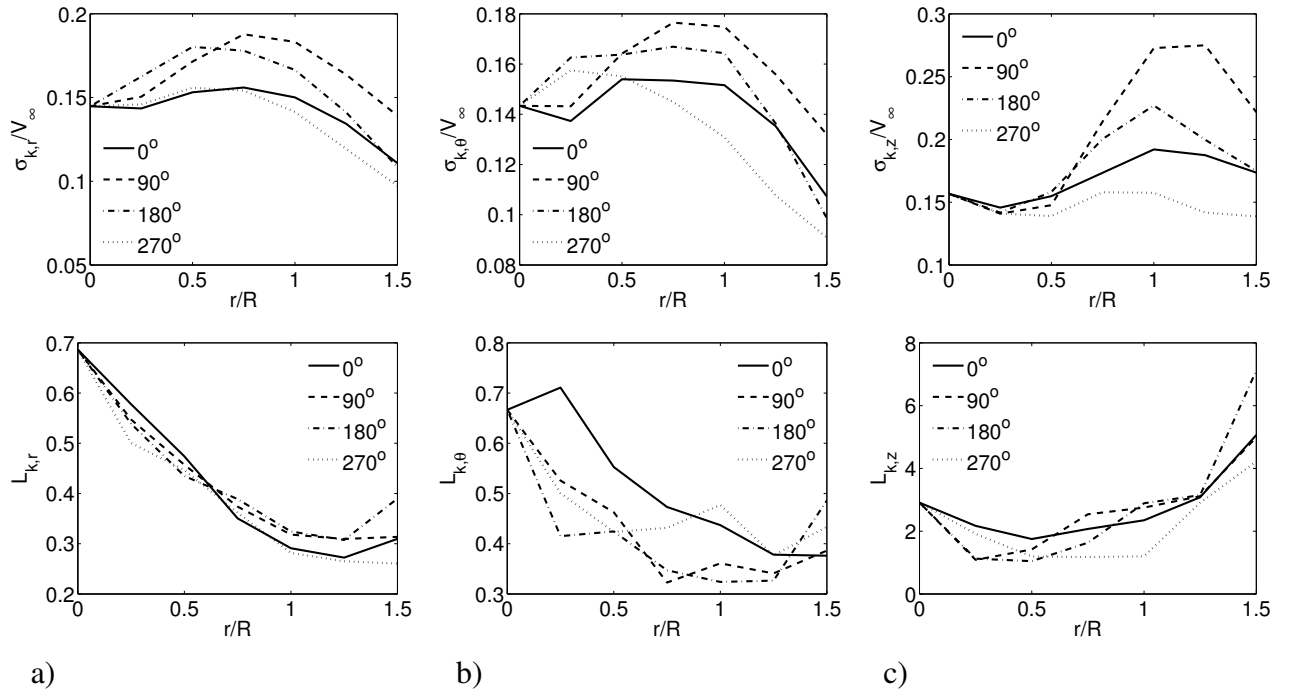


Figure 10.5: Estimated standard deviations (top figures) and Kaimal length scales (bottom figures) in a section located  $6R$  downstream of the Tjæreborg turbine; a) Radial component; b) Tangential component; c) Axial component

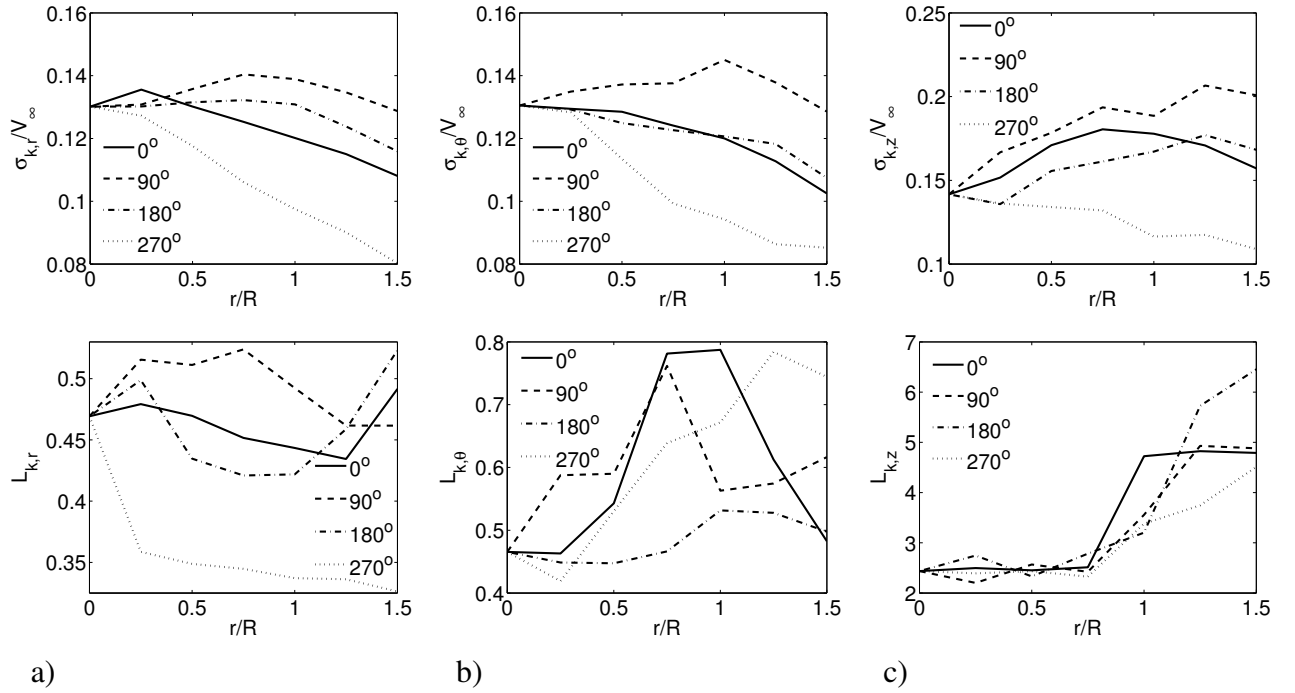


Figure 10.6: Estimated standard deviations (top figures) and Kaimal length scales (bottom figures) in a section located  $14R$  downstream of the Tjæreborg turbine; a) Radial component; b) Tangential component; c) Axial component

The distributions of  $L_{k,i}$  in the wake have many similarities to the non-sheared turbulent inflow case (figure 9.7): The axial length scales is clearly smallest in the interior of the wake and tend to increase with increasing radial position. Furthermore, the radial and tangential length scales are generally smaller than the axial length scales and are undergoing variations without a clear trend.

Even though the azimuthal variation of  $L_{k,i}$  is less pronounced than that of the standard deviations, it is clear that the turbulent length scales typically are smallest in the lower part of the wake.

## 10.4 Coherence

In figure 10.7 and 10.8 the spatial variation of the coherence decrement,  $C$ , defined from equation A.17, is displayed for two different downstream positions at azimuth angles of respectively  $0^\circ$ ,  $90^\circ$ ,  $180^\circ$  and  $270^\circ$ . Note that as the flow field is no more rotationally symmetric results are presented for the angle  $\phi_m$  in the range  $[0^\circ; 180^\circ]$ .

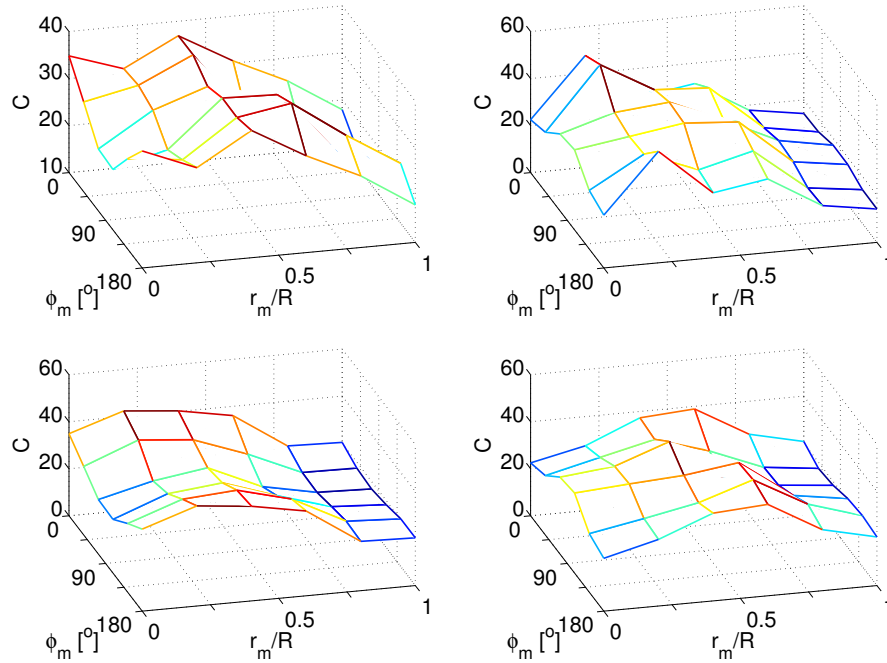


Figure 10.7: Spatial variation of the coherence decrement  $6R$  downstream of the Tjæreborg turbine operating in a sheared and turbulent inflow. From left to right:  $\theta = 0^\circ$ ,  $\theta = 90^\circ$ ,  $\theta = 180^\circ$  and  $\theta = 270^\circ$

The figures reveal many of the same features as was observed in the turbulent non-sheared case (figure 9.8-9.9).

The coherence decrement is generally increased considerably compared to the ambient flow field and tends to decrease with downstream position. Furthermore,  $C$  is typically largest in the inner part of the wake and is most sensitive to variations in the radial position. However, in the present case it appears that the angle  $\phi_m$  has greater significance on the coherence decrement than in uniform inflow. In particular it is observed that the coherence decrement in the present

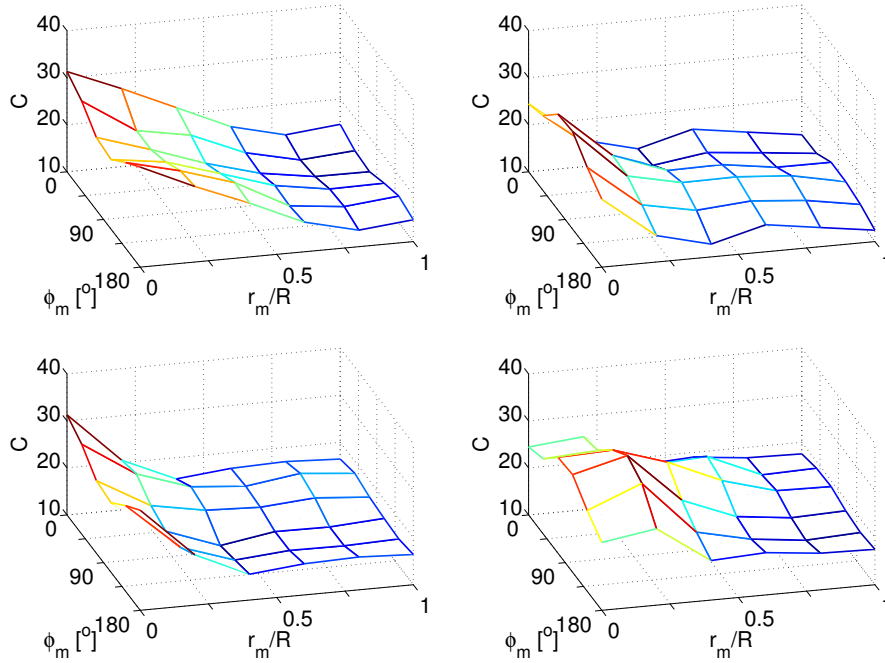


Figure 10.8: Spatial variation of the coherence decrement  $14R$  downstream of the Tjæreborg turbine operating in a sheared and turbulent inflow. From left to right:  $\theta = 0^\circ$ ,  $\theta = 90^\circ$ ,  $\theta = 180^\circ$  and  $\theta = 270^\circ$

case is not constant at  $r_m = 0$  due to the rotational asymmetry caused by the inflow shear. However, it should be noted that the azimuthal variations of the coherence decrement for both tested downstream positions are rather moderate, which suggests limited rotational asymmetry.

## 10.5 Large scale dynamics

In order to elucidate the large scale dynamics of the flow field as well as the turbulence characteristics in the meandering frame of reference a POD analysis has been conducted in a cross-section located  $10$  rotor radii downstream of the rotor. The reason that the present investigation only is carried out for a single downstream position is partly that the axial development was expected to be similar to that observed in the non-sheared case (chapter 9) and partly because the main objective of this section is to study the degree of azimuthal asymmetry of the turbulence properties in the meandering frame of reference. The POD analysis was based on a dataset consisting of  $1158$  snapshots of the velocity field sampled at a rate corresponding to  $5.1$  times the rotational frequency.

An analysis of the POD modes revealed significant correlation between the first  $3$  modes of the wake and the inflow and therefore in analogy to chapter 9 it was deduced that these modes constitute the meandering of the wake, while the remaining higher modes represent the turbulence described in the meandering frame of reference.

Figure 10.9 shows the radial distribution of respectively  $L_{k,i}$  and  $\sigma_{k,i}$  in the meandering frame of reference at azimuth positions of respectively  $0^\circ$ ,  $90^\circ$ ,  $180^\circ$ ,  $270^\circ$ .

As expected the length scales in the meandering frame of reference are generally smaller than those determined in the fixed frame of reference (figure 10.5-10.6) and also their size seems to be closer to each other in agreement with an increasingly isotropic flow. Furthermore, it is observed that the characteristic length scales are rather insensitive to changes in the azimuth positions, but that the axial length scales still varies somewhat with radial position and thus generally maximizes in the outer part of the wake.

The corresponding standard deviations,  $\sigma_{k,i}$  reveal that the turbulence in the meandering frame of reference is much closer to being isotropic and that it can be considered more spatial homogeneous, however there are still some variations in the wake as a function of radial position.

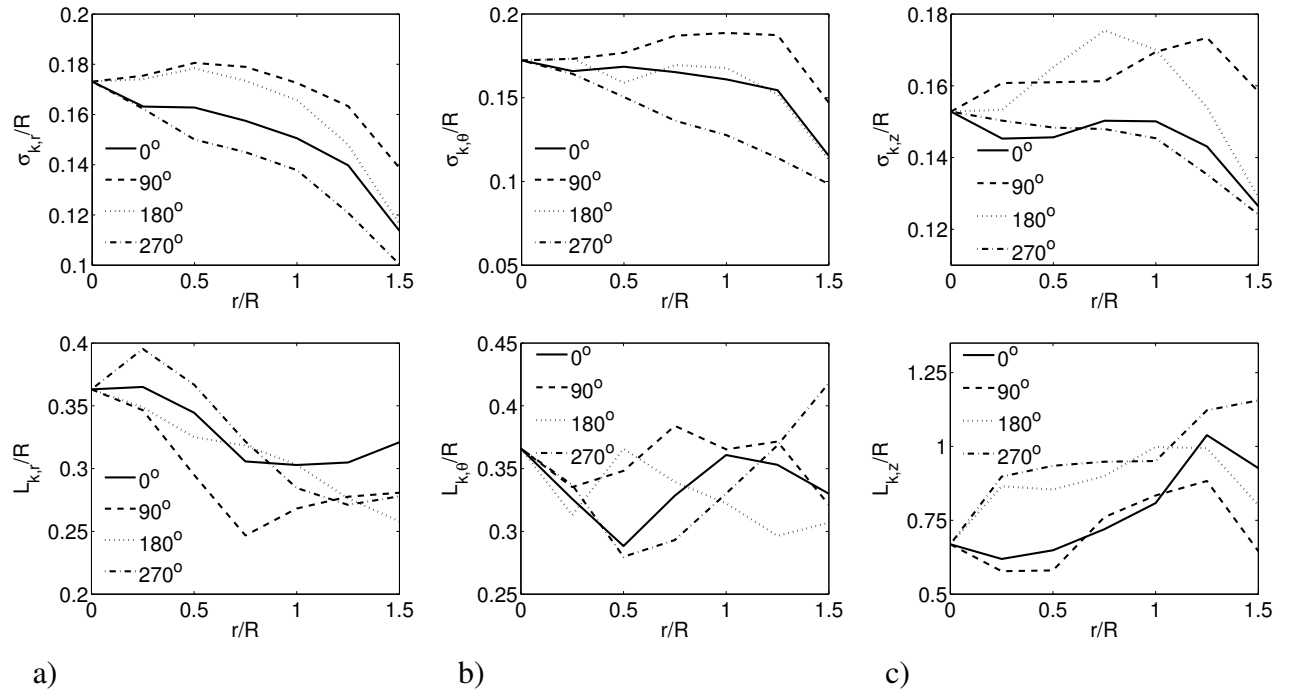


Figure 10.9: Estimated standard deviations (top figures) and Kaimal length scales (bottom figures) in the meandering frame of reference; a) Radial component; b) Tangential component; c) Axial component

Figure 10.10 presents the coherence properties in the meandering frame of reference at different azimuth positions. The variation of the coherence decrement does not show a clear trend but, as expected, it is generally increased compared to the turbulence field described in the fixed frame of reference.

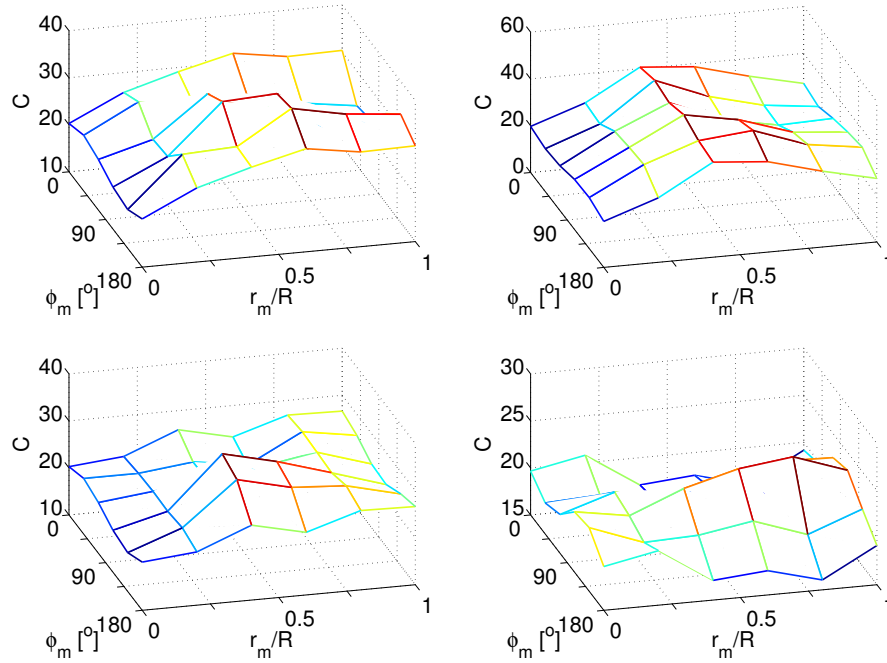


Figure 10.10: Spatial variation of the coherence decrement in the meandering frame of reference. From left to right:  $\theta = 0^\circ$ ,  $\theta = 90^\circ$ ,  $\theta = 180^\circ$  and  $\theta = 270^\circ$

## 10.6 Summary

The wake of the Tjæreborg wind turbine operating in a sheared and turbulent inflow has been studied.

Initially a qualitative description was provided by showing contours of vorticity as well as the mean axial velocity. Besides a vertical skew caused by the inflow shear, the wake was also shown to become horizontally asymmetric due to wake rotation in the same manner as was observed in the corresponding laminar inflow case. However, as the wake broke up and became increasingly turbulent it appeared that the asymmetry gradually diminished.

Secondly, a study showed that the axial velocity could be considered fairly self-similar in the inner part of the wake, whereas this condition generally was not well fulfilled in the outer and especially the lower part of the wake.

Thereafter, the development of the turbulence characteristics was studied in terms of the standard deviations, turbulent length scales and spectral coherence. The turbulence was, as in the wake of a turbine operating in a non-sheared turbulent inflow, shown to be inhomogeneous, anisotropic and characterized by having smaller length scales than the ambient flow field. It was, however, shown that both the length scales and the coherence properties varied rather moderately with azimuth position, which suggested limited rotational asymmetry of these quantities. Finally, a POD analysis was carried out in a section located 10 rotor radii downstream of the rotor and the results were used to reconstruct the velocity field without including the 3 most energetic modes, thereby obtaining a representation of the turbulence in a meandering frame of reference. A subsequent analysis showed that the standard deviations of the turbulence in the meandering frame of reference exhibited much more isotropic behavior than the corresponding field in a fixed frame of reference.

# Chapter 11

## Wake Interaction between a Row of 3 Turbines

The wakes of 3 Tjæreborg wind turbines placed in a row is simulated in a case where the wind is in line with their common axis. The mutual distance between the rotors is 5 diameters and they are operating in a uniform mean free-stream velocity of  $V_\infty = 10 \text{ m/s}$ . Simulations are carried out both for laminar and turbulent inflow conditions and the results are compared with the aim of studying the influence of the ambient turbulence on the wake behavior. The characteristics of the imposed turbulent inflow are given in table 9.1.

### 11.1 Mesh configuration

The computations were carried out in a Cartesian computational domain as sketched in figure 2.5a and 2.5c. The dimensions of the grid was  $(L_x, L_y, L_z) = (18R, 18R, 35.3R)$ , where the  $z$ -coordinate is in the flow direction.

The actuator lines were rotating in the  $z$ -plane and their point of rotation was in the center of the domain. The most upstream rotor was located 7 rotor radii downstream of the inlet and the other two rotors were positioned respectively 10 and 20 rotor radii further downstream.

The height and width of the near domain was  $2.6R$  and it extended from  $1.3R$  upstream of the first turbine to  $3R$  downstream of the third turbine.

The grid was divided into 48 blocks (2 in the  $x$  and  $y$  direction respectively and 12 in the  $z$ -direction) with 64 grid points in each direction. Thus, the used mesh contained  $128 \times 128 \times 768$  grid cells corresponding to a total of approximately  $12.6 \cdot 10^6$ .

### 11.2 Qualitative wake characteristics

Figure 11.1 depicts iso-vorticity contours in a cross-section along the common axis of the rotors. When the incoming wind is laminar the wake behind the upstream turbine is seen to be dominated by organized tip and root vortices, whereas the flow undergoes massive separation over the second rotor, causing the most downstream rotor to operate in a completely separated flow. It should be mentioned that the highly separated flow partly is a result of the rotors being forced to operate at the same rotational speed, whereby the tip speed ratio and thus also the drag becomes very high for the downstream rotors.



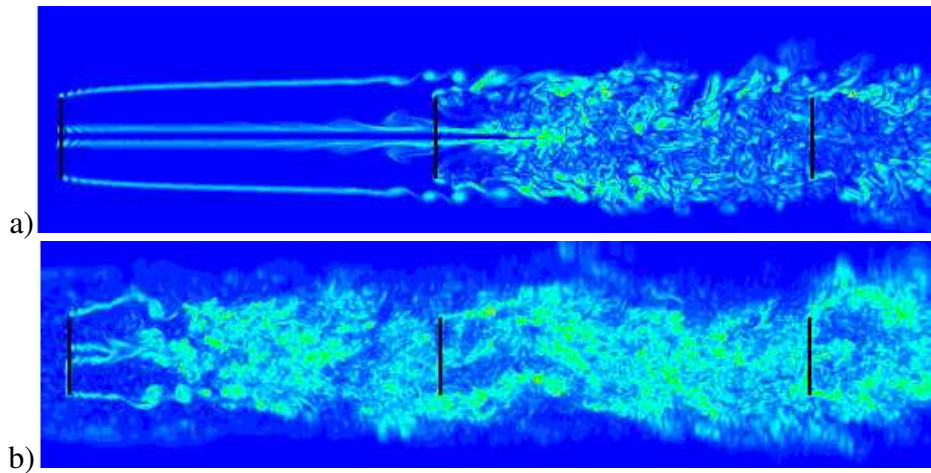


Figure 11.1: Visualization of flow field between the rotors using vorticity contours. Regions of high vorticity appear as light colors. The rotors are indicated as black lines; a) Laminar inflow b) Turbulent inflow

When ambient turbulence is introduced to the inflow the wake characteristics are significantly altered especially behind the first and second turbine. The ambient turbulent fluctuations perturb the vortex system generated by the upstream turbine, whereby the wake breaks up and as a consequence the second rotor then operates in a flow characterized by broad band turbulence. Although, the influence of the two downstream rotors on the wake immediately downstream is visible it is clear that the flow field is fully turbulent. Furthermore, it is seen that the ambient turbulence field causes a large scale wake meandering, which is significantly larger than the diameter of the rotors.

### 11.3 Mean Wake Characteristics

Figure 11.2 compares the azimuthally and time averaged profiles of the axial velocity in the wake of the three rotors with and without ambient turbulence included.

In the laminar inflow case the profiles in the wake of the first turbine are nearly constant over most of the radial distance, which as mentioned in chapter 4, is indicative of a wake dominated by the induction of distinct tip vortices. In the velocity profile obtained at the second rotor the presence of two systems of tip vortices originating from respectively the first and the second turbine is clearly seen, which is consistent with the vorticity contours shown in figure 11.1. In between the second and the third rotor the flow field is observed to undergo a rather rapid transition into a bell shaped profile, indicating that the wake becomes dominated by small scale turbulence. The flow field is redistributed as it passes through the third rotor but the strong unsteady mixing causes the deficit to develop rapidly back to the bell shaped form.

When ambient turbulence is introduced to the inflow the mean velocity profiles in the wake of the first turbine becomes bell shaped prior to impacting the second turbine. This transition into a bell shape form is as mentioned in chapter 8 partly due to the break up of the vortex system and partly due to the large scale meandering of the wake deficit. The unsteady nature of the upstream wake and the accompanied tendency toward recovery of the velocity deficit causes the induction over the second rotor to be reduced compared to that obtained in the laminar inflow case. Furthermore, it is evident from the velocity profiles obtained between the second and third

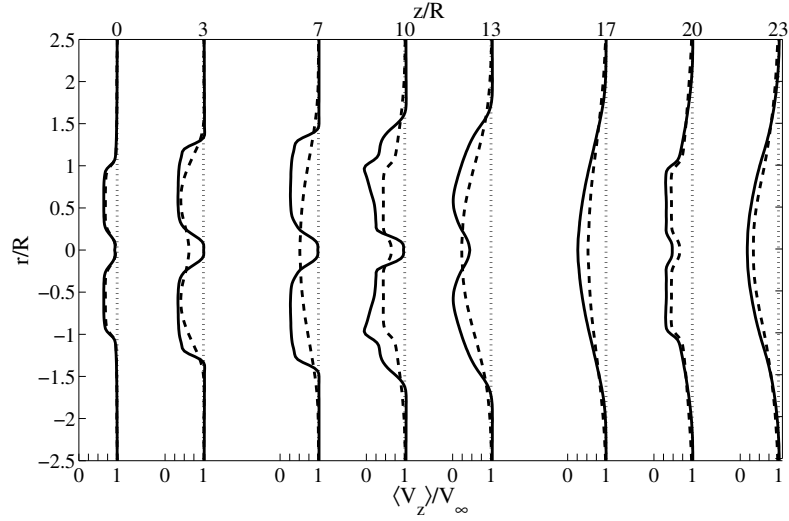


Figure 11.2: Computed profiles of the averaged axial velocity at different downstream positions.

rotor that the development of the wake deficit in this region is stronger when ambient turbulence is included than when the inflow is laminar. In the vicinity of the third rotor and downstream of it the influence of the ambient turbulence field on the mean velocity profiles appear less visible, which suggests that the flow field here is dominated by wake generated turbulence, i.e. turbulence originating from the bound vorticity of the blades and the velocity shear of the wake deficit.

In Figure 11.3 the corresponding downstream development of the tangential velocity profiles are compared.

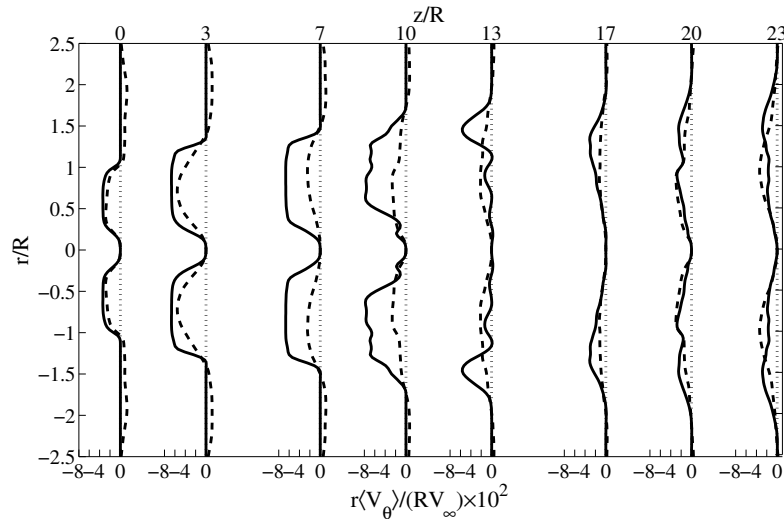


Figure 11.3: Computed profiles of the averaged tangential velocity at different downstream positions.

When the inflow is laminar the profiles of the normalized swirl velocity in the wake of the first turbine remains nearly uniform until impact with the second turbine, whereas the profile decays rapidly toward zero in the turbulent inflow case. In both the tested cases the tangential velocity is rather marginal downstream of the second and the third rotor and thus it can be concluded

that circulation is far from being conserved.

Figure 11.4 and 11.5 present the radial distribution of the four main components of the Reynolds-stress tensor at different positions downstream each turbine. All the shown curves are averaged in the circumferential direction. The two components  $\langle v_r v_\theta \rangle$  and  $\langle v_\theta v_z \rangle$  are, as mentioned in chapter 6, zero due to circumferential symmetry and they are therefore not shown in the figures.

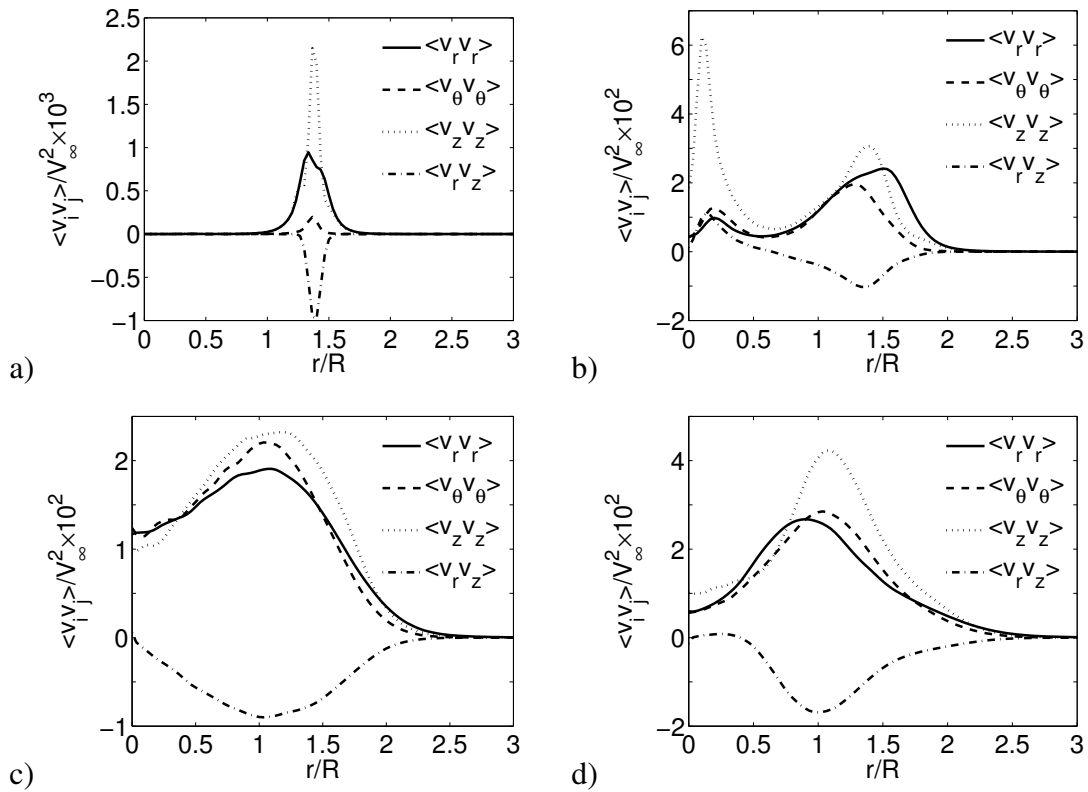


Figure 11.4: Radial distributions of Reynolds stresses at different sections downstream of the first rotor in laminar inflow. The second and third rotor is located respectively 10 and 20 rotor radii downstream. a)  $z/R = 8$ ; b)  $z/R = 12$ ; c)  $z/R = 18$ ; d)  $z/R = 23$

In the laminar inflow case the Reynolds stresses are generally largest in the annular region surrounding the tips indicating that turbulence primarily is generated by the shear from the tip vortices.

In the turbulent inflow case the Reynolds stresses are as expected observed to develop faster toward a bell shaped form. However, also in this case the presence of the tip vortices are clearly seen immediately downstream of the rotors as a local maximum of the Reynolds stresses in the wake periphery. It should be noted that the distributions of the Reynolds stresses downstream of the third rotor are quite similar in the two tested cases, which is consistent with the flow field being dominated by the small scale wake generated turbulence. Furthermore, it is observed that there is a tendency for the wake to become increasingly isotropic, however, in both the tested cases the axial normal stresses are generally larger than the other components.

Finally, similarly to what was observed in chapter 9 in connection with the analysis of an isolated wind turbine, the development of the velocity deficit is much faster than the Reynolds

stresses, which in agreement with several field measurements [10] shows that the turbulence is more persistent than the velocity deficit.

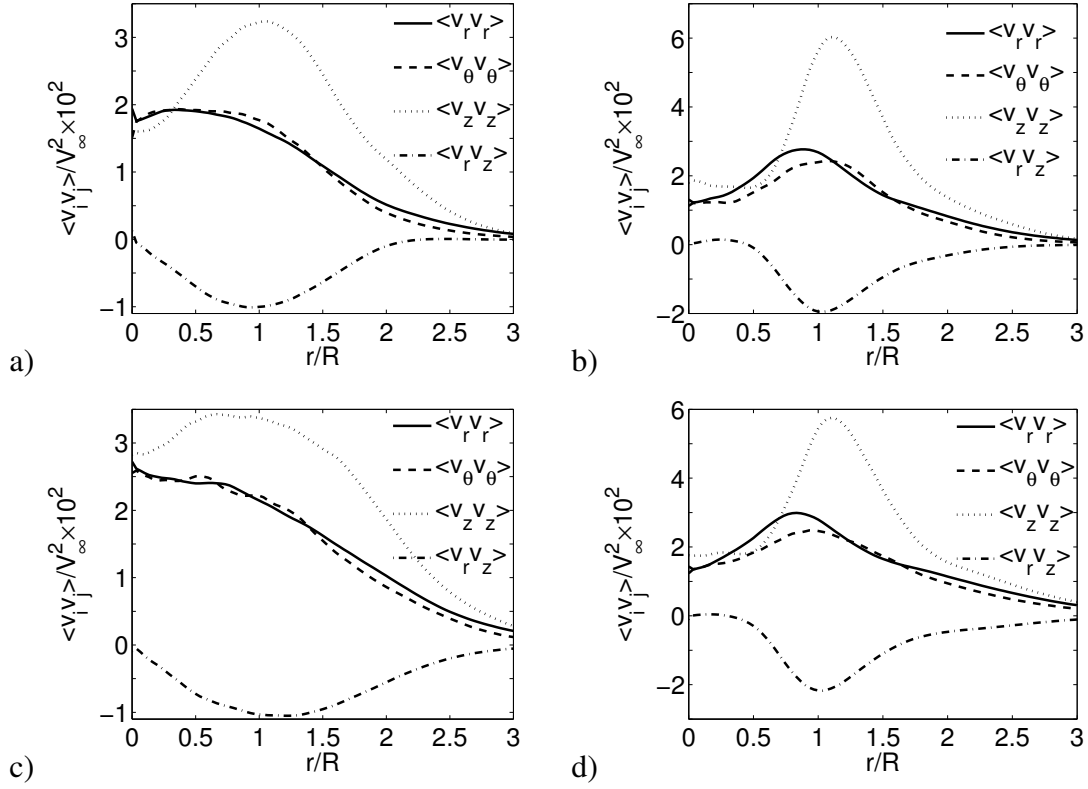


Figure 11.5: Radial distributions of Reynolds stresses at different sections downstream of the first rotor in turbulent inflow. The second and third rotor is located respectively 10 and 20 rotor radii downstream. a)  $z/R = 8$ ; b)  $z/R = 12$ ; c)  $z/R = 18$ ; d)  $z/R = 23$

## 11.4 Rotor loading

In order to quantify the effect of the inflow turbulence on the rotor loading a rainfall count of the yaw moments of each turbine were carried out and the corresponding equivalent moments,  $\hat{M}_y$  were computed assuming a non-dimensional equivalent load frequencies of  $f_0 = f \cdot R/V_\infty = 1$  and a Wöhler exponent of  $m = 6$ .

Figure 11.6 shows the computed equivalent yaw moments along the row of turbines for respectively laminar and turbulent inflow. It should be noted that the corresponding results for Wöhler exponents of 3 and 9 gives more or less the same overall trend as in figure 11.6.

When the inflow is laminar the equivalent yaw moment increases almost linearly along the row, which seems to indicate that some large scale wake meandering takes place.

In the turbulent inflow case the yaw loads on the downstream turbines are, due to the wake meandering, also significantly larger than on the first turbine but here the loading levels out such that the yaw loads on the third turbine is somewhat lower than on the second turbine.

At a first glance it might be surprising that the equivalent yaw moment on the third turbine is

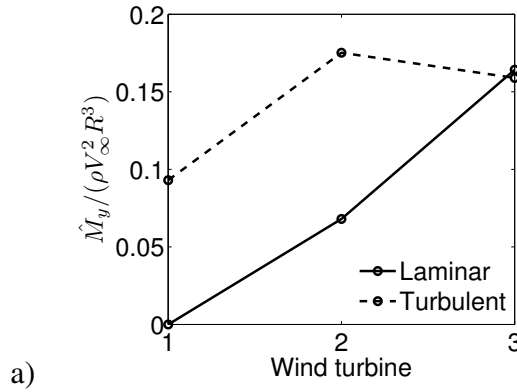


Figure 11.6: Equivalent yaw moments acting on the row of rotors for respectively laminar and turbulent inflow

larger when the inflow is laminar than when it is turbulent since the wake meandering is more significant in the latter than in the former case. An investigation of the wake center coordinates (equation 6.3) in a section located  $2R$  upstream of the third rotor revealed a standard deviation of the  $x$  and  $y$  coordinates of respectively 0.28 and 0.18 in the turbulent inflow case, while the corresponding values in the laminar inflow case only was 0.05 and 0.05. The reason for this apparent contradiction can, however, be explained from figure 11.7 which, for both inflow cases, shows the azimuthally averaged axial velocity profile at the same downstream position.

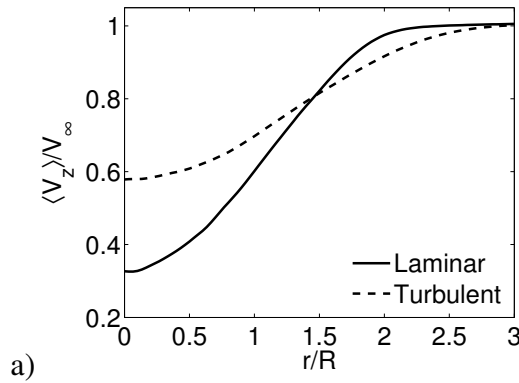


Figure 11.7: Comparison of mean wake deficit computed  $2R$  upstream of the third rotor in respectively laminar and turbulent inflow

As seen the wake deficit encountered by the third turbine is both much deeper and steeper when the inflow is laminar than when it is turbulent and therefore the effect of the large scale wake meandering is felt most severely in the former case.

The above analysis is important since it shows that besides the meandering of the wakes also the shape of the deficit has a significant effect on the yaw loads of downstream turbines.

## 11.5 Summary

A row of three Tjæreborg turbines spaced 5 diameters apart from each other has been simulated in a case where the wind is directed along their common axis. Both laminar and turbulent inflow

conditions were considered.

The simulations revealed that the wake development in the laminar and the turbulent inflow case is very different both in terms of mean velocity and Reynolds stress distributions. The main influence of the ambient turbulence field is to perturb the otherwise stable vortex system generated downstream of the first turbine, whereby the wake becomes unstable and breaks up prior to impacting the second turbine. The break up of the wake and transition into small scale turbulence causes an increased exchange of flow from the exterior, whereby the second rotor experiences higher mean velocities than in the corresponding laminar case.

Moreover, visualization of the wake behavior together with an inspection of the wake center coordinates showed that wake meandering is significant in the turbulent inflow case and less so in laminar inflow. Despite these observations it was found that the equivalent yaw loads on the downstream rotors in laminar inflow was quite large in particular for the third turbine, which experienced higher yaw loads than the corresponding turbine when the inflow was turbulent. The reason for this was argued to be due to the deeper wake deficit when the inflow is laminar.

## Chapter 12

# Wake Interaction between 2 Turbines in Strongly Sheared and Low Turbulent Atmospheric Flow

Two NM80 turbines operating in an atmospheric boundary layer characterized by strong shear and low ambient turbulence are simulated in a case where the downstream turbine operates partly in the wake of the upstream one. The numerical setup of the simulation corresponds to conditions measured during night at the Tjæreborg wind farm site in Denmark as presented in [46]. The results from the present actuator line simulations were used to tune various parameters in the new Dynamic Wake Meandering (DWM) model [43]. The results from the tuned DWM model were later compared to measurements [47] and fair agreement was achieved. Unfortunately, the measurements could not be used for a direct comparison with the actuator line computations because the experimental conditions were complicated by the wake from the upstream turbine for some reason being deflected downwards hence only occurring on the lower part of the downstream rotor [46].

### 12.1 Mesh configuration and numerical setup

The computation was carried out in a Cartesian computational domain as sketched in figure 2.5b and 2.5c. The dimensions of the grid was  $(L_x, L_y, L_z) = (20R, 24R, 28R)$ , where the  $z$ -coordinate is in the flow direction.

The upstream rotor was positioned  $9.5R$  downstream of the inlet and having its point of rotation located  $H = 1.4R$  above ground corresponding to the actual hub height of the NM80 turbine. The second rotor was located  $6.6R$  further downstream and in order to obtain partial wake operation the centers of the two turbines were placed  $1.6R$  apart in the  $x$ -direction. The downstream turbine was furthermore yawed an angle of  $15^\circ$  compared to the mean flow direction.

The height and width of the near domain was  $3.6R$  and it extended from approximately  $1R$  upstream of the first turbine to approximately  $4R$  downstream of the second turbine.

The grid was divided into 72 blocks (3 in the  $x$  and  $y$  direction respectively and 8 in the  $z$ -direction) with 48 grid points in each direction. Thus, the used mesh contained  $144 \times 144 \times 384$  grid points corresponding to a total of approximately  $8.0 \cdot 10^6$  and a resolution in the near domain of 30 grid points per rotor radius.

## 12.2 Atmospheric boundary layer modeling

The mean wind shear of the atmospheric boundary layer was modeled according to a power law profile

$$V_z(y) = \begin{cases} V_\infty \left(\frac{y}{H}\right)^\alpha, & y \leq 8R \\ V_\infty \left(\frac{8R}{H}\right)^\alpha, & y > 8R \end{cases} \quad (12.1)$$

Where the exponent  $\alpha$  was set to 0.75 and the mean velocity in hub height was set to  $V_\infty = 5.75 \text{ m/s}$ . The turbulence intensity of the ambient turbulence field was set to about 3-4%, which, along with the strong shear, is in agreement with stable atmospheric conditions typically experienced at night.

## 12.3 Blade loading

Figure 12.1-12.2 show the azimuth variation of respectively the ensemble averaged normal velocity and its standard deviation at various radial positions along the blade for each wind turbine.

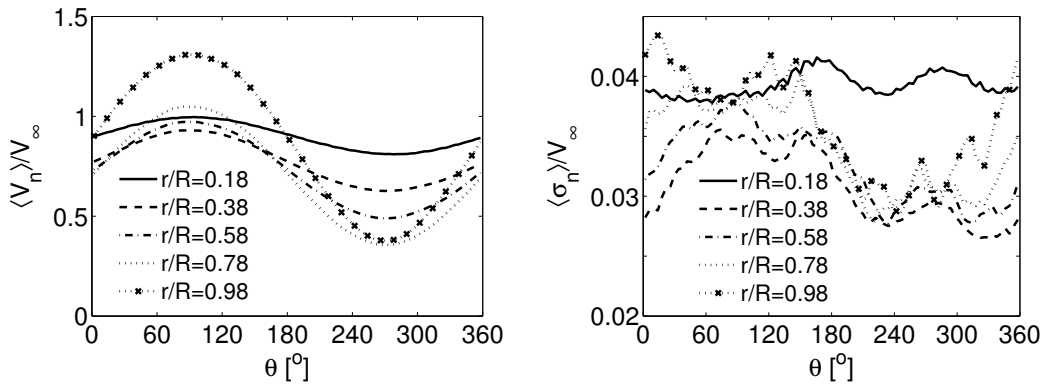


Figure 12.1: Normal velocity and its standard deviation binned on azimuth position for various spanwise stations along the blade of the upstream turbine.

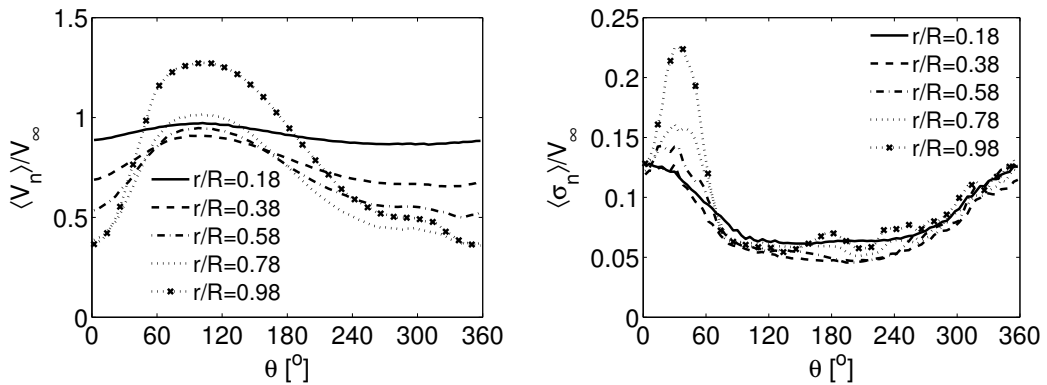


Figure 12.2: Normal velocity and its standard deviation binned on azimuth position for various spanwise stations along the blade of the upstream turbine.



For the upstream turbine the variation appears sinusoidal and the standard deviations are as expected at a level comparable to that of the ambient flow. For the downstream turbine the influence of the wake from the upstream turbine is clearly seen as a substantial increase in the standard deviations and a decrease in the velocities in the azimuth range from  $300^\circ$  to  $60^\circ$ , i.e. the situation corresponds to  $1/3$  wake operation.

In order to illustrate the variation of the blade forces the spanwise distribution of respectively the normal and tangential forces are depicted in figure 12.3-12.4 for four distinct azimuth positions for each turbine.

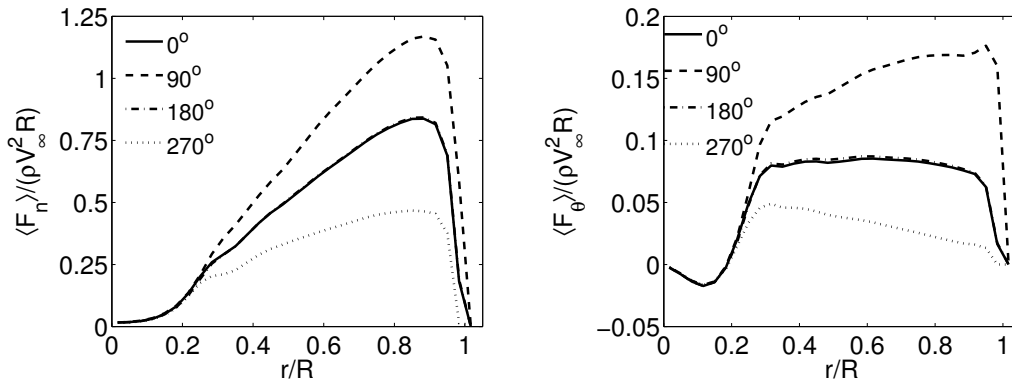


Figure 12.3: Ensemble averaged normal and tangential force along the blade at four azimuth positions for the upstream rotor.

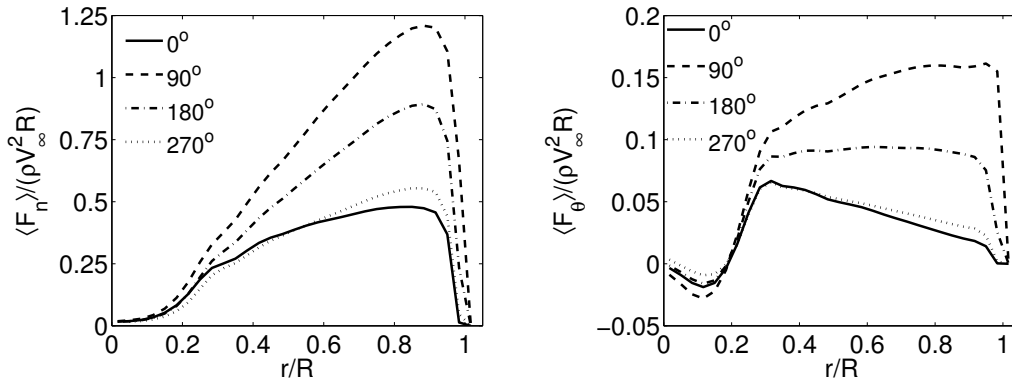


Figure 12.4: Ensemble averaged normal and tangential force along the blade at four azimuth positions for the downstream rotor.

From the figures it is evident that the blade forces vary significantly during a rotor revolution. As expected the loading is generally highest when the blade is oriented vertically upwards ( $90^\circ$ ) and lowest when it is pointing downwards ( $270^\circ$ ). For the upstream rotor the blade loading at the two horizontal positions  $0^\circ$  and  $180^\circ$  is nearly the same hence indicating almost no hysteresis. As mentioned in chapter 7, a CFD study by Zahle and Sørensen [93] on two different wind turbines operating in shear flow showed that this hysteresis, though generally being modest, can be more significant especially at the inner part of the blade where the local reduced frequency of the blade section ( $k = c\omega/(2V_{rel})$ ) is high due to the larger chord and lower relative velocity. The reason that the horizontal asymmetry is not observed to the same degree here could, as

mentioned in chapter 7, be due to a combination of limited grid resolution and use of steady 2D airfoil data in the attached region. However, since the hysteresis for a typical MW wind turbine operating in strong shear flow [93] normally is rather small the limited phase-lag in the actuator line computations was not considered a major issue.

When the blade of the downstream rotor is oriented horizontally at  $0^\circ$  the blade loading is as expected low because the blade in this case is partly immersed in the wake of the upstream rotor. It is evident from figure 12.4 that this rotor besides a large tilt moment also experiences a significant yaw moment.

## 12.4 Wake Characteristics

In figure 12.5 the flow field between the rotors is visualized in terms of respectively the instantaneous contours of the streamwise velocity and the absolute vorticity in a horizontal plane located at hub height. Please note that the view is from above and hence the azimuth angle corresponding to  $0^\circ$  is upwards in the figures.

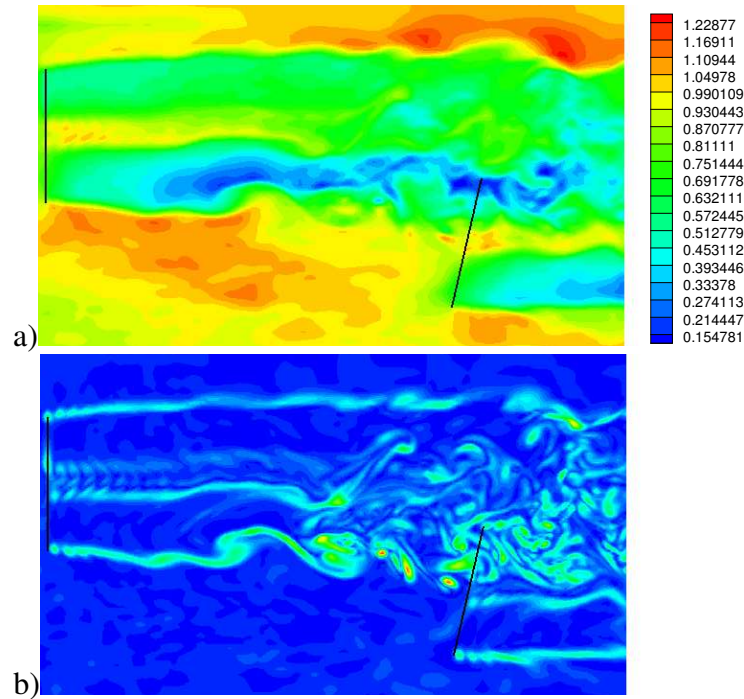


*Figure 12.5: Visualization of flow field in a horizontal plane located in hub height. The rotors are indicated as black lines. a) Streamwise velocity; b) Vorticity (regions of high vorticity appear as light colors)*

As seen the wake of the upstream turbine is characterized by significant asymmetry with the largest velocity deficit occurring at the side corresponding to an azimuth angle of  $180^\circ$ , i.e. the part of the wake which is located closest to the downstream rotor. Furthermore, the figure reveals a very inhomogeneous turbulence field inside the wake. At the side of the wake corresponding to an azimuth angle of  $0^\circ$  the tip vortex sheet, though becoming unstable, remains coherent until about two rotor radii downstream of the second turbine. On the other side of the wake (i.e. at  $\theta = 180^\circ$ ) the instability of the tip vortices is strong and causes rather large organized structures to form, which shortly after coalesce with the root vortices where after this

side of the wake approaches a state dominated by small scale turbulence.

From the contours of the streamwise velocity it is evident that the asymmetry of the wake is a feature that gradually builds up with downstream position and is apparently not occurring immediately downstream of the rotor, which is consistent with the very low degree of horizontal asymmetry observed on the blade loading. Recall from chapter 7 and 10 that the same feature was observed for the Tjæreborg turbine operating in a more moderately sheared inflow. The horizontal asymmetry of the wake deficit is, as also shown in the aforementioned chapters, due to the rotation of the wake, which causes low velocity air from the bottom part of the wake to surge upwards and being entrained. This is more clearly shown in figure 12.6, which presents the development of the mean velocity field at various distances downstream of the rotor. Note that the view is from downwind, i.e. the azimuth position  $0^\circ$  is to the right in the plots.

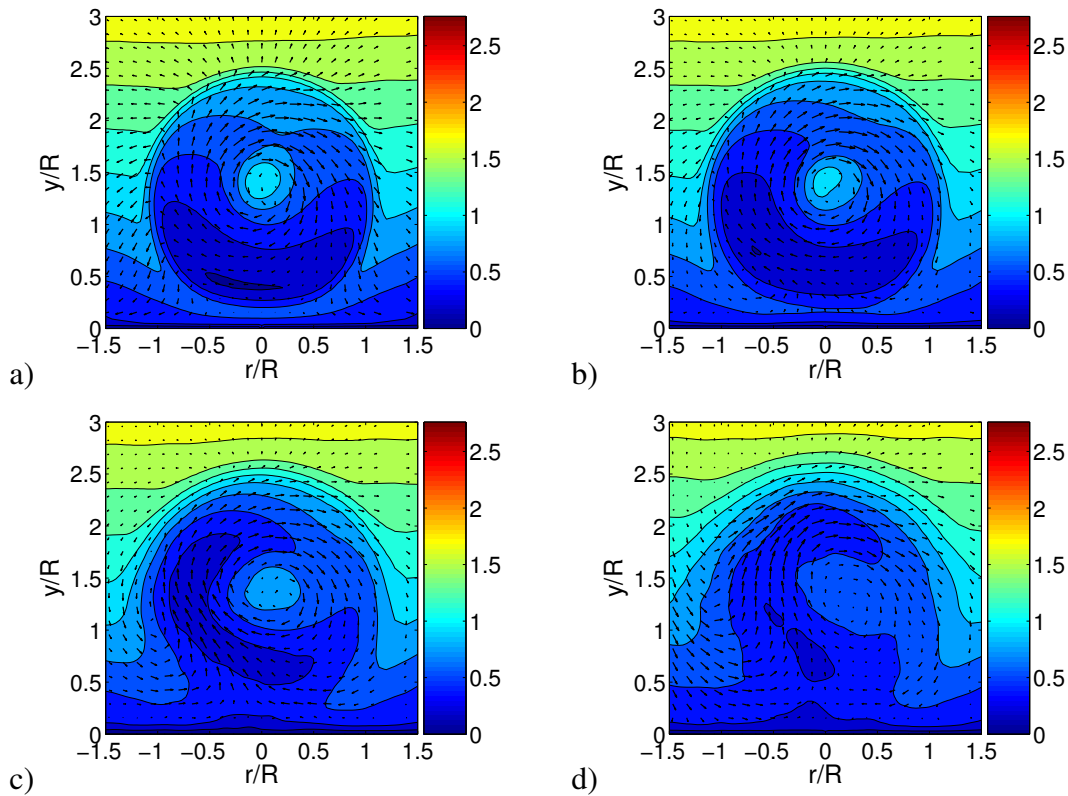


*Figure 12.6: Mean velocity field at different positions downstream of the first turbine. The contours refer to the streamwise velocity component. a)  $z/R = 1$ ; b)  $z/R = 2$ ; c)  $z/R = 4$ ; d)  $z/R = 6$*

From the figure it is evident that the wake deficit rotates in the opposite direction to the wind turbine as it is convected downstream, thereby creating a horizontal asymmetry in the wake. It is interesting to observe that the upwards movement of the air is accompanied with a significant flow of ambient air into the lower part of the wake. This behavior is in good qualitative agreement with the CFD study of Zahle and Sørensen [93].

Figure 12.7 shows the streamwise velocity profiles in a vertical plane going through the center of the upstream turbine. The wake develops rapidly with downstream position as a consequence of the break down of the vortex system. Furthermore, it is observed that the presence of the ground causes both the flow to be accelerated significantly below the rotor and to expand more

upwards than downwards. The nearly constant velocity profile observed respectively 8 and 10 rotor radii downstream of the rotor is indicative of a high degree of turbulent mixing. However at these positions the flow field is also significantly influenced by the wake of the downstream turbine.

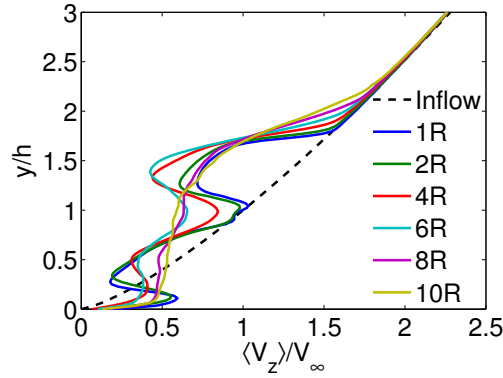


Figure 12.7: Time averaged streamwise velocity shear profiles through the center axis of the upstream rotor at various downstream positions.

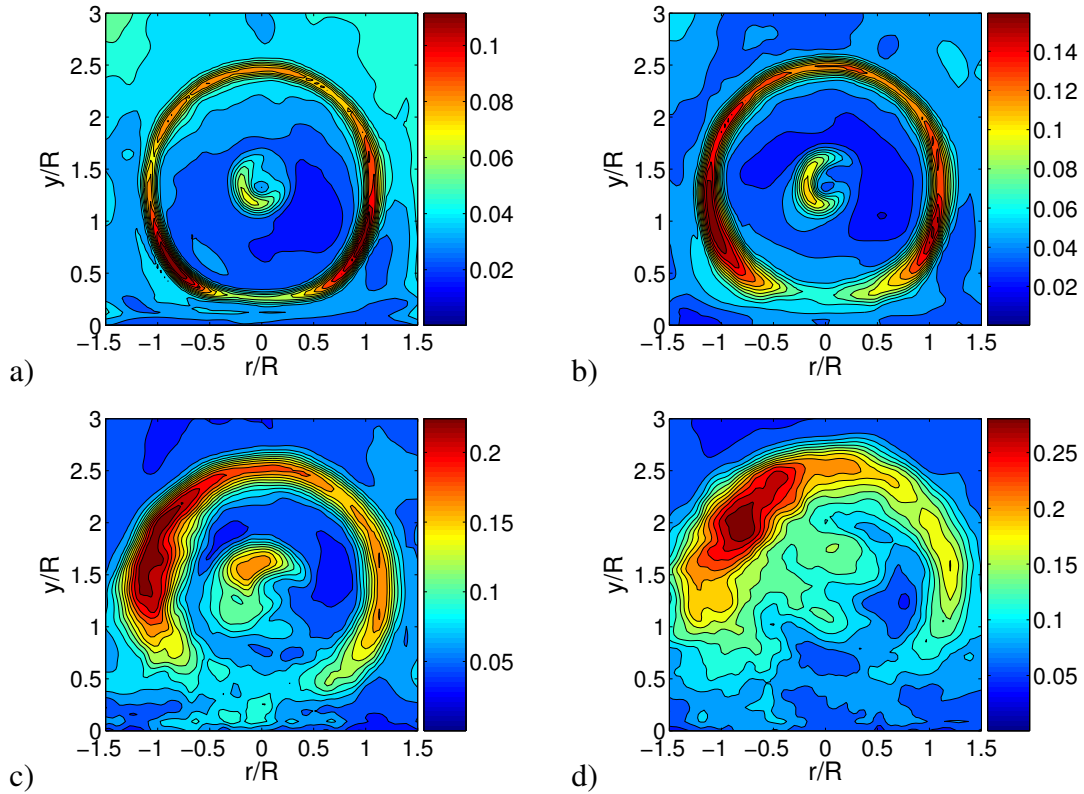


Figure 12.8: Streamwise normal stress,  $\langle v_z v_z \rangle$ , at different positions downstream of the first turbine. a)  $z/R = 1$ ; b)  $z/R = 2$ ; c)  $z/R = 4$ ; d)  $z/R = 6$

Figure 12.8, displays the downstream development of the streamwise turbulence intensity in the wake of the first turbine. Comparing figure 12.8 and 12.6 a general characteristic is that the turbulence intensity is largest in the regions of highest velocity gradients. From the figure it appears that the main mechanism for generating turbulence is provided by the development of the tip vortices which due to the rotation of the wake eventually maximizes in the area corresponding to an azimuth angle of approximately  $135^\circ$ .

## 12.5 Summary

The wakes of two NM80 turbines operating in a severe sheared flow have been simulated in a case where one of the turbines operated partly in the wake of the other.

Initially, the loading on the two rotors was investigated. The individual blade forces on the upstream rotor was as expected varying significantly over a rotor revolution but was nearly horizontally symmetric. The corresponding forces on the downstream rotor was undergoing a substantial drop when the blades were at azimuth positions where they were partly immersed in the wake of the upstream turbine. The azimuth positions where the blades of the downstream turbine were inside the wake of the first turbine were clearly identified as a significant increase of the turbulence intensity of the flow field experienced by the blades.

Secondly, in agreement with the findings of chapter 7 and 10, it was shown that the wake of the upstream turbine reveals increasingly horizontal asymmetry as it is transported downstream because the rotation of the wake causes low velocity air from the bottom part of the wake to move upwards on one side and high velocity air from the upper part of the wake to move downwards on the other side. Furthermore, it was shown that the wake due to the presence of the ground expands more upwards than downwards.

Finally, a study of the axial normal stresses in the wake showed that turbulence is mainly generated by the shear layer formed by the tip vortices.

# Chapter 13

## Conclusion

The wake flow of wind turbine rotors subject to various flow conditions have been simulated using the three-dimensional incompressible Navier Stokes solver EllipSys3D and the actuator line technique combined with refined modelling of wind shear and elegant inclusion of ambient turbulence using the Mann turbulence model. Comprehensive numerical results have been presented both for an isolated turbine operating in a flow field of systematically increased complexity and for interacting wakes between rows of turbines.

Numerical simulations of a wind turbine operating in a uniform inflow at various tip speed ratios revealed very different wake developments ranging from a completely stable wake governed by the induction of the tip and root vortices to a fully turbulent wake characterized by broad band turbulence.

A comparison between the measured and predicted power coefficient showed good agreement in the entire operational regime. The rather slight discrepancies between measurements and computations were mainly attributed to inaccurate airfoil data.

A thorough analysis of the wake characteristics was carried out including a study of the vortex properties and a characterization of the turbulence properties.

Simulations of an isolated turbine subject to a moderately sheared inflow showed that the non-symmetric loading on the rotor caused a skewed wake development, which was felt throughout the entire downstream region. In particular it was shown that the velocity deficit and the Reynolds stresses, as a consequence of wake rotation, are redistributed such that they become increasingly horizontally asymmetric with downstream position. It was argued that this effect, where low velocity air from the bottom part of the wake is moving upwards on one side and high velocity air from the upper part of the wake is moving downwards on the other side, could be responsible for the asymmetric development of the wake, which have been observed in several field experiments.

Computations on stand alone turbines subject to a non-sheared turbulent inflow revealed a significantly altered wake development compared to that observed in the laminar inflow case. The near wake was shown to interact with the atmospheric turbulence, which perturbs the helical vortex system whereby the wake breaks up in a chaotic process resulting in increased turbulence levels inside the wake.

A comparison between computations and measurements yielded fair agreement in terms of

mean wake deficit and turbulence intensity at a given downstream section.

Analysis of the spectral characteristics and coherence properties revealed an inhomogeneous and anisotropic wake characterized by having considerably smaller length scales than the ambient flow field.

It was furthermore shown that the main driver governing wake meandering clearly is the large scale coherent structures of the ambient turbulence.

The characteristics of the far wake turbulence field described in a meandering frame of reference was analyzed and it was found to be much more isotropic than in a fixed frame, thus suggesting that the main source of the anisotropy of the wake turbulence is the ambient flow field.

As a final study on isolated wind turbines a simulation was conducted on a turbine operating in a combined sheared and turbulent inflow. Compared to a laminar inflow the wake was found to break up much closer to the rotor, as expected. Besides a vertical skew caused by the inflow shear the wake also become horizontally asymmetric due to wake rotation in the same manner as was observed in the laminar sheared inflow case. However, as the wake breaks up and becomes increasingly turbulent it appears that the asymmetry gradually diminishes.

Analysis of the mean axial velocity deficit revealed that the wake, if properly scaled, may be considered fairly self-similar in the inner part of the wake, but that self-similarity in the outer and especially the lower part of the wake is questionable.

The development of the turbulence characteristics was studied in terms of the standard deviations, turbulent length scales and spectral coherence. The turbulence was, as in the wake of a turbine operating in a non-sheared turbulent inflow, shown to be inhomogeneous, anisotropic and characterized by having smaller length scales than the ambient flow field. The non-symmetric development of the turbulence was clearly visible as an circumferential variation of the normal stresses, whereas the length scales and coherence properties apparently were less sensitive to azimuth position. Still, however, the wake turbulence was very inhomogeneous, as all turbulence quantities were shown to be sensitive to the radial and downstream position.

Simulations on three turbines placed in a row along the mean wind direction showed very different wake behavior depending on whether the inflow was laminar or turbulent. The main influence of the ambient turbulence field is to perturb the otherwise stable vortex system of the first turbine, which thereby breaks up prior to impacting the second turbine. The break up of the wake causes an increased exchange of flow from the exterior, whereby the second and third rotor experiences higher mean velocities than in the corresponding laminar case.

It was furthermore shown that, wake meandering is clearly most significant in the turbulent inflow case, as expected. Despite this it was found that the equivalent yaw loads occurring on the downstream rotors in laminar inflow was quite large in particular for the third turbine, which experienced higher yaw loads than the corresponding turbine in turbulent inflow. The reason for this observation was argued to be due to the deeper wake deficit when the inflow is laminar.

Finally, simulations of two turbines operating in an atmospheric boundary layer characterized by strong shear and low ambient turbulence was presented in a case where the downstream turbine operated partly in the wake of the upstream one.

A study of the rotor loads revealed that the individual blade loading on each turbine varied considerably during a rotor revolution especially for the downstream turbine which in addition to a tilt moment caused by the extreme wind shear also experienced severe yaw moments due to the partial impact of the upstream rotor wake.

A subsequent investigation of the wake behavior showed that because of the low ambient turbulence the wake of the upstream turbine did not completely break up prior to impacting the downstream turbine and therefore, this turbine operated in a complex inflow which in part was undisturbed and in part governed by organized flow structures originating from the tip vortices.



# Appendix A

## Basic concepts of turbulence applied to wind turbine wakes

This appendix gives a brief review of some of the most basic quantities in turbulence analysis and how they are applied here in the study of wind turbine wakes.

### A.1 Turbulence statistics

One of the most useful statistical quantities in the study of turbulent flows is the two-point correlation tensor

$$R_{i,j}(\mathbf{x}, \mathbf{x}', t, t') = \langle v_i(\mathbf{x}, t) v_j(\mathbf{x}', t') \rangle \quad (\text{A.1})$$

where  $\langle \rangle$  denote ensemble averaging and  $v_i(\mathbf{x}, t) = V_i(\mathbf{x}, t) - \langle V_i(\mathbf{x}, t) \rangle$  represents a component of the fluctuating velocity.

For  $\mathbf{x} = \mathbf{x}'$  and  $t = t'$ ,  $\mathbf{R}$  is the well-known Reynolds stress tensor,  $\langle v_i v_j \rangle$ , which is of great importance because its elements represent the apparent normal and shear stresses arising from the fluctuating velocity field. The diagonal elements of the Reynolds stress tensor are the square of the standard deviation of each velocity component, i.e.

$$\sigma_i^2 = \langle v_i v_i \rangle \quad (\text{A.2})$$

where  $\sigma$  is the standard deviation (rms) and the index  $i$  denotes the considered velocity component (no summation implied).

### A.2 Correlation and scales of turbulence

From the two-point correlation tensor,  $\mathbf{R}$ , it is common to define respectively temporal and spatial correlations. For a fixed position in space the time correlation coefficients are defined as

$$\rho_{i,j}(\mathbf{x}, s) = \frac{\langle v_i(\mathbf{x}, t) v_j(\mathbf{x}, t + s) \rangle}{[\langle v_i(\mathbf{x}, t)^2 \rangle \langle v_j(\mathbf{x}, t)^2 \rangle]^{1/2}} \quad (\text{A.3})$$

Several different time correlations can be considered but the most important is perhaps the autocorrelation,  $\rho_{i,i}(\mathbf{x}, s)$ , which indicates the length of time a process correlates with itself. For

a random variable (such as a turbulent velocity) the autocorrelation coefficient has the property that it equals 1 at zero time-separation and approaches zero as the time-separation goes towards infinity.

A frequently used definition of a characteristic time scale of turbulence is the integral time scale computed by integrating the autocorrelation coefficient from zero to infinity

$$\tau_i(\mathbf{x}) = \int_0^\infty \rho_{i,i}(\mathbf{x}, s) ds, \quad (\text{A.4})$$

Physically, this quantity represents the memory of the flow or equally the average length of time it takes for a flow structure to pass a given point. The integral time scale is an important measure since it gives information about how large the time between two successive samples of a turbulent flow should be in order to be uncorrelated. Therefore, it plays a central role when analysing the statistics of turbulent flows because such analysis require many statistically independent samples.

The above concepts also applies for multi-point statistics, the most common being the two-point correlation coefficients, which here are defined as

$$B_{i,j}(\mathbf{x}, \mathbf{s}) = \frac{\langle v_i(\mathbf{x} + \frac{1}{2}\mathbf{s}) v_j(\mathbf{x} - \frac{1}{2}\mathbf{s}) \rangle}{[\langle v_i(\mathbf{x} + \frac{1}{2}\mathbf{s})^2 \rangle \langle v_j(\mathbf{x} - \frac{1}{2}\mathbf{s})^2 \rangle]^{1/2}} \quad (\text{A.5})$$

with the corresponding integral length scales defined by

$$L_{i,j}^{(k)}(\mathbf{x}) = \int_0^\infty B_{i,j}(\mathbf{x}, \mathbf{s}) d\mathbf{x} \quad (\text{A.6})$$

where the index  $k$ , indicate the direction of integration.

The integral length scales characterize the distance over which the turbulent fluctuations are correlated in a given direction and hence may be interpreted as the characteristic length scale of the coherent structures at the position in question.

The integral scales are easy to interpret but may be problematic to use in studies of wake turbulence which are characterized by rather large time scales and hence require long time series to obtain good estimates of the two point correlations. To illustrate this consider the wake of a wind turbine with a diameter of  $D = 80 \text{ m}$  operating at a wind speed of  $V_\infty = 10 \text{ m/s}$ . If it is assumed that a typical length scale of the wake is in the order of 1 rotor radius and Taylor's frozen turbulence hypothesis is adopted then the integral time scale should be in the order of  $\tau = R/V_\infty$ , i.e. about 4 seconds. If the turbulent fluctuations in the wake are further assumed to behave as Gaussian distributed random variables it can be shown that the square of the variability of the estimator of the variance is given by [8]

$$\epsilon_{var,N}^2 = \frac{2}{N} \quad (\text{A.7})$$

where  $N$  is the number of independent realizations used in the estimation. Hence, if an accuracy of say 5% is wanted in the estimate of the variance then  $N = 800$  independent samples are required. In order to obtain independent data the time between successive samples should be twice the integral time scale and hence the length of the time series required to get

an accuracy of 5% in the estimation of the variance is  $T = 2\tau N = 6400 \text{ s} \approx 107 \text{ min}$ . Even though the required length of time may be reduced in case of a rotationally symmetric flow by averaging in the circumferential direction, the above example clearly show that generally rather long time series are needed to establish good estimate of the second order statistics and hence also the integral scales. In practice analysis of the wind is normally based on a sufficient number of 10 minute measurements to establish proper statistics. However such measurements rarely exist in the form of synchronized two-point measurements from which the integral length scales could be deduced. Characteristic length scales could also be estimated from the integral time scale through the Taylor hypothesis, which is quite accurate when  $v/V_\infty \ll 1$ , but may fail in some free shear flows [63]. On the other hand, though numerical studies provide the necessary spatial resolution they are often too computational demanding to establish the required time length.

An alternative way of establishing characteristic turbulent length scales, presented in [43], is by fitting the one-dimensional spectra obtained in the wake with a generic spectrum. In the following, the Kaimal spectrum is used for this purpose since this spectrum often is applied as a basis for wind field simulation in connection with wind turbine design. The Kaimal spectrum,  $S_k$ , is defined in a number of different but equivalent ways in the literature and here the definition adopted in the IEC standard [34] is used

$$S_{k,i} = 4\sigma_{k,i}^2 \frac{L_{k,i}/V_\infty}{(1 + 6fL_{k,i}/V_\infty)^{5/3}} \quad (\text{A.8})$$

where  $\sigma_{k,i}$  is the standard deviation,  $f$  is the frequency,  $L_{k,i}$  is a characteristic length scale, referred to as the Kaimal length scale and the index  $i$  refer to the velocity component in question. In order to obtain  $L_{k,i}$  the above expression is fitted to the spectra obtained in the wake by simultaneously adjusting  $\sigma_k$  as well as  $L_k$  to obtain the optimal agreement in a least square sense. For this purpose the non-linear Levenberg-Marquardt [64] method has been used.

Even though the derived length scales  $L_{k,i}$  may be more difficult to interpret than the integral length scale its definition is convenient since a characteristic eddy size can be defined from measurement in only one point. However, it is clear that the method only makes sense when the used generic spectrum at least to some degree resembles the spectra actually obtained in the wake. That is, when using the Kaimal spectrum the method only applies at positions in the wake where the turbulence is fully developed.

Furthermore, since the method relies on estimates of the spectra, the accuracy of the spectral estimator should be addressed. Generally, the spectra are estimated by dividing the time series into a number of equally sized segments, which are overlapping each other with one half of their length, and computing the spectrum as the ensemble average of the absolute square of the Fourier transform of each segment. The advantage of using a 50% overlap of the segments is that the variance of the spectral estimator is smaller than when using non-overlapping segments. Denoting the number of segments by  $N$  and assuming the time series sufficiently long the variance of the spectral estimator when using non-overlapping segments is in the order  $N^{-1}$ . Even though the corresponding reduction in the variance is only approximately  $11/(9N)$  [64] when using 50% overlap the overall reduction is significantly reduced in this case because the total number of segments is nearly doubled compared to using non-overlapping segments.

The ability of the algorithm used to extract  $L_k$  and  $\sigma_k$  from a given turbulence field was tested by applying it to a discrete velocity signal with spectral characteristics given by equation A.8, where  $V_\infty = 1$ ,  $L_k = 1$  and  $\sigma_k = 0.15$ . The length of the time series was 1024 seconds and the time step between two samples was 0.125 seconds. The spectral estimate of the signal was estimated according to the above described method with the time series divided into a number of segments with a 50% overlap.

Table A.1 presents examples of the estimated  $L_k$  and  $\sigma_k$  for different numbers of segments. As seen the method is rather robust and is capable of predicting the correct  $L_k$  and  $\sigma_k$  with an accuracy, which is within the relative standard deviation of the spectral estimator.

The reason that the algorithm generally overestimates the true standard deviation is that the Kaimal spectrum (equation A.8) is defined for the entire frequency range from zero to infinity. Since the variance,  $\sigma^2$ , is the integral under the spectrum, this implies that the estimated variance includes contributions from the parts of the Kaimal spectrum, which are outside the frequency limits of the actual finite spectrum.

$N$	7	17	31	63
$L_k$	0.98	1.01	1.03	1.00
$\sigma_k$	0.159	0.159	0.160	0.161

Table A.1: Predicted  $L_k$  and  $\sigma_k$  for different  $N$ . The true standard deviation and length scale are respectively  $\sigma_k = 0.15$  and  $L_k = 1$

In order to further validate the method figure A.1 shows an example where equation A.8 has been fitted to a spectrum obtained in the wake of the Tjæreborg turbine operating in a uniform inflow velocity of  $V_\infty = 6 \text{ m/s}$ . Note that the highest frequency range of the spectrum is excluded in the fitting procedure because this part is influenced by numerical diffusion. As seen the correlation between the two curves is generally very good, hence indicating that the Kaimal spectrum is a suitable generic spectrum in this case.

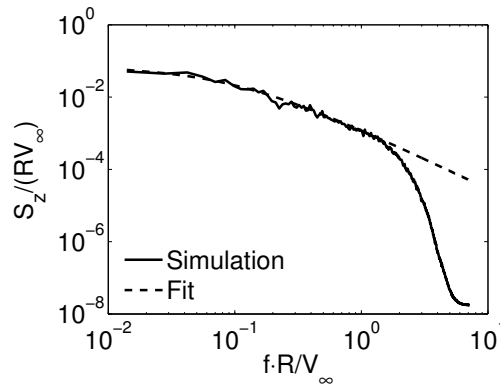


Figure A.1: Example of a Kaimal spectrum fitted to the spectrum observed at  $r/R = 0$  and  $z/R = 14$  for  $V_\infty = 6 \text{ m/s}$ . (See chapter 5)

Above, it has been described how characteristic turbulent length scales can be computed either from the two-point correlations, the Kaimal spectrum or from the integral time scales. Even though the three definitions of the length scales are not expected to yield exactly the same results they should at least be correlated. To verify this, the azimuthally averaged radial distribution of

each length scale was computed in the far wake of the M80 turbine and the results are compared in the left plot of figure A.2. As seen the resemblance of the three types of length scales is generally good, which suggests that their physical significance is connected. In the right plot of figure A.2 the corresponding distribution of the actual and the estimated standard deviation in the wake is compared and it is evident that these also compare well both in terms of level and shape.

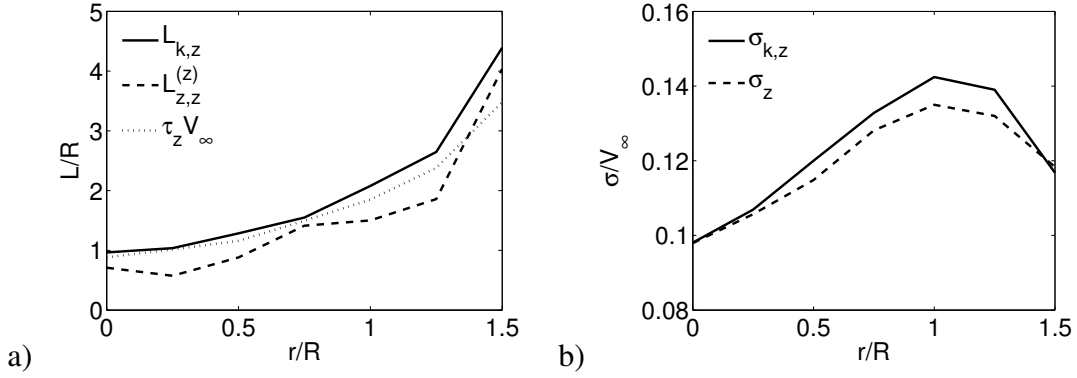


Figure A.2: Comparison of radial distribution of a) different types of characteristic length scales and b) actual and predicted standard deviation in the wake of the NM80 turbine at  $z/R = 6$  and  $V_\infty = 10$  m/s (see chapter 9)

The above discussion and comparison seems to verify that the method of estimating length scales from the Kaimal spectrum is useful and therefore it was decided to use the Kaimal length scale,  $L_{k,i}$ , as a measure of the characteristic length scale of the flow in the present thesis.

### A.3 Coherence

The turbulent velocity fluctuations between two points in space will be correlated to varying degrees depending on their location as well as the characteristic length and time scales of the turbulence.

Typically, the spectral coherence is used as a frequency dependent measure of the amount of correlation between the turbulent velocities in two points  $p_i$  and  $p_j$ . Here, the spectral coherence is defined as

$$coh = \frac{|S_{i,j}(f)|^2}{S_{i,i}(f)S_{j,j}(f)} \quad (A.9)$$

where,  $S_{i,j}$  is the cross-spectrum between the two points and  $S_{i,i}$  and  $S_{j,j}$  are the one-dimensional spectra of the turbulent velocity in each point.

Due to the use of limited datasets the estimates of the coherence have unavoidable statistical errors, which should be assessed. Obviously, if the definition in equation A.9 is applied to compute the coherence function using only a single realization of two random processes the result will become identical unity since the cross-spectrum,  $S_{i,j} = C + iQ$ , is a vector of size  $|S_{i,i}S_{j,j}|$  and direction  $\theta$ .

This source of distortion can only be prevented if the cospectrum,  $C$ , and the quadrature spectrum,  $Q$ , are averaged over a number of time series. Thus, if the time series are completely

uncorrelated at a given frequency, this implies that  $\Delta\theta$  is distributed randomly and that both  $C$  and  $Q$  on averaging becomes zero (if the number of time series is large).

The statistical errors associated with the coherence estimate are discussed in [48], [50] and [42]. For  $N$  independent segments of two time series Kristensen and Kirkegaard [42] derived the following analytical expressions of respectively the bias and the variance of the coherence estimator,  $coh_N$

$$Bias(coh_N) = \alpha_1 - coh \quad (A.10)$$

$$Var(coh_N) = \alpha_2 - \alpha_1^2 \quad (A.11)$$

Here  $coh$  denote the true coherence between two time series, while  $\alpha_1$  and  $\alpha_2$  are given by respectively

$$\alpha_1 = 1 - \frac{N-1}{N}(1-coh)^N {}_2F_1(N, N; N+1; coh) \quad (A.12)$$

$$\begin{aligned} \alpha_2 = & 1 - (1-coh)^N(N-1) \\ & \times \left[ \frac{N}{N+1} {}_2F_1(N+1, N; N+2; coh) \right. \\ & \left. - \frac{N-2}{N} {}_2F_1(N, N; N+1; coh) \right] \end{aligned} \quad (A.13)$$

where  ${}_2F_1$  is the hypergeometric function

In figure A.3 these expressions are plotted as a function of the true coherence for different number of segments.

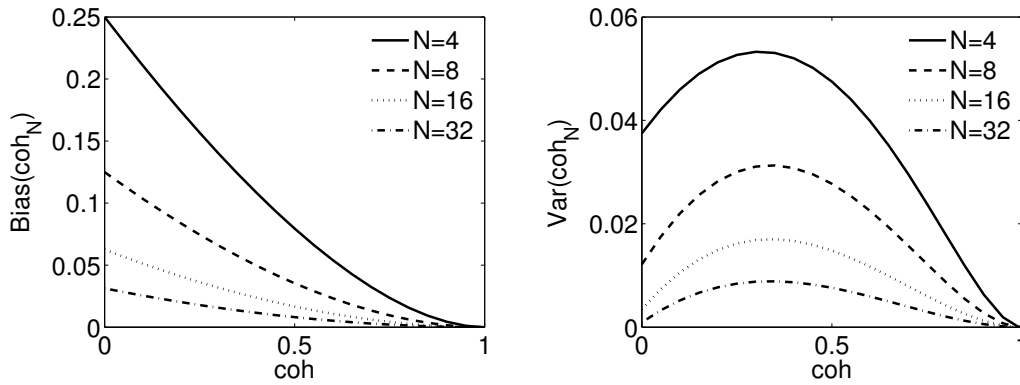


Figure A.3: Bias and variance of the coherence estimator,  $coh_N$  as a function of the true coherence for various choices of  $N$

As seen the coherence is systematically overestimated but the difference reduces with increasing number of segments. Likewise, it is seen that the variance of the coherence estimator is reduced when the number of segments is increased. However, it should be appreciated that choosing a large number of segments from a finite dataset reduces the accuracy of the estimator in the low frequency region where the coherence is large. Therefore, the number of segments should generally be chosen to limit statistical error, without compromising the accuracy of the estimate in the low frequency region.

To overcome this difficulty a practical approach was adopted in the present work whereby the coherence function, for each pair of time series, was estimated for different numbers of 50% overlapping segments. These estimates were then combined in a suitable manner to obtain a single optimal representation of the coherence function, which benefits from both low spectral distortion and limited bias.

Since the turbulence in a wind turbine wake generally is spatially inhomogeneous the coherence will vary in space and therefore the coherence between two points is governed by 7 parameters

$$coh = coh(r_i, r_j, \theta, \Delta\theta, z_i, z_j, f) \quad (\text{A.14})$$

where  $r$ ,  $\theta$  and  $z$  is respectively the radial, azimuthal and axial position and  $\Delta\theta$  denote the angular displacement between the two points.

The dominant parameter governing the coherence function is expected to be the displacement between the two points and therefore it is convenient to express the function in terms of this parameter instead of the angular displacement.

In order to achieve this consider two points  $p_i$  and  $p_j$  located at the same downstream position as sketched in figure A.4. The two points are spaced a distance  $d$  apart and the line connecting them has a midpoint,  $m$ , which is located  $r_m$  from the centre axis at an azimuthal position of  $\theta$ . The angle  $\phi_m$  and the separation length  $d$  now define the position of the points compared to the midpoint  $m$ .

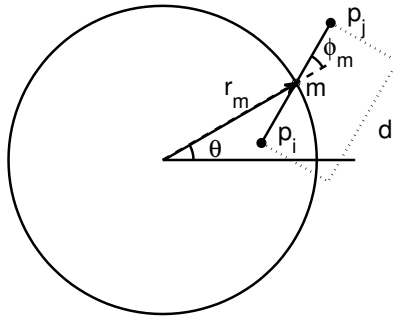


Figure A.4: Sketch used to define the coordinates  $r_m$ ,  $d$  and  $\phi_m$

The present work is restricted to only considering in-plane coherence, i.e.  $z_i = z_j$  and therefore the coherence function can be expressed as

$$coh = coh(r_m, \phi_m, \theta, d, f) \quad (\text{A.15})$$

For rotationally symmetric flows it follows that it is sufficient to consider the mutual location of the points compared to a given azimuth direction and that only  $\phi_m \in [0^\circ; 90^\circ]$  is relevant. Thus, for axisymmetric flows the functional form of the coherence may be further reduced to

$$coh = coh(r_m, \phi_m, d, f) \quad (\text{A.16})$$

Based on the simple exponential model commonly used for representing atmospheric turbulence (see e.g. [34]) it will be assumed that the spectral coherence in the wake may be expressed on

the form

$$coh = \exp \left( -C(r_m, \phi_m, \theta) \frac{f \cdot d}{V_\infty} \right) = \exp (-C(r_m, \phi_m, \theta) f_r) \quad (\text{A.17})$$

where  $C(r_m, \phi_m, \theta)$  is the coherence decrement and  $f_r$  is the reduced frequency, which expresses the relation between the separation length and a characteristic eddy size connected to the frequency. For homogeneous turbulence  $C(r_m, \phi_m, \theta)$  is obviously a constant and the coherence is then solely governed by the reduced frequency.

A consequence of the above assumption is that the coherence, for fixed values of  $r_m$ ,  $\phi_m$  and  $\theta$  should be insensitive to changes in,  $d$ , when plotted against  $f_r$ . That this is probably a fair assumption is verified in figure A.5, where the coherence for fixed values of  $r_m$ ,  $\phi_m$  and  $\theta$ , is seen to nearly collapse on a single curve when plotted against the reduced frequency for various displacements.

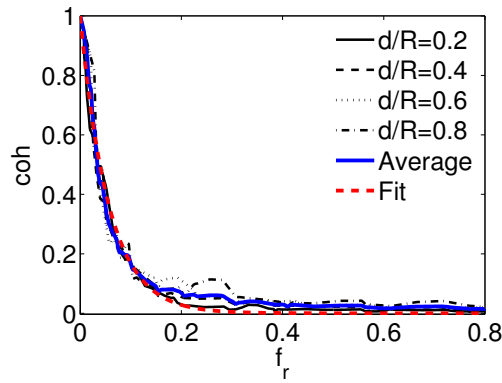


Figure A.5: Comparison of coherence functions computed for various displacements in the wake of the Tjæreborg turbine at  $V_\infty = 10$  m/s,  $r_m = 0.6$ ,  $\phi_m = 0$  and  $z/R = 14$  (see chapter 9). Also shown is the average of all curves as well as the fitted curve using equation A.17 with optimal choice of  $C$

Having accepted equation A.17 as suitable for modelling the coherence it only remains to determine  $C(r_m, \phi_m, \theta)$ . This is done by, at each combination of  $r_m$ ,  $\phi_m$  and  $\theta$ , making a least-square fit of equation A.17 to the curve obtained by averaging the coherence curves over the different displacements (the blue curve in figure A.5).

The algorithm developed for extracting the coherence decrement was validated by applying it to a synthetic 3D turbulence field with known spectral characteristics and coherence properties. The turbulence field was generated using the algorithm presented in [84], which uses Fourier analysis to create a number of correlated time series from the power spectrum and a coherence function. In the test the spectrum was defined from equation A.8, with  $V_\infty = 1$ ,  $L_k = 1$  and  $\sigma_k = 0.15$ , while the coherence function was given by equation A.17 with  $C = 20$ . Correlated time series were generated in 25 equally spaced points. The length of each time series was 128 seconds and the time step between two samples was 1/16. The coherence function between two points was then estimated for different spacing using the method outlined above. Note that the homogeneity of the turbulence field was utilized in the estimation and thus the coherence function was computed as the average over all points having the same distance. Table A.2



presents the coherence decrement obtained by fitting equation A.17 to the coherence function for various displacements between points.

$d$	0.05	0.1	0.2	0.4
$C$	19.3	19.6	19.5	19.3

Table A.2: Estimated coherence decrement for different spacings between two points. The true coherence decrement is 20

The coherence decrement is as expected from the theoretical considerations systematically slightly underestimated but appears to be fairly insensitive to changes in the distance between the two points.

## A.4 Proper orthogonal decomposition (POD)

In order to analyze the dynamics of the dominant coherent structures of the studied wakes use has been made of the Proper orthogonal decomposition (POD) technique. Several versions of the POD technique have been developed and in the present work the so-called snapshot version is applied. A good description of the POD technique is presented in Holmes et al. [33] and in the following only a brief outline will be made. The idea of the proper orthogonal decomposition is, like for any other orthogonal decomposition, to represent the turbulent flow on the form

$$\mathbf{v}(\mathbf{x}, t) = \sum_{i=1}^m a_i(t) \phi_i(\mathbf{x}) \quad (\text{A.18})$$

where  $\phi_i$  is a set of real orthogonal basis functions (modes) and  $a_i$  are the random basis function coefficients. There are infinitely many choices of the basis function, the most well known being the Fourier modes, however, a defining property of the POD is that the basis functions are chosen to maximize the energy contained in the investigated domain.

In the snapshot POD a given discrete dataset consisting of  $N$  snapshots of the velocity (each with  $l \times m$  data points) are arranged in vectors  $\mathbf{U}_n = [V_x^1 \dots V_x^{lm}, V_y^1 \dots V_y^{lm}, V_z^1 \dots V_z^{lm}]$  and the ensemble average is subtracted thereby obtaining vectors,  $\mathbf{u}_n$ , containing the fluctuating part of the velocity.

$$\mathbf{u}_n = \mathbf{U}_n - \frac{1}{N} \sum_{i=1}^N \mathbf{U}_i, \quad n = 1 \dots N \quad (\text{A.19})$$

From these vectors the  $N \times N$  covariance matrix is constructed

$$C_{ij} = \mathbf{u}_i \cdot \mathbf{u}_j \quad (\text{A.20})$$

Solving the eigenvalue problem for  $\mathbf{C}$  gives the eigenvectors,  $\mathbf{g}^k$  from which the normalized orthogonal basis functions, also referred to as modes, can be determined

$$\phi_k = \frac{\sum_{i=1}^n g_i^k \mathbf{u}_i}{\left\| \sum_{i=1}^n g_i^k \mathbf{u}_i \right\|} \quad (\text{A.21})$$

where  $g_i^k$  is the  $i$ 'th component of the normalized eigenvector corresponding to the  $k$ 'th eigenvalue,  $\lambda_k$ .

It can be shown that the eigenvalue  $\lambda_k$  corresponding to the eigenvectors  $\mathbf{g}^k$  represent the energy contained in the corresponding mode. Therefore, by ordering the eigenvalues as  $\lambda_1 > \lambda_2 > \dots > \lambda_m > 0$  the first modes represents the most energetic and dominant coherent structures in the flow.

The time varying amplitudes of the POD modes can be found by projection of the velocity field on the basis modes

$$\mathbf{A} = \Phi^T \mathbf{V} \quad (\text{A.22})$$

where  $\mathbf{A}$ ,  $\Phi$  and  $\mathbf{V}$  are matrices containing respectively the  $\mathbf{a}^k$ ,  $\phi^k$  and  $\mathbf{u}^k$  vectors arranged columnwise.

Having established the amplitude coefficients of each mode a given snapshot can be reconstructed as follows

$$\mathbf{U}_n \approx \sum_{i=1}^m \phi^i a_i^n + \frac{1}{N} \sum_{j=1}^N \mathbf{U}_j \quad (\text{A.23})$$

where  $m$  denotes the number of modes included in the reconstruction of the flow.

Evidently the size of the eigenvalue problem depends on the number of snapshots ( $\text{rank}(C) = N$ ) and therefore the snapshot POD seems attractive when analysing sets of data with a high spatial and a low temporal resolution. Nevertheless, it is also clear that knowledge about the two-point correlation is essential in a POD analysis and therefore the analysis should be based on sufficient statistically independent data to establish good estimates of the second order statistics. However, as shown in section A.2 obtaining good estimates of the full two-point correlation of a typical wind turbine wake is very demanding and in practice the POD analysis presented in this thesis are not based on dataset with completely converged second-order statistics. However, for the current work this is not expected to have a significant impact on the results because the POD technique here only is used to analyze the large scale dynamics of given datasets and not to establish general low dimensional models for the wake.

In order to validate the implementation of the snapshot POD figure A.6, for a position 10 rotor radii downstream of the NM80 turbine, compares a given snapshot of the axial velocity fluctuations with the corresponding reconstructed field determined from equation A.23. The shown reconstructed field contains 90% of the total energy and for this reason should resemble the snapshot well. As seen this is also the case and therefore it was concluded that the method was properly implemented.

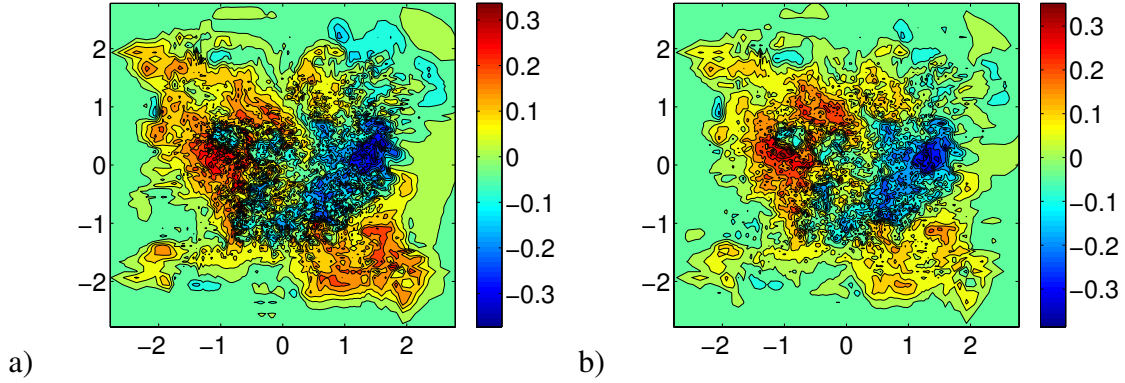


Figure A.6: a) Snapshot of axial fluctuating velocity and b) Corresponding reconstructed velocity field containing approximately 90% of the energy

## A.5 Self-similarity

The concept of self-similarity is frequently used in the study of turbulent free shear flows and is also the basis of many kinematic models for the far wake of wind turbines.

Self-similarity implies that a given flow field after a developing region reaches a stage where the shape of the mean profile of a given quantity (such as the velocity) stay unchanged with downstream position and hence if scaled properly these profiles collapse on a single curve. It is well known from experiments [63] that some of the most commonly studied turbulent free shear flows (e.g. jets) become self-similar after a certain downstream position.

For an axisymmetric wake such as formed behind a disk the scaled self-similar velocity profile is defined as

$$f_v(\xi) = \frac{V_\infty - \langle V_z(r, z) \rangle}{V_s(z)} \quad (\text{A.24})$$

Here the characteristic velocity difference,  $V_s$  is defined as

$$V_s(z) = V_\infty - \langle V_z(0, z) \rangle \quad (\text{A.25})$$

and  $\xi = r/r_{1/2}$  is the radial coordinate scaled with the wake half width,  $r_{1/2}$  defined from

$$\langle V_z(r_{1/2}, z) \rangle = V_\infty - \frac{1}{2} V_s(z) \quad (\text{A.26})$$

Actually, as mentioned in [63] the axisymmetric wake is not exactly self-similar; however, it approaches this stage asymptotically in the far wake as  $V_s/V_\infty$  goes toward zero. In practice self-similarity is observed for  $V_s/V_\infty$  less than about 0.1.

Introducing the turbulent viscosity concept and assuming a constant turbulent viscosity in the wake it can be shown that the self-similar velocity profile in the axisymmetric wake is given by [63]

$$f_v(\xi) = \exp(-\alpha \xi^2) \quad (\text{A.27})$$

where  $\alpha = \ln 2$ .

## A.6 Summary

This appendix has provided a description of some important concepts in the study of turbulent flows.

Initially, the concept of characteristic scales of turbulence was presented and some issues related to their application in the study of wind turbine wakes were discussed. It was argued that the use of integral length scales, computed from the two-point correlations, may be inaccurate in the study of wake turbulence due to insufficient temporal resolution and instead it was proposed to use a method where the characteristic length scales are estimated by fitting a generic spectrum to the spectra obtained in the wake.

Secondly, the idea of spectral coherence was described with a special focus on how it can be applied for studying wind turbine wakes. In this connection it was shown that an extended formulation of the exponential expression commonly used to describe coherence of the fluctuating velocity in the atmosphere also seems to be suitable for wind turbine wakes.

Following this the snapshot version of the Proper Orthogonal Decomposition method was briefly outlined and finally the concept of self-similarity for axisymmetric free-shear flows was described.

# Bibliography

- [1] Abbott, I.H. and von Doenhoff, A.E. Theory of Wing Sections, 1st ed. Dover Publications, Inc., 1959.
- [2] Ainslie, J.F. Development of an eddy viscosity model for wind turbine wakes. Proc. 7<sup>th</sup> BWEA Wind Energy Conference, Oxford, 1985
- [3] Ainslie, J.F. Wake modelling and the predictions of turbulence properties. Proceedings of the 1986 8<sup>th</sup> British Wind energy Association Conference, Cambridge, 1986, pp. 115-120.
- [4] Ainslie, J.F. Calculating the flow field in the wake of wind turbines. Journal of Wind Engineering and Industrial Aerodynamics, 27, pp. 213-224, 1988.
- [5] Alinot, C. and Masson, C. Aerodynamic simulations of wind turbines operating in atmospheric boundary layer with various thermal stratifications AIAA-2002-42, ASME Wind Energy Symposium, 40th collection of technical papers, Reno, January, 2002.
- [6] Bareiss, R. Guidati, G. and Wagner, S. Wake simulation for wind turbines with a free, prescribed and hybrid wake method, Proc. 10th IEA Symp. on Aerodynamics of Wind Turbines, Edinburgh, 1996.
- [7] Bechmann, A. Large-Eddy Simulation of Atmospheric Flow over Complex Terrain. PhD Dissertation, Risø-PhD-28(EN), Risø National Laboratory, Roskilde, Denmark, 2007.
- [8] Bendat, J.S. and Piersol, A.G. Random Data - Analysis and Measurement Procedures. Second edition, John Wiley & Sons, 1986.
- [9] Bingöl, F. Mann, J. and Larsen, G.C. Laser Measurements of Wake Dynamics Scientific proceedings at EWEC, Milan, 2007.
- [10] Cleijne, J.W. Results of Sexbierum wind farm. Report 92-388, TNO-MT, Apeldoorn, Netherlands, 1992.
- [11] Coton F.N. and Wang T. The prediction of horizontal axis wind turbine performance in yawed flow using an unsteady prescribed wake model. Proceedings of the Institution of Mechanical Engineers, Part A. J Power Energy 1999;213:33-43.
- [12] Crespo A. and Hernández J. Numerical modelling of the flow field in a wind turbine wake. In: Proceedings of the 3<sup>rd</sup> Joint ASCE/ASME Mechanics Conference, Forum on Turbulent Flows. ASME, FED-vol. 76, La Jolla, CA, USA, 1989.

- [13] Crespo, A. and Hernández, J. Turbulence characteristics in wind-turbine wakes. *Journal of Wind Engineering & Industrial Aerodynamics*. Vol.61 Issue.1, pp. 71-85, 1996.
- [14] Crespo, A., Hernández J. and Frandsen S. Survey of Modelling Methods for Wind Turbine Wakes and Wind Farms. *Wind Energy*, Vol. 2, pp. 1-24, 1998.
- [15] Dobrev, I., Massouh, F. and Rapin, M. Actuator surface hybrid model. *Journal of Physics: Conference Series*. The Science of Making Torque from Wind. Technical University of Denmark, Lyngby, August 2007.
- [16] Ebert P.R. and Wood D.H. The near wake of a model horizontal-axis wind turbine-I. Experimental arrangement and initial results. *Renewable Energy*, Vol. 12, No. 3, pp. 225-243, 1997.
- [17] Ebert P.R. and Wood D.H. The near wake of a model horizontal-axis wind turbine-II. General features of the three-dimensional flowfield. *Renewable Energy*, Vol. 18, pp. 513-534, 1999.
- [18] Ebert P.R. and Wood D.H. The near wake of a model horizontal-axis wind turbine Part 3: properties of the tip and root vortices. *Renewable Energy*, Vol. 22, pp. 461-472, 2001.
- [19] Felli, M., Giulio, G., Roberto, C. Effect of the number of blades on propeller wake evolution. *Experiments in Fluids*. Vol.44 Issue.3. pp. 409-418. 2008.
- [20] Ferziger, J.H. and Peric, M. *Computational Methods for Fluid Dynamics*, 3rd Edition, Springer, 2002.
- [21] Fingersh, D., Simms, D. Hand, M., Jager, D., Cortrell, J., Robinson, M., Schreck, S. and Larwood, S. Wind tunnel testing of NREL's unsteady aerodynamics experiment AIAA paper 2001-0035, 2001.
- [22] Frandsen, S., Chacón, L., Crespo, A., Enevoldsen, P., Gómez-Elvira, R., Hernández, J., Højstrup, J., Manuel, F., Thomsen, K. and Sørensen, P. Measurements on and Modelling of Offshore Wind Farms. Risø-R-903(EN), Risø National Laboratory, Technical University of Denmark, Roskilde, Denmark, 1996.
- [23] Frandsen, S., Barthelmie, R., Pryor, S., Rathmann, O., Larsen, S., Højstrup, J., and Thøgersen, M. Analytical modelling of wind speed in large offshore wind farms. *Journal of Wind Energy*, Vol. 9, Issue 1-2, 2006.
- [24] Frandsen, S.T. Turbulence and turbulence-generated structural loading in wind turbine clusters. Risø-R-1188(EN). Risø National Laboratory, Technical University of Denmark, Roskilde, Denmark, 2007.
- [25] Froude RE. On the part played in propulsion by difference in pressure. *Transaction of the Institute of Naval Architects*; 30: 390.423, 1889.
- [26] Glauert, H. Airplane Propellers, In *Aerodynamic Theory*, Durand WF (ed.). Dover, New York, 4(Div. L), 1963

- [27] Gómez-Elvira, R., Crespo, A. and Migoya, E. Anisotropy of turbulence in wind turbine wakes. *Wind Engineering and Industrial Aerodynamics*. Vol. 93, 2005.
- [28] Grant, I and Parkin, P. A DPIV study of the trailing vortex elements from the blades of a horizontal axis wind turbine in yaw. *Experiments in Fluids*, 28. Springer-Verlag, 2000.
- [29] Hansen, M.H., Fuglsang, P. and Thomsen K. Aeroelastic modeling of the NM80 turbine with HAWC. Risø-I-2017(EN). Risø National Laboratory, Technical University of Denmark, Roskilde, Denmark, 2004.
- [30] Hansen, M.O.L. *Aerodynamics of Wind Turbines*. Second edition. Earthscan, 2008.
- [31] Höglström, U., Asimakopoulou, D.N., Kambezidis, H., Helmis, C.G., Smedman, A. A field study of the wake behind a 2 MW wind turbine. *Atmospheric Environment* 22(4):803-20, 1988.
- [32] Højstrup, J. Spectral coherence in wind turbine wakes. *Journal of Wind Engineering & Industrial Aerodynamics* 80, pp. 137-146, 1999.
- [33] Holmes, P., Lumley, J. and Berkooz, G. *Turbulence, coherent structures, dynamical systems and symmetry*. Cambridge University Press, 1996.
- [34] IEC 61400-1 Ed. 3 (2005): *Wind turbines - Part 1: Design requirements*. International Electrotechnical Commission.
- [35] Ivanell, S.S.A. *Numerical Computations of Wind Turbine Wakes*, Licentiate Thesis, TRITA-MEK, Technical Report 2005:10, Stockholm, Sweden, 2005
- [36] Ivanell, S., Mikkelsen, R., Sørensen, J.N. and Henningson, D. Numerical analysis of the tip and root vortex position in the wake of a wind turbine. *Journal of Physics: Conference Series. The Science of Making Torque from Wind*. Technical University of Denmark, Lyngby, August 2007.
- [37] Ivanell, S., Mikkelsen, R., Sørensen, J.N. and Henningson, D. Three dimensional actuator disc modelling of wind farm wake interaction. In *proceedings of the 2007 EWEC conference*, Bruxelles, 2008.
- [38] Jimenez, A., Crespo, A. Migoya, E. and Garcia, J. Advances in large-eddy simulation of a wind turbine wake. *Journal of Physics: Conference Series. The Science of Making Torque from Wind*. Technical University of Denmark, Lyngby, August 2007.
- [39] Jimenez, A., Crespo, A. Migoya, E. and Garcia, J. Large-eddy simulation of spectral coherence in a wind turbine wake. *Environmental Research Letters*. 3, 2008.
- [40] Kasmi, A.E. and Masson, C. An extended  $k-\epsilon$  model for turbulent flow through horizontal-axis wind turbines. *Journal of Wind Engineering and Industrial Aerodynamics* 96, 103-122, 2008.
- [41] Kempf, A., Klein, M. and Janicka, J. Efficient Generation of Initial -and Inflow Conditions for Transient Turbulent Flows in Arbitrary Geometries. *Flow, Turbulence and Combustion* 74:67-84, Springer, 2005

- [42] Kristensen, L. and Kirkegaard, P. Sampling problems with spectral coherence. Report No. R-526, Risø National Laboratory, Roskilde, Denmark, 1986.
- [43] Larsen, G.C., Madsen, H.Aa., Bingöl, F. Mann, J., Ott, S., Sørensen, J.N., Okulov, V., Troldborg, N., Nielsen, M., Thomsen, K., Larsen, T.J. and Mikkelsen, R. Dynamic wake meandering modelling. Risø-R-1607(EN). Risø National Laboratory, Technical University of Denmark, Roskilde, Denmark, 2007.
- [44] Larsen, G.C., Madsen, H.Aa., Thomsen, K. and Larsen, T.J. Wake Meandering - A pragmatic Approach. Wind Energy, 2008.
- [45] Madsen, H.A. and Rasmussen, F. The influence of energy conversion and induction from large blade deflections. In: Proceedings of the European Wind Energy Conference, James & James, 1999.
- [46] Madsen, H.A., Larsen, G.C. and Thomsen, K. Wake flow characteristics in low ambient turbulence conditions, Presented at Copenhagen Offshore Wind 2005, Risoe National Laboratory, Denmark, 2005.
- [47] Madsen, H.A., Larsen, G.C., Larsen, T.J., Mikkelsen, R. and Troldborg, N. Wake deficit- and turbulence simulated with two models compared with inflow measurements on a 2MW turbine in wake conditions. In proceedings of the 2008 EWEC conference, Bruxelles, 2008.
- [48] Mann, J. The spatial structure of neutral atmospheric surface-layer turbulence. Journal of Fluid Mechanics, 273, 141-168, 1994.
- [49] Mann, J. Wind field simulation. Probabilistic Engineering Mechanics, Vol. 13, No. 4, pp. 269-282, 1998
- [50] Manuel, K.S.L. and Veers, P.S. A Comparison of Standard Coherence Models for Inflow Turbulence with Estimates from Field Measurements. Journal of Solar Energy Engineering, Vol. 126, 1069-1082, 2004.
- [51] Masson, C. Viscous differential/actuator disk method and its applications. In: Thor S-E, editor. Proceedings of the 15th IEA Symposium on the Aerodynamics of Wind Turbines, FOI, Swedish Defence Research Agency, 2002.
- [52] Medici, D. Experimental Studies of Wind Turbine Wakes, Doctoral Thesis in Fluid Mechanics, TRITA-MEK 2005:19, Stockholm, Sweden, 2005.
- [53] Michelsen, J.A. Basis3D - a Platform for Development of Multiblock PDE Solvers. Report AFM 92-05, Dept. of Fluid Mechanics, Technical University of Denmark, DTU, 1994.
- [54] Michelsen, J.A., Block Structured Multigrid Solution of 2D and 3D elliptic PDE's, Report AFM 94-06, Dept. of Fluid Mechanics, Technical University of Denmark, DTU, 1994.
- [55] Mikkelsen, R., Sørensen, J.N. and Shen, W.Z. Modelling and Analysis of the Flow Field around a Coned Rotor. Wind Energy, 4: 121-135, 2001.



- [56] Mikkelsen, R., Actuator Disc Methods Applied to Wind Turbines, MEK-FM-PHD 2003-02, Technical University of Denmark, 2003
- [57] Mikkelsen, R., Sørensen, J.N. and Troldborg, N. Prescribed Wind Shear Modelling Combined with the Actuator Line Technique. In proceedings of the 2007 EWEC conference, Milan, 2007.
- [58] Mikkelsen, R., Sørensen, J.N. and Troldborg, N. Analysis of Power Enhancement for a Row of Wind Turbines Using the Actuator Line Technique. Journal of Physics: Conference Series. The Science of Making Torque from Wind. Technical University of Denmark, Lyngby, August 2007.
- [59] Nielsen, M., Larsen, G.C. and Hansen, K.S. Simulation of inhomogeneous, non-stationary and non-Gaussian turbulent winds. Journal of Physics: Conference Series. The Science of Making Torque from Wind. Technical University of Denmark, Lyngby, August 2007.
- [60] Okulov, V.L. On the stability of multiple helical vortices. Journal of Fluid Mechanics, Vol. 521, pp. 319-342, 2004
- [61] Okulov, V.L. and Sørensen J.N. Stability of helical tip vortices in rotor far wake. Journal of Fluid Mechanics, Vol. 576, pp. 1-25, 2007.
- [62] Ta Phuoc, L., Lardat, R, Coutanceau, M. and Pineau, G. Recherche et analyse de modeles de turbulence de sous maille adaptes aux ecoulements instationnaires decolles. LIMSIS Report 93074, LIMSIS, France, 1994.
- [63] Pope, S.B. Turbulent Flows. Cambridge University Press, 2000.
- [64] Press, W.H., Teukolsky, S.A., Vetterling, W.T. and Flannery, B.P. Numerical Recipes in Fortran The Art of Scientific Computing, Second Edition. Cambridge University Press, 1992.
- [65] Rankine, W.J.M. On the Mechanical Principles of the Action of Propellers. Trans. Inst. Naval Architects, 6, 1865.
- [66] Reck, M. Computational fluid dynamics, with detached eddy simulation and the immersed boundary technique, applied to oscillating airfoils and vortex generators. PhD thesis, Technical University of Denmark, Department of Mechanical Engineering, Fluid Mechanics Section, 2004.
- [67] Saugaut, P., Large Eddy Simulation for Incompressible Flows - An Introduction, Springer, 2005
- [68] Schreck, S. The NREL full-scale wind tunnel experiment introduction to the special issue. Wind Energy, 5(2-3), 2002.
- [69] Shen, W.Z. and Sørensen, J.N. Actuator surface model for wind turbine flow computations. In proceedings of the 2007 EWEC conference, Milan, 2007.
- [70] Snel, H. Review of the Present Status of Rotor Aerodynamics. Wind Energy, 1, 46-69, 1998.

- [71] Snel, H., Schepers, J.G. and Montgomerie, B. The MEXICO project (Model Experiments in Controlled Conditions): The database and first results of data processing and interpretation. Journal of Physics: Conference Series. The Science of Making Torque from Wind. Technical University of Denmark, Lyngby, August 2007.
- [72] Sørensen J.N. and Myken A. Unsteady actuator disc model for horizontal axis wind turbines. Journal of Wind Engineering & Industrial Aerodynamics, 39, 139-49, 1992.
- [73] Sørensen J.N. and Kock, C.W. A model for unsteady rotor aerodynamics. Journal of Wind Engineering & Industrial Aerodynamics ,58:259-75,1995
- [74] Sørensen, J.N., Shen, W.Z. and Munduate, X. (1998) Analysis of Wake States by a Full-field Actuator Disc Model. Wind Energy, Vol. 1, pp. 73-78, 1998.
- [75] Sørensen, J.N. and Shen, W.Z. Numerical modelling of Wind Turbine Wakes. Journal of Fluids Engineering, Vol. 124, Issue 2, pp. 393-399, 2002.
- [76] Sørensen, J.N. and Okulov, V.L. Modeling the Far Wake behind a Wind Turbine. Proceedings of the Euromech Colloquium. Springer. 2007.
- [77] Sørensen, N.N., General Purpose Flow Solver Applied to Flow over Hills, PhD Dissertation, Risø-R-827(EN), RisøNational Laboratory, Roskilde, Denmark, 1995.
- [78] Sørensen, N.N. , Michelsen, J.A. and Schreck, S. Navier-Stokes Predictions of the NREL Phase VI Rotor in the NASA Ames  $80\text{ ft} \times 120\text{ ft}$  Wind Tunnel. Wind Energy, 5: 151-169, 2002.
- [79] Sørensen,N.N and Johansen, J. UPWIND, Aerodynamics and aero-elasticity: Rotor aerodynamics in atmospheric shear flow. In proceedings of the 2007 EWEC conference, Milan, 2007.
- [80] Taylor, G.J., Højstrup, J. Luken, E., Mclaughlin, S. and Ainslie, J.F. A review of measured wake data from the Nibe wind Turbines. European community wind energy conference, Herning, Denmark, 6-10 June, 1988.
- [81] Tindal, A.J., Garrad, A.D., Schepers, G.,Bulder, B., Hutting, H. and Verheij, F. Dynamic loads in wind farms, Proc. of European Community Wind Energy Conference, Germany, pp. 477-480, 1993.
- [82] Troldborg, N., Sørensen, J.N. and Mikkelsen, R. Actuator Line Simulation of Wake of Wind Turbine Operating in Turbulent Inflow. Journal of Physics: Conference Series. The Science of Making Torque from Wind. Technical University of Denmark, Lyngby, August 2007.
- [83] Troldborg, N., Sørensen, J.N. and Mikkelsen, R. Actuator Line Simulations of Wake of Wind Turbines in Turbulent Inflow. In proceedings of the 2007 EAWE conference, Pamplona, October 2007.
- [84] Veers, P.S. Three-Dimensional Wind Simulation,SAND88-0152-UC-261, Sandia National Laboratories, Albuquerque, New Mexico, 1988.

- [85] Verheij, F. J., Cleijne, j.W, Voutsinas, S.G., Huberson, S., Crespo, A., Delaunay,D. and Taylor, G. Wake and wind farm modelling, Proc. of European Community Wind Energy Conference, Travemunde, Germany, pp. 400-403.
- [86] Vermeer, L.J., Sørensen, J.N. and Crespo, A. Wind Turbine Wake Aerodynamics. Progress in Aerospace Sciences, Vol. 39, pp. 467-510, 2003.
- [87] Walther, J.H., Gúenot, M., Machefaux, E., Rasmussen, J.T., Chatelain, P., Okulov, V.L., Sørensen, J.N., Bergdof, M. and Koumoutsakos, P. A numerical study of the stability of helical vortices using vortex methods. Journal of Physics: Conference Series. The Science of Making Torque from Wind. Technical University of Denmark, Lyngby, August 2007.
- [88] Whale, J., Papadopoulos, K.H., Anderson, C.G., Helmis, C.G. and Skyner, D.J. A study of the near wake structure of a wind turbine comparing measurements from laboratory and full-scale experiments. Solar Energy 1996, 56(6):621-33.
- [89] Whale, J., Anderson, C.G., Bareiss, R. and Wagner, S. An experimental and numerical study of the vortex structure in the wake of a wind turbine. Journal of Wind Engineering and Industrial Aerodynamics. 2000, 84:1-21.
- [90] Wußow, S., Sitzki, L. and Hahm, T. 3D-simulation of the turbulent wake behind a wind turbine. Journal of Physics: Conference Series. The Science of Making Torque from Wind. Technical University of Denmark, Lyngby, August 2007.
- [91] Zahle, F. Wind Turbine Aerodynamics Using an Incompressible Overset Grid Method. PhD thesis, Imperial College, London, 2006.
- [92] Zahle, F. and Sørensen, N.N. On the Influence of Far-Wake Resolution of Wind Turbine Flow Simulations. Journal of Physics: Conference Series. The Science of Making Torque from Wind. Technical University of Denmark, Lyngby, August 2007.
- [93] Zahle, F. and Sørensen, N.N. Rotor Aerodynamics in Shear Flow. In proceedings of the 2008 EWEC conference, Bruxelles, 2008.
- [94] Øye, S. A simple vortex model. In: McAnulty K, editor. Proceedings of the Third IEA Symposium on the Aerodynamics of Wind Turbines, ETSU, Harwell, 1990.
- [95] Øye, S. Wind Turbine: Dynamic Flow Measurement. AFM Notat VK-233, Department of Fluid Mechanics, Technical University of Denmark, DTU, 1992